2-2013

Characterization of Self-Assembled Functional Polymeric Nanostructures: I. Magnetic Nanostructures from Metallopolymers II. Zwitterionic Polymer Vesicles in Ionic Liquid

Raghavendra Raj Maddikeri
University of Massachusetts Amherst, maddikeriraj@gmail.com

Recommended Citation

Maddikeri, Raghavendra Raj, "Characterization of Self-Assembled Functional Polymeric Nanostructures: I. Magnetic Nanostructures from Metallopolymers II. Zwitterionic Polymer Vesicles in Ionic Liquid" (2013). *Open Access Dissertations*. 694.
https://doi.org/10.7275/yhjc-hf39 https://scholarworks.umass.edu/open_access_dissertations/694

CHARACTERIZATION OF SELF-ASSEMBLED FUNCTIONAL POLYMERIC NANOSTRUCTURES:

I. MAGNETIC NANOSTRUCTURES FROM METALLOPOLYMERS
II. ZWITTERIONIC POLYMER VESICLES IN IONIC LIQUID

A Dissertation Presented

By

RAGHAVENDRA RAJ MADDIKERI

Submitted to the Graduate School of the
University of Massachusetts, Amherst in partial fulfillment
of the requirements for the degree of

DOCTOR OF PHILOSOPHY

February 2013
Polymer Science & Engineering

CHARACTERIZATION OF SELF-ASSEMBLED FUNCTIONAL POLYMERIC NANOSTRUCTURES:

I. MAGNETIC NANOSTRUCTURES FROM METALLOPOLYMERS
II. ZWITTERIONIC POLYMER VESICLES IN IONIC LIQUID

A Dissertation Presented

By

RAGHAVENDRA RAJ MADDIKERI

Approved as to style and content by

Gregory N. Tew, Chair

Samuel P. Gido, co-chair

Mark Tuominen, member

David A. Hoagland, Department Head
Polymer Science & Engineering

DEDICATION

To my parents and my loving wife, Srilatha Raghur.

ACKNOWLEDGEMENTS

I would first like to thank my advisor, Gregory Tew. He has been a wonderful support all these five years. He has kept his group multi-disciplinary with excellent group dynamics and it has been a wonderful experience working in his research group. He strives hard to keep the quality of research high in his group and among his students. These qualities learnt during these years by being with him would always be a great asset in rest of my life.

I would also like to thank my co-advisor, Samuel Gido. With great patience and personal interest he taught me the techniques of Electron Microscopy and Materials Science. He was always been there to help me in the times of distress. I am amazed at his new approaches for solving problem, a quality I would try to develop. I would sincerely like to thank, my committee member Mark Tuominen for educating me on Magnetism, an important aspect of my thesis. He has been an important collaborator and discussions with him helped me to develop my work and ideas. I would also like to thank him for allowing me to use instruments in his laboratory, which contributed substantially towards my thesis.

I also would like to thank Miguel Novak, visiting professor from Brazil for helping me with my magnetic characterizations and educating me on nanomagnetism. I would specially like to thank my team members Yongping Zha, Hitesh Thaker and Jing Jiang for synthesizing all the polymers. Without their help, I would have not made any start in my research work. I also would like to thank Zoha Al-Badri, for initially starting the work on this project and optimizing the conditions before I could embark on the project. I would like to thank Huajie and Stefan, members of Prof. Tuominen's research group for help with magnetic characterizations and discussions on magnetism.

I would like to thank all Tew group members past and present for all the help and support during my stay in UMASS. Without their help and contributions, sailing through the stage of my life was impossible. I would specially like to Melissa for going through my written documents and papers with great attention and always has been a wonderful critic, which helped me to substantially improve the quality of papers and documents. Similarly, Mike for those lengthy discussions on random topics of science and helping to solve many problems encountered my thesis. I would specially thank, Erin for all help and support and taking care of official matters. I would like to acknowledge the contributions of other group members for helping in various aspects, which I forgot to mention.

I would like to thank all my PSE friends, especially, Jyothi Prakash Mahalik (J. P.) for being a such a good friend and support all these years. I would also like to thank Eric Anderson, for all the help with TEM and other scientific discussions. I would also thank the incoming class of 2006 for being such a great group. I also would like to thank Balaji Ganapthy, my roommate for his help and support during my final stages of thesis.

To my parents, who always encouraged me to follow my passion and achieve goals. Without their sacrifices and love and I owe all my success in my life to them. I am incredibly fortunate to have such wonderful and caring parents. Further, I thank my brother Santosh, sister Padmaja and brother-in-law Rajesh, for their love and support. I really miss being with my nephew Aarush for all these 4 years. Most importantly, I would like to thank my wife Srilatha Raghur for being with me. She always motivated me with simple inspirational words, when, I had lost hope. Her life journey would always be an inspiration to me. I love you for being such a wonderful person and feel fortunate to spend rest of my life with you.

ABSTRACT

CHARACTERIZATION OF SELF-ASSEMBLED FUNCTIONAL POLYMERIC NANOSTRUCTURES:

I. MAGNETIC NANOSTRUCTURES FROM METALLOPOLYMERS
II. ZWITTERIONIC POLYMER VESICLES IN IONIC LIQUID

FEBRUARY 2013

RAGHAVENDRA RAJ MADDIKERI,

B.E., NATIONAL INSTITUTE OF TECHNOLOGY KARNATAKA, SURATHKAL, INDIA

M.S. CHALMERS UNIVERSITY OF TECHNOLOGY, GOTEBORG, SWEDEN

M.S. UNIVERSITY OF MASSACHUSETTS, AMHERST

Ph.D., UNIVERSITY OF MASSACHUSETTS, AMHERST

Directed by: Gregory N. Tew

Two diverse projects illustrate the application of various materials characterization techniques to investigate the structure and properties of nanostructured functional materials formed in both bulk as well as in solutions. In the first project, ordered magnetic nanostructures were formed within polymer matrix by novel metallopolymers. The novel metal-functionalized block copolymers (BCPs) enabled the confinement of cobalt metal ions within nanostructured BCP domains, which upon simple heat treatment resulted in room temperature ferromagnetic (RTFM) materials. On the contrary, cobalt functionalized homopolymer having similar chemical structure and higher loading of metal-ion are unstructured and exhibited superparamagnetic (SPM) behavior at room temperature. Based on a series of detailed investigations, using various materials characterization techniques, it was hypothesized that the SPM cobalt particles within BCP microdomains exhibited a collective behavior due to increased dipolar

interactions between them under the nanoconfinement of cylindrical domains in BCP, resulting in RTFM behavior. On contrary, the same SPM cobalt particles formed within homopolymer, without any confinement exhibited SPM behavior either due to lack of interactions or random interactions between them.

To further support this hypothesis, a series of BCPs were prepared in which the BCP morphology was varied between the cylindrical, lamellar, and inverted cylindrical phases and their magnetic properties were compared. All these BCPs, which are nanostructured, exhibited RTFM behavior, further supporting the proposed hypothesis. Different dimensionality or degree of nanoconfinement in BCP morphologies affected the magnetization reversal processes in these BCPs, yielding different macroscopic magnetic properties. Most strongly constrained cylindrical morphology has shown best magnetic properties (highest coercivity) among other BCP morphologies. Inverted cylindrical morphology, in which a 3-D matrix is confined between the non-magnetic cylinders, had second highest and lamellar morphology with least confinement among BCPs, exhibited lowest coercivity.

The proposed hypothesis was further tested by systematically varying the dipolar interactions between the SPM cobalt nanoparticles by reducing the density of cobalt within the cylindrical domains and varying the dimensions of the cylindrical domains (i.e. diameter). A series of novel ferrocene-cobalt containing block copolymers were developed and cobalt density within the cylindrical domains of BCP was varied by changing the chemical composition of the metal functionalized block. Further, the diameter of the cylindrical domains was varied by varying the molecular weight of the cobalt-containing BCPs. These studies allowed us to understand the fundamental

correlations between the self-assembled nanostructures and their macroscopic magnetic properties.

In the second part of the thesis, a novel amphiphilic block copolymer (ABC), composed of a hydrophilic zwitterionic block and a hydrophobic PS block, was synthesized by ROMP. The formation of zwitterionic vesicles in an ionic liquid, as well as in PBS buffer, was confirmed by TEM and DLS characterization. The dispersion of vesicles within ionic liquid enabled the usage of conventional, room temperature TEM to visualize them in their solution state. This technique of materials characterization could be extended for the visualization of other hydrophilic soft matter.

TABLE OF CONTENTS

Page

LIST OF TABLES

Table Page

LIST OF FIGURES

Figure Page

CHAPTER 1

SELF-ASSEMBLED FUNCTIONAL NANOSTRUCTURES FROM DIBLOCK COPOLYMERS

1.1. Nanostructured Materials and their Fabrication

Nanostructured materials have dimensions on the length scales of 1 – 100 nm and have exhibited unique electrical, chemical, optical, mechanical and magnetic properties that are substantially different from their bulk counterparts due to quantum size effects. Because of these unique properties, functional nanostructured materials have tremendous potential in a wide variety of applications, ranging from aerospace to biomedical applications.[1] The fabrication methods for the development of nanostructured materials can be classified as "top-down" and "bottom-up" approaches.

In top-down approach, the nanostructures are fabricated by using pattern transfer (lithographic methods), deposition (thin films) or etching (selective removal of material) techniques. Currently, lithographic-based nanofabrication techniques are often used in industry due to their ability to produce nanostructures of wide range of shapes and sizes with superior precision and accuracy.[2-4] However, they are very time consuming and have high production cost, and hence are not suitable for large scale production. On the other hand, in bottom-up approach building blocks or molecules undergo autonomous organization resulting in structures or patterns without human intervention.[5] From a technological point of view, the development of nanostructured materials by self-assembly is low-cost, fast and easily adaptable to large scale production. Molecular self-assembly is ubiquitous in biological systems in the formation of a wide variety of complex biological structures.[6] It utilizes non-covalent or weak interactions such as electrostatic, hydrogen bonding, van der Waals forces, hydrophobic interactions, $\pi - \pi$ interactions and coordination bonds between molecules for hierarchical assembly into functional supramolecular systems. Inspired by nature, the molecular self-assembly of functional block copolymers has become a very effective and promising approach to develop nanostructured materials with a wide variety of morphologies and functionalities.[6-10]

1.2. Block Copolymers: Introduction and Self-assembly

Block copolymers (BCPs) are a particular class of polymers, composed of two or more chemically distinct polymers (blocks), which are covalently bound together.[11, 12] They have gained considerable attention for various applications, owing to their ability to microphase separate into a rich variety of well-defined nanometer-sized morphologies in both bulk as well as in solutions.[9, 11, 13]

1.2.1. Self-assembly of BCPs in Bulk

The thermodynamic incompatibility between components of a BCP drives microscopic phase separation while the covalent bond connecting the blocks prevents macroscopic phase separation.[11] Thus, the minority block is segregated from the majority block forming regularly-shaped and ordered nanodomains. The morphologies of BCPs are majorly governed by three different parameters: the total degree of polymerization N ($= N_A + N_B$), volume fractions of the constituents blocks (f_A and f_B, $f_A = 1 - f_B$) and the strength of interaction parameter, χ, between two segments of BCP (Flory-Huggins parameter, which is a measure of the incompatibility between the two blocks).[14]

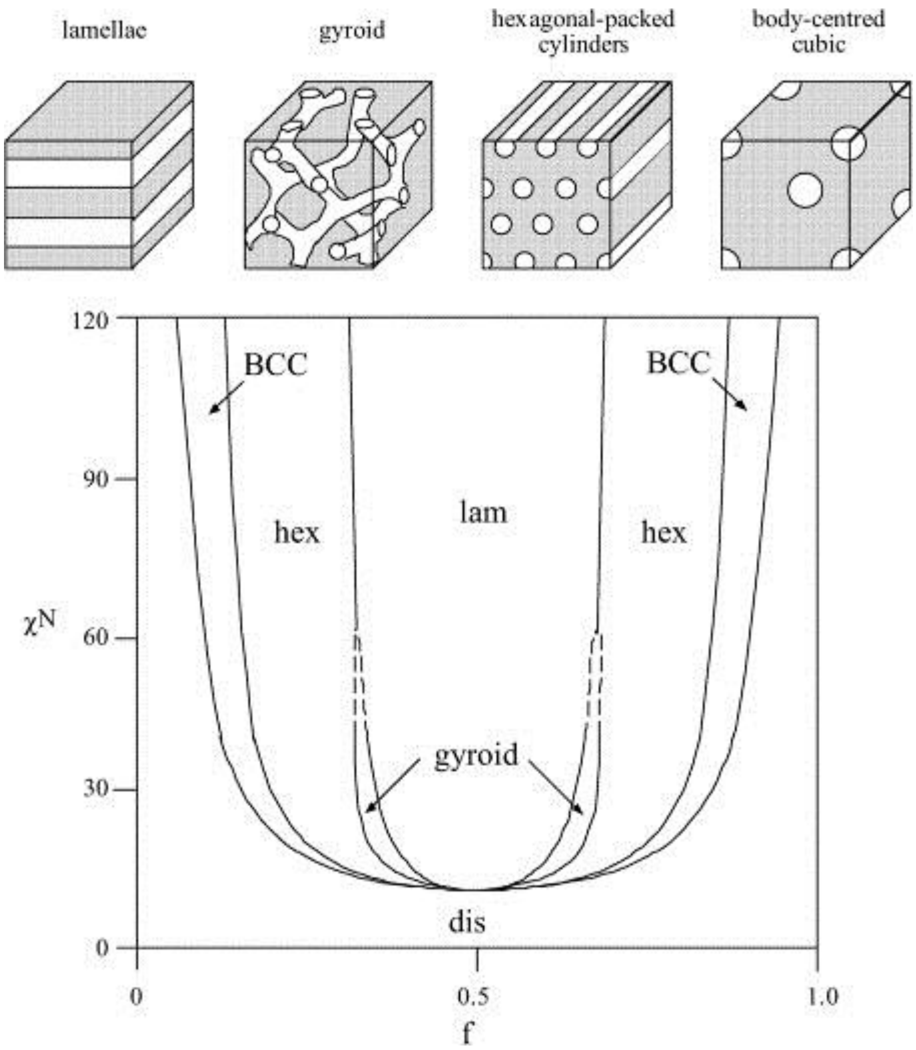

Figure 1.1 Phase diagram for a conformationally symmetric diblock copolymer, calculated using self-consistent mean field theory, illustrating the equilibrium morphologies: lamellar (lam), hexagonally-packed cylinder (hex), gyroid (gyr) and body-centered cubic (BCC) spheres.[11]

For the simplest case of a diblock copolymer (AB), the influence of χ and *f* on the microphase separated morphologies can be observed from the morphology diagram shown in Figure 1.1, where the degree of segregation, χN, is plotted against the volume fraction, *f*. At any given volume fraction, *f*, χN dictates whether the BCP is microphase separated or phase mixed. The boundary between microphase separated and phase mixed structures is referred as order-disorder transition (ODT).[11, 15, 16] The interaction parameter, χ, is inversely proportional to the temperature and hence as the temperature of the BCP is increased above ODT, the microdomain structure disappears completely, giving rise to a disordered homogenous phase. This critical temperature is referred to as T_{ODT}. On the other hand, by varying the volume fraction, *f*, the morphology of the BCP can be varied into the structures shown in Figure 1.1, including spherical (Sph) or, hexagonal packed cylinder (Cyl), and lamellar (Lam). Apart from these classical structures, gyroid (Gyr) and hexagonally perforate lamellar (HPL) are also observed depending on the value of χN. The boundary between two different morphologies is called order-order transition (OOT).[11, 15, 16]

Consequently, the phase behavior of the diblock copolymer (BCP) and extent of segregation is controlled by segregation product χN. Depending on its value; three different regimes can be distinguished: (1) the weak segregation limit (WSL) for $\chi N \leq 10$, (2) the intermediate segregation region (ISR) for $10 < \chi N < 50$ and (3) the strong segregation limit (SSL) for $\chi N \rightarrow \infty$. Theories were developed in different segregation regimes to explain the equilibrium phase behavior of linear diblock copolymers. Helfand and co-workers developed self-consistent field theory (SCFT) in strong segregation limit assuming that the microphase domains are well developed and the interphase region is very narrow due to chain stretching. The experimental results for strongly segregated systems were consistent with this theory. However, due to the assumptions, this theory was not able to predict the ODT boundary accurately. Leibler *et al.* developed theories in weak-segregation regime assuming that composition fluctuations are small and the effective free energy can be written in the Landau Ginzburg form.[17] With the advent of computer technology, Matsen and Bates used SCFT without any approximations to develop general theory explaining the equilibrium phase behavior in all the segregation regimes of BCP.[18-20] According to this theory, in SSL regime, the BCP morphologies transit in the order Sph – Hex – Lam – inverted phase of Hex – inverted Sph as the volume fraction is increased (See Figure 1.1). In weak and intermediate regimes, the Gyr phase is observed in between Hex and Lam phases, which vanishes as the χN increases to SSL regime. The dimensions of the domains can be tuned from ~ 5 to ~100 nm by changing the molar mass of the block.[21]

In addition to χN and f, other additional parameters such as architecture, fluctuation effects, conformational asymmetry, polydispersity index and additives effect the phase behavior of BCP in bulk.[19] Nonlinear architectures of the BCP, such as graft and star, were shown to have a strong effect on their phase behavior by changing both T_{ODT}, and $\mathrm{T}_{\mathrm{OOT}}$. Fluctuation effects decrease the T_{ODT} and allow for direct transitions between phases, which are not adjacent in the original phase diagram from Leibler. Conformational asymmetry, which is the ratio of block A and B statistical segment lengths, α_A/α_B, shifts the order-order transitions towards compositions richer in the segments with the longer statistical length.[12, 22]

1.2.2. Self-assembly of BCPs in Solution

Block copolymers self-assemble in selective solvents, which preferentially dissolve one block but not the other block, forming various nanostructures such as micelles and vesicles. In the solution, the interactions between the solvent and the different blocks dictate the ability to form well-defined structures. Amphiphilic block copolymers (ABC) in aqueous solvents are most widely studied example systems for the self-assembly of block copolymers in dilute solutions. The amphiphilic block copolymers consist of hydrophobic and hydrophilic blocks. In aqueous solutions, interactions between the hydrophobic block and solvent are unfavorable and ABCs undergo self-assembly in order to minimize these unfavorable interactions.

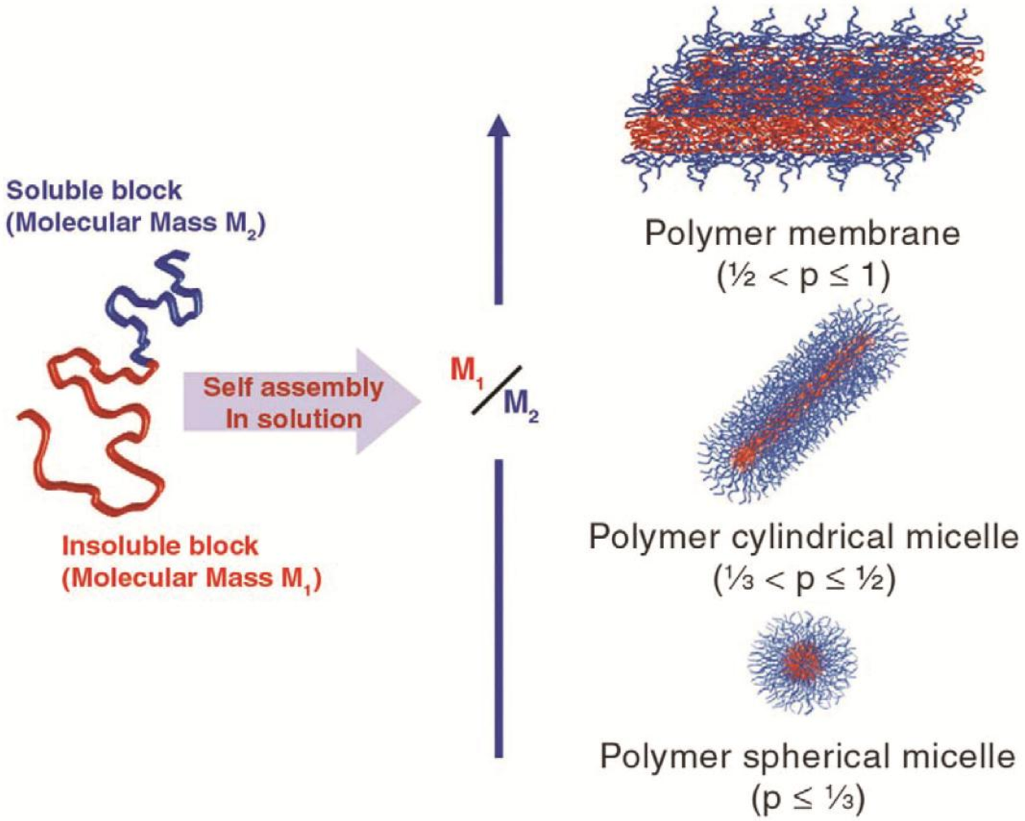

Figure 1.2 Various self-assembled structure formed by block copolymers in block selective solvents. The morphology of the nanostructure formed in the solution is determined by the packing parameter, p.[23, 24]

The various morphologies obtained due to the self-assembly of a BCP in solution is determined by the "packing parameter", p, which is defined as

$$p = \frac{\nu}{a_0 l_c} \tag{1}$$

Where ν is the volume of hydrophobic chains, a_0 is the optimal area of the head group, and l_c is the length of the hydrophobic tail. As a general rule, spherical micelles are favored when $p \leq 1/3$, cylindrical micelles when $1/3 \leq p \leq 1/2$ and vesicles or polymersomes $1/2 \leq p \leq 1$.[3, 23] Thus, by tuning the block length the molecular weight targeted morphology can be achieved. Several factors such as copolymer composition[25, 26], nature of the solvent[27], salt concentration[28], additives such as ions[28], homopolymers[29], or surfactants[30], polydispersity[31, 32], and temperature[33] can affect the morphologies of self-assembled ABC in solution. In addition, by functionalizing different blocks of ABC, novel functionalities can be added to BCP nanostructures. For example, pH sensitive vesicles can be obtained by using polyacid blocks, which change their ionization status by change in pH.[29] The peptide functionalized polymer vesicles and micelles have attracted significant attention for drug and gene delivery applications.[31, 34]

1.2.3. Block Copolymers for Nanofabrication

The nanofabrication methods should have an ability to develop, control, manipulate and modify the nanostructures. The BCPs have emerged as an important tool for the fabrication of nanostructured materials due to their following advantages[35]:

1) **Precise control over length scale**

The dimensions of the BCPs can varied from 5 – 50 nm by varying the molecular weight, monomer structure and temperature.

2) **Control over morphology**

A simple diblock copolymer can microphase separate in different morphologies namingly : hexagonal cylinders(Cyl), Lamellar (Lam), Inverted cylindrical (Inv.

Cyl), Gyroid (Gyr) and Spherical (BCC) morphology. In bulk phase, the morphology can be controlled by varying the composition, temperature, architecture and solvent. A block copolymer can only have two blocks (diblock copolymer, AB) or more blocks (multi-block copolymers) such as triblock copolymers, ABC. The block copolymers can be linear or more complex architectures such as star, comb, or ladder shaped block copolymers. A wide variety of morphologies are possible by the composition (number of blocks) and architecture of the block copolymers.

3) Control over domain functionality and properties

With the advances in polymerization techniques, now it is possible to precisely control the composition and confer functionality of different blocks of BCPs. Further, the macromolecules with complex architectures have been realized. Having control over the functionality of domains would allow scientists to develop materials with desired macroscopic properties.

1.3. Dissertation Outline

Understanding the correlation between the structure and functionality of nanostructures and the macroscopic properties of nanostructured materials is necessary in the development of advanced functional materials with desirable properties. Materials characterization is an important tool in deriving necessary details to develop these structure-property relationships in mateirals.[35] In two different projects described in this dissertation, novel nanostructured polymeric materials are developed by the self-assembly of functional BCPs. Relevant materials characterization techniques are utilized to investigate the morphology and functionality of these nanostructures and correlate it with their macroscopic properties. Thus this dissertation is principally divided into two different sections. In the first part, novel nanostructured magnetic polymers with RTFM behavior were developed by the self-assembly of metal-ion containing BCPs. In second part, functional polymeric nanostructures were formed in solution by a novel zwitterionic amphiphilic block copolymers. In Chapter 2, design, optimization, development and characterization of novel cobalt-functionalized homo and block copolymers has been described. Various materials characterization techniques were utilized to demonstrate the importance of nanostructuring on the magnetic behavior of these metal-containing polymers. The hypothesis was further tested by developing a series of cobalt-functionalized BCPs with different morphologies - cylindrical, lamellae, and the inverted cylindrical morphology in Chapter 3. Among all the morphologies of BCP, best magnetic properties were obtained for polymers with cylindrical morphology. An extensive magnetic characterization of these BCPs with different morphologies will be discussed to explain this observation. In Chapter 4, the magnetic properties of metal functionalized BCPs exhibiting cylindrical morphology was tuned by changing chemical composition and molecular weight has been illustrated. These studies give further insight into the mechanism operative in delivering magnetic properties to these novel nanostructured magnetic materials.

Deviating from the bulk materials, the formation of polymer vesicles by the self-assembly of a novel amphiphilic zwitterionic BCPs in ionic liquid, a unique solvent, will be discussed in the Chapter 5. An improved method for the characterization of nanostructures in solution is demonstrated in this work.

CHAPTER 2

MAGNETIC PROPERTIES OF COBALT-CONTAINING POLYMERS

2.1. Introduction to Magnetic Nanostructures

Magnetic materials are used as components in many electromechanical and electronic devices used in everyday life and hence are considered as indispensable in modern technology.[36] Nanostructured magnetic materials exhibit enhanced and interesting properties than their bulk counterparts and thus have opened new avenues for technological applications such as magnetic data storage, magnetic sensors, magneto optics, magnetic separation, spintronics, magnetic refrigeration and cancer treatment.[37, 38, 39] Hence, magnetic nanostructures are an interesting class of materials from both scientific as well as technological point of views. Rather than individual magnetic nanostructures, ordered arrays are more applicable in industrial applications due to their enhanced magnetic properties.[2] The fabrication of ordered array of magnetic nanostructures can be majorly classified into two categories: "top-down" and "bottom-up".[2, 39] In top-down approach, the nanostructures are fabricated by using light, X-ray, electron beam (E-beam) or nanoimprint lithographic based techniques. Currently, these lithographic based nanofabrication techniques are being used in industry due to their ability to produce nanostructures of wide range of shapes and sizes with superior precision and accuracy. However, they are very time consuming and have high production cost, and hence are not suitable for large scale production.[40] On the other hand, in bottom-up approach, nanostructures are formed by the spontaneous self-assembly of macromolecules. Bottom-up approaches are simple and low cost processes and thus can be used for large scale production of ordered array of magnetic nanostructures.[2, 41, 42] The individual magnetic nanostructures act as building blocks in development of new magnetic materials and devices by bottom up approach. Therefore, a complete understanding of their properties is necessary in order to engineer their properties.

2.2. Magnetic Materials: Diamagnetism, Paramagnetism and Ferromagnetism

The behavior of a magnetic material in response to an applied magnetic field is considered as a primary factor in their practical applicability. Thus for the evaluation of the material, the induced magnetization, M or B is plotted as a function of the applied field. The M-H or magnetization curves for any given magnetic material are important not only from application point of view but also in understanding the magnetization process. The magnetic behaviors of different kind of magnetic materials - diamagnetic, paramagnetic and ferromagnetic materials are described below.

The origin of magnetism in materials is attributed to motion of electrons in an atom. In diamagnetic materials, the atoms have filled electron shells and hence the net magnetic moment is zero. When subjected to an external applied field, the induced magnetization of the diamagnetic material opposes applied field and exhibits weak, negative susceptibility (slope of the graph) as shown Figure 2.1a. The atoms with unfilled electron shells have a non-zero net magnetic moment. Depending on the arrangement of these magnetic moments the material can exhibit paramagnetic or ferromagnetic behavior. In paramagnetic material, each atom has individual magnetic moment but due to their random arrangement, their net magnetic moment within the material is zero. When an external magnetic field is applied, the randomly oriented magnetic moments rotate and orient themselves along the direction of the applied field with induced magnetization. A typical magnetization behavior of a paramagnet as function of applied field is shown in Figure 2.1b. As the applied field is increased, more magnetic moments are aligned in the direction of the magnetic field and hence, the induced magnetization is a linear function of the applied field. Upon the removal of magnetic field, the magnetic moments return to their random orientation and hence their net magnetic moment is zero.

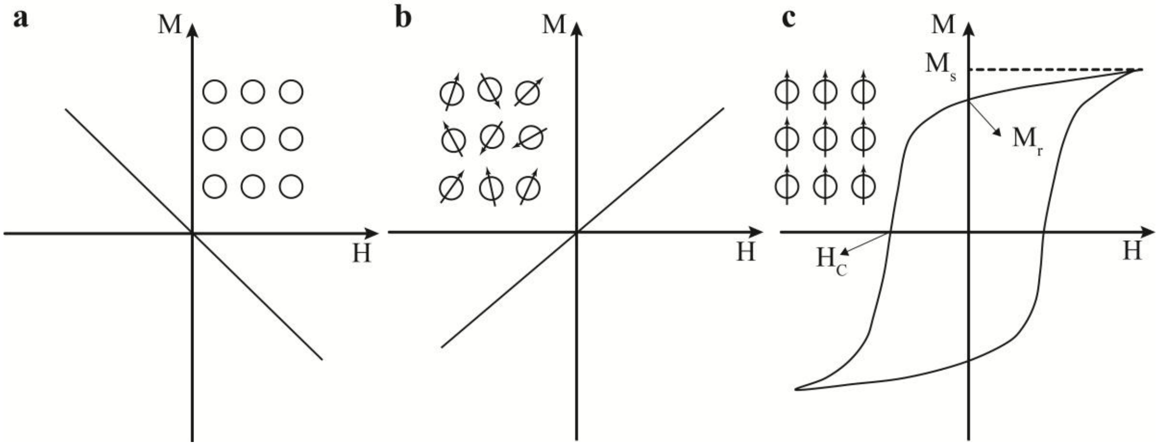

Figure 2.1 Magnetization as function of field curves for a) diamagnetic b) paramagnetic and c) ferromagnetic. Ferromagnetic material exhibits hysteresis and M_s, M_r, and H_c representing saturation magnetization, remenance, and coercivity respectively. The diamagnetic and paramagnetic material does not exhibit any hysteresis and hence zero coercivity. Superparamagnetic material above its blocking temperature would exhibit similar behavior to paramagnetic.[43]

In ferromagnetic materials, the individual magnetic moments are arranged in an orderly fashion so that the net magnetic moment is not zero. A typical magnetization curve for a ferromagnetic sample is shown in Figure 2.1c. The induced magnetization of the ferromagnetic material increases non-linearly with an increase in the applied field. At very high fields, all the magnetic moments within material are oriented in the direction of the magnetic field and any further increase in the field strength will not result in increased magnetization. The ferromagnetic material in this condition is considered to be in saturated state and the corresponding induced magnetization is called saturation magnetization, M_s. Upon the removal of magnetic field, the induced magnetization decreases non-linearly (demagnetizing), taking a different path than during magnetization process. When the applied field is reduced to zero, the induced magnetization is not zero but retains certain amount of magnetization called as remnant magnetization M_r. A magnetic field equal to the coercive field H_c is required to switch the magnetization into opposite direction and to bring the remnant magnetization to zero. The parameters M_r and H_c are used to describe the strength of the ferromagnet. In contrast, an ideal paramagnet material would have zero M_r and H_c.

2.3. Coercivity: Mechanisms of Magnetization Reversal

As described above, the coercivity is a quantitative parameter to describe the strength of a permanent magnet. When a negative coercive field is applied to a ferromagnetic material, the magnetization is reduced to zero by “magnetization reversal” process. Hence, the knowledge of magnetization reversal process is essential in order to understand the magnetic behavior of novel ferromagnetic materials. Several models have been proposed in the literature to describe the magnetization reversal process in these materials. Among them, magnetization reversal by coherent rotation is a widely accepted model for smaller particles with single-domain. Magnetization reversal by nucleation and propagation of domain wall has been a widely accepted model for multi-domain materials. In large single-domain particles such as nanorods and nanowires, magnetization reversal by non-uniform rotational process such as curling and fanning are applicable. These magnetization reversal mechanisms are explained in detail below.

2.3.1. Magnetization Reversal by Coherent Rotation

The simplest case to describe the magnetization reversal in a ferromagnetic material is described by Stoner-Wolfarth model for single-domain particle. A non-interacting spheroidal particle with uniaxial magnetic anisotropy as shown in the Figure 2.2 is considered to explain the model.

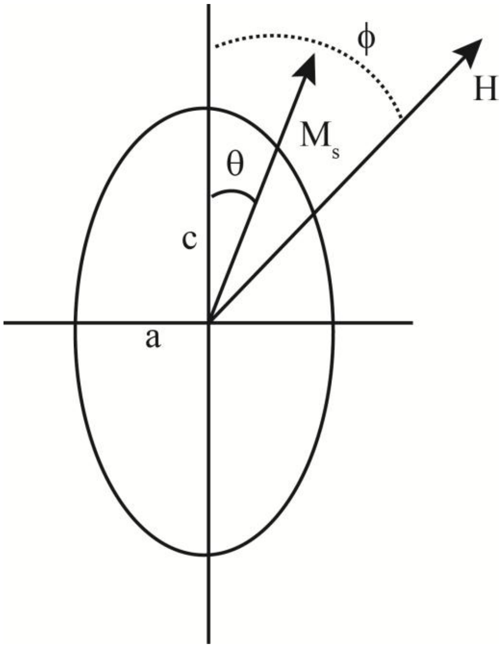

Figure 2.2 Magnetization reversal process in a single-domain particle in which the shape and crystallographic axis coincide. An externally applied field at an angle ϕ relative to the easy axis and the net magnetization lie at an angle θ.[43]

The magnetic anisotropy of the particle is either due to magnetocrystalline effects or shape anisotropy. For simplification, the anisotropy axis is assumed to coincide with the easy axis of magnetization (or symmetry axis) of the spheroid, which is actually dependent on the nature of the material and the shape of the particle. The magnetization reversal of this single-domain particle is described by the rotation of all the atomic moments of the particle in unison (coherent rotation) from the easy axis direction to direction of applied field. The total magnetic anisotropy energy of this single domain spheroidal nanoparticle is given by a simple expression.

$$E_a = KVsin^2\theta \tag{1}$$

where θ is the angle between the net magnetization of the particle and the anisotropy axis and K is the anisotropy constant.

In the absence of an applied field, the net magnetization, $M_{s,}$ is aligned in the direction parallel to the easy axis. An external field H is applied in a direction which is at an angle ϕ from the easy axis of the particle. The net magnetization of the particle, M_s rotates away from the easy axis and towards the direction of an applied field, by an angle θ, depending on the relative strength of the field and anisotropy of the material. Since, all the spins or atomic moments within the single domain particle rotate in unison, its overall moment or spin is referred as “superspin”. Considering the easy axis of magnetization for the particle, in the absence of the field, one can imagine two preferred orientations for superspin, “up” and “down” (or $\theta = 0$ or $\theta = \pi$). According to the equation 1, the free energy of the system will then have two minima, separated by an energy barrier $E_B = KV$, where V corresponds to volume of the particle (See Figure 2.3). This energy barrier is reduced as the strength of the applied field is increased and eventually becomes zero at certain critical field strength. In magnetization reversal by coherent rotation model, this critical field corresponds to the coercive field and is given by

$$H_c = \frac{2K}{M_s} \tag{2}$$

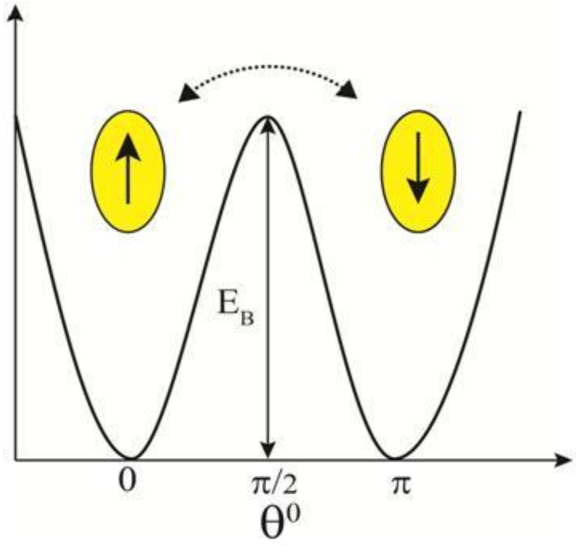

Figure 2.3 Schematic representation of potential energy of single-domain particle with uniaxial (e.g. Shape anisotropy) as a function of magnetization direction. The E_B represents the energy barrier, required to overcome, for the magnetization reversal by coherent rotation. The θ is the angle between the net magnetization (M_s) and the easy-axis.[44]

The rate of magnetization reversal is determined by the thermal energy of the system. If the energy barrier, $KV \gg k_BT$, then the superspin cannot switch spontaneously and the system behaves like a ferromagnet at a given temperature, T. However, if the energy barrier is of the order of thermal energy or lesser, i.e. $KV \sim k_BT$, the spontaneous switching of the superspin can occur, depending on the time scale of the experiment. Such nanoparticles are called 'superparamagnetic (SPM) nanoparticles'. Further, the energy barrier is a function of volume of the particle ($E_B = KV$) and therefore is reduced as the size of the single-domain particle is reduced at given anisotropy energy constant. As seen in the Figure 2.4, for sizes lesser than critical diameter (D_c) a transition from ferromagnetic to superparamagnetic state occurs. Further, the magnetization reversal process is a time dependent process. When sufficient thermal energy to overcome the energy barrier is available, the fluctuations of the superspin in two possible easy axis directions take place with a frequency f or a characteristic relaxation time $\tau = {}^{1}/_{2\pi f}$. A quantitative expression for the τ is given by Neel-Brown model following an Arrhenius type of activation law.

$$\tau = \tau_0 exp\left(\frac{KV}{k_B T}\right) \tag{3}$$

where the prefactor $\tau_0 \sim 10^{-9}$s for superparamagnetic particles within experimental measurement time scales.

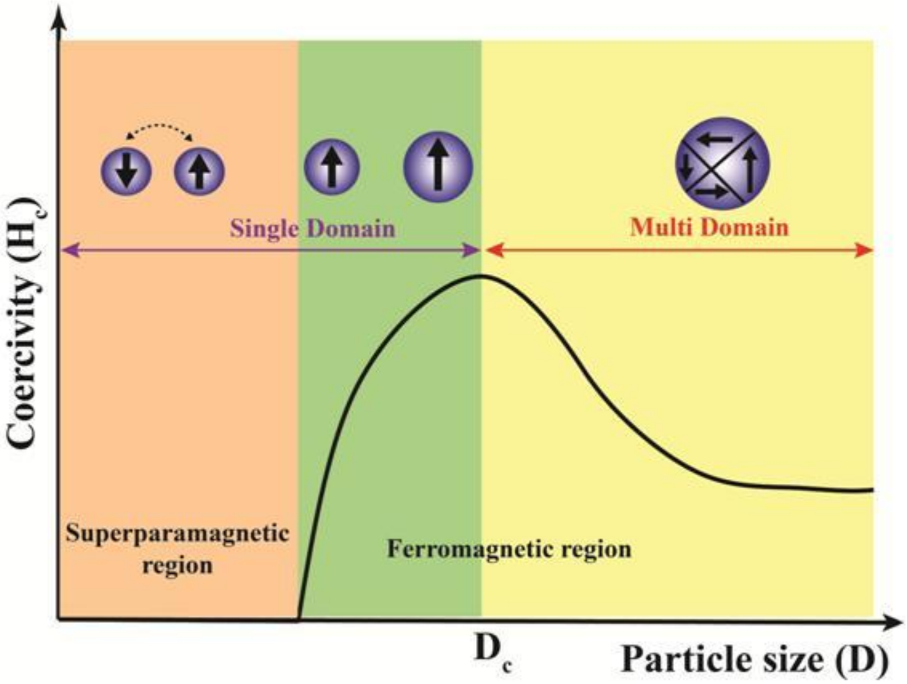

Figure 2.4 Effect of size of the nanoparticle on its domain structure and coercivity. As the size is reduced below critical radius or diameter (D_c), a multi-domain structure is energetically unfavorable and transits into single-domain structure. Similarly, further reduction in the size of particle, a transition from ferromagnetic to superparamagnetic behavior occurs.[45]

According to the equation 3, the dynamics of the magnetization reversal is strongly dependent on temperature. At higher temperatures, the magnetic moments will have sufficient energy to overcome the energy barrier and hence will fluctuate rapidly (relaxation time is low). As the temperature is lowered the fluctuations are reduced and at very low temperatures, the fluctuations of the moment are completely blocked or frozen, as the energy barrier is too high to overcome with the available thermal energy. For a given probing timescale of a measurement, there is a characteristic crossover temperature, above which the magnetic moments are ‘unblocked’ and below which they are ‘blocked’. This characteristic temperature is called the “blocking temperature”, T_B, corresponding to the temperature at which the timescale of the thermal fluctuations of the nanoparticles match to that of the measurement timescale and hence is given by:

$$\tau_{exp} = \tau(T_B) = \tau_0 \exp\left(\frac{KV}{k_B T}\right) \Rightarrow T_B = \frac{KV}{k_B ln\left({}^{\tau_{exp}}/{}_{\tau_0}\right)} \tag{4}$$

Thus, the blocking temperature is not an intrinsic temperature of the system but depends strongly on the measurement time. To summarize, the magnetization reversal process of a single-domain particle is explained by coherent rotation model and its dynamics is dependent on temperature, time and applied field.

2.3.2. Non-uniform Magnetization Reversal: Curling

The simplest non-uniform or non-coherent reversal mode is curling. The transition from the coherent rotation to non-uniform reversal mode is determined by exchange length given by:

$$\lambda = \sqrt{{}^{A}/{}_{M_s}}\,, \tag{5}$$

where, A is the exchange energy. For particles having the radius larger than the exchange length, magnetization reversal by curling is more favorable and the process is believed to be initiated by nucleus which then propagates throughout the sample. For example, the magnetization reversal in nanowires has been explained by curling and propagation mode.[46]

2.3.3. Magnetization reversal by Domain Wall Motion

The ferromagnetic particles of large size are divided into uniformly magnetized regions called as “magnetic domains” and separated by “domain walls (or Bloch walls)” in order to minimize its magnetostatic energy. Within each magnetic domain, all the atomic magnetic moments are aligned parallel, so that the magnetization is almost saturated. Certain crystallographic axes called as ‘magnetic easy axes’ are preferred by these magnetic moments but the direction of alignment varies from domain to domain in a random manner. The domain wall is an interface between two magnetic domains and due to energy considerations, the direction of magnetic moments within them changes gradually from one domain to another. Since the atomic moments within the domain wall are aligned in non-easy directions, the anisotropic energy cost is higher than that of the adjacent domains. Therefore, while the magnetostatic energy of bulk ferromagnetic material is reduced by the formation of magnetic domains, an additional energy is required for the formation of domain walls. The magnetostatic energy is proportional to the volume of material whereas the domain wall energy is proportional to the surface area. As the size of material is reduced below critical size, the increase in energy due to domain wall formation dominates over the decrease in magnetostatic energy attributed to the formation of domains, favoring a uniformly magnetized single domain (See Figure 2.4).

The magnetization in multi-domain or bulk ferromagnetic material is explained by combination of domain wall motion and coherent rotation. The magnetic hysteresis curve would be an indispensable tool to explain different processes of magnetization reversal in a multi-domain ferromagnetic material. At the application of an external field, the domains which are aligned favorably with respect to the applied field in the demagnetized multi-domain ferromagnetic material grow at the expense of domains which are unfavorably aligned. At higher fields, the domain rotation can occur in which the magnetization can suddenly rotate away from the original direction of the magnetization to the crystallographic easy axis which is nearest to the field direction. The final domain process at highest magnetic fields is by the coherent rotation of the domains to become aligned parallel to the direction of magnetic field. Irrespective of the easy and hard axes, the whole material is aligned in the direction of magnetic field, resulting in a saturated state. Thus the magnetization of a ferromagnet occurs by a series of discontinuous steps due to domain wall motion, and very small steps are sometimes seen on the magnetization curves. This is known as the “Barkhausen effect”.

Now when the ferromagnetic multi-domain material in its saturated state is subjected to a reverse field, magnetization reversal occurs by nucleation and growth of Bloch walls. The process of magnetization reversal starts with the formation of a “nucleus” in the small regions where either the magnetic moments are not fully aligned in the direction of field or local defects are present. The local values of the exchange field and anisotropy field near defect regions are reduced with respect to that in bulk and hence local magnetization reversal is easier in these regions. Within the nucleus, the magnetic moments have non-uniform configuration similar to that of domain wall. This domain wall subsequently grows into main phase to form a magnetic domain and then propagates into whole material till the magnetization reversal is established. If there is no hindrance to the domain wall displacement, the magnetization of the ferromagnetic material occurs at low field. The surfaces, impurities and strains in the material can pin the domain wall movement and therefore increase the coercivity. Thus local defects play an important role in determining the magnetization reversal process in ferromagnetic materials. If too many defects are present within the material, then the nucleation of domain wall happens easily but its motion is hindered. On the contrary, if the defects are less in the material then the nucleation of domain wall is difficult but once they are formed the propagation is much faster.

2.4. Collective Behavior of Superparamagnetic Nanoparticles

As described above, magnetic nanostructures such as nanoparticles are building blocks in the development of novel magnetic materials or devices. Thus the magnetization reversal in individual nanoparticles was described, in both single-domain and multi-domain regime. Hence, the next logical step is to understand the magnetic behavior of an ensemble of nanoparticles. In real systems, often an ensemble of nanoparticles is encountered than individual nanoparticle and thus it is critical to understand their magnetic behavior. We know from previous sections that particles with sizes lesser than critical radius have single-domain and due to its large moment can be considered as “superspin”. In an ensemble of SPM particles, if the superspins are widely spaced or isolated from one another, their interactions (dipolar) are negligible leading to

SPM behavior. At temperatures below the blocking temperature (T_B), the thermal energy is not sufficient for overcoming the anisotropy energy barrier and hence the superspins are in blocked state, exhibiting ferromagnetic-like behavior. On the contrary, when the inter-particle interactions are not negligible, the system shows a collective behavior, which overcomes the individual anisotropy of the particles.[47] However, if the interactions between the particles are too weak, the ensemble still exhibits a superparamagnetic behavior. [48]

Several different types of magnetic inter-particle interactions are possible between magnetic nanoparticles and their strength is dependent on their concentration. Magnetic dipolar interactions are always present between particles and are an inverse function of distance between them ($1/d^3$). If the distance between the nanoparticles is very close, direct exchange between the surface atoms on the nanoparticles is possible and is called as exchange interaction. If the matrix is metallic, then RKKY (Ruderman-Kittel-Kasuya-Yosida) interactions can occur between particles. When the matrix is insulating, superexchange interactions can exist depending on the structure and nature of the matrix and the bonding at the particle matrix interface. From, insulating magnetic materials, exchange interactions are short ranged, but if the bonding is favorable, superexchange can extend until large distance. The strength of these interactions is dependent on their separation distance, degree of mutual alignment and the nature of matrix surrounding them.[44, 49]

These magnetic interactions can significantly affect the energy barrier ($E_B = K_{eff}V_{eff}$), increasing both K_{eff} and effective volume, V_{eff} which depends on the symmetry of the anisotropy of the single particle. An increase in the energy barrier will subsequently increase the blocking temperature of the system and thus affect their magnetic behavior.[48, 50, 51] For example, closely packed arrays of magnetite nanoparticles exhibit ferromagnetic behavior even for particles with diameter smaller than 26 nm due to strong dipole-dipole interactions. Similarly, the Co nanoparticles embedded in an antiferromagnetic matrix (CoO) has shown 30-fold increase in their blocking temperature in comparison to be embedded in Al_2O_3.[52] This was due to a strong exchange interaction in the system, causing the pinning of magnetic moments of nanoparticles in the matrix. Thus, in a dense ensemble of single-domain nanoparticles, interparticle interactions can dominate over single-particle magnetic behavior and lead to collective behavior. Depending on the strength of interparticle interactions, two different collective states are distinguished, namely superspin glass (SSG) and the superferromagnetic (SFM) [44, 49, 51, 53, 54].

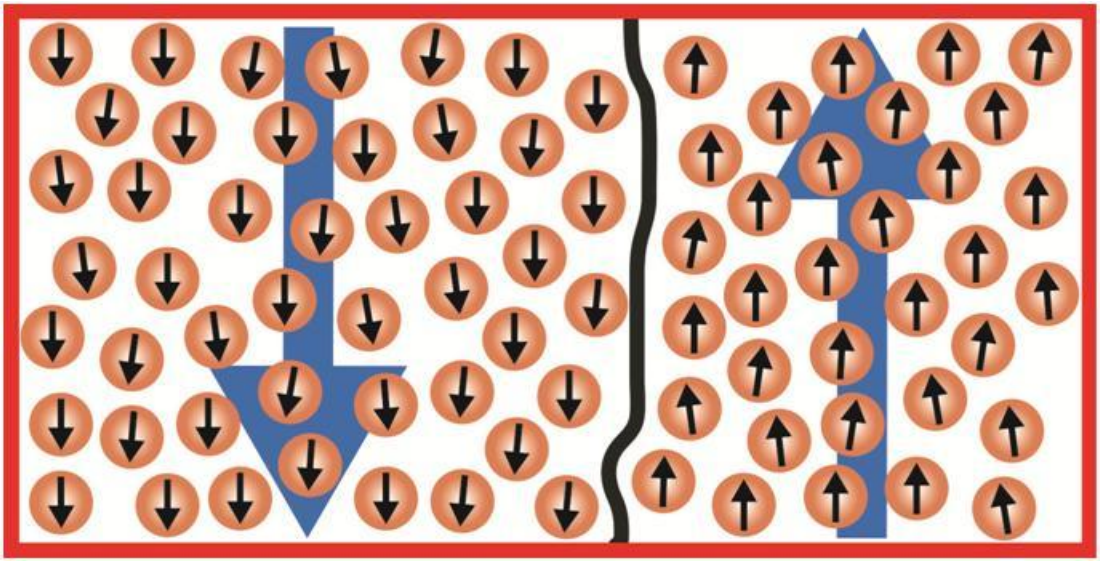

Figure 2.5 Schematic representation of SFM state in ensemble of single-domain nanoparticles represented by circles. The black arrows inside the circles represent the superspins of the nanoparticles. The bold black line represents a fictitious SFM domain wall. The two wide arrows represent the average magnetization direction and magnitude inside each SFM domain. [44]

SSG state is observed in systems where the strength of the interparticle interactions is of intermediate strength, randomness in the particle positions and sufficiently narrow size distribution.[55] The superspins are frozen collectively into a spin glass phase below a critical temperature, T_g. The SSG behavior has been observed in various nanoparticle systems.[55-58] For example, a frozen ferrofluid consisting of γ-Fe_2O_3 nanoparticles of diameter of 8.6 nm exhibited SSG behavior.[56, 59] The nanoparticles within the ferrofluid have rotational freedom and hence their interaction is random and often, a SSG behavior is observed in them. For high strength of dipolar interactions or higher densities of particles and hence stronger interactions, SFM state is observed. The nanoparticles ensemble system in SFM state behaves similar to ferromagnetic material and correlations arise between superspins of nanoparticles (instead of atomic moments). The SFM state has domains, similar to magnetic domain ferromagnetic materials, with only difference being that the atomic moments are now replaced by superspins of the individual nanoparticles, as shown in the Figure 2.5. Thus magnetic reversal of the nanoparticle ensemble system exhibiting collective behavior can be essentially explained by the nucleation and propagation of domain walls, similar to regular ferromagnetic material.[44, 53, 60]

Experimentally, the different collective states have been illustrated by controlling the interparticle interaction strength. For example, depending on the inter-particle interactions, in the granular (discontinuous) metal-insulator multilayer system (DMIM), different magnetic states are encountered. The $Co_{80}Fe_{20}$ granules are grown at sapphire interface and the nominal thickness between the layers was varied, controlling the strength of interaction. Depending on the interaction strength SPM, SSG and SFM state were demonstrated [61-64]. Similarly, Sankar *et al*. have studied non-percolated Co-SiO_2 granular films and has described the ferromagnetic-like correlations between the nanoparticles by small-angle neutron scattering (SANS) studies in the absence of magnetic field. However, at dilute concentrations, these ferromagnetic interactions were absent.[52]

2.5. Fabrication of Magnetic Nanostructures by Block Copolymers

Among bottom-up approaches for the fabrication of ordered magnetic nanostructures, block copolymers have attracted great attention.[65] The microphase separation of block copolymers offers a straight forward and simple approach for the generation of nanostructures by either acting as template, structure-directing agent or functional unit.[66] Recent advances in the living polymerization methods such as ring open metathesis polymerization (ROMP) have allowed synthetic chemists to tailor the dimensions, morphology and functionality of the block copolymer domains.[15] This method can be applied to develop magnetic nanostructures by confining the ferromagnetic metal ions to one particular domain of block copolymer.[67-69] Applying similar approach, in our published work the development of nanostructured magnetic materials by the self-assembly of functional diblock copolymers by confining ferromagnetic metal-ion (i.e. Cobalt) to one particular block has been demonstrated.[70] Since, the magnetic behavior of similar BCPs will be discussed in this thesis; a short review on the formation of magnetic nanostructures by using polymers is presented below. The approaches to develop nanostructured magnetic polymer materials can be classified into three different approaches as shown in the Fig. 2.6 .

In the first approach, the magnetic nanoparticles are synthesized *ex-situ* (either coated with specific polymer or uncoated) and mixed with block copolymer solution, which selectively decorate one particular domain of block copolymer (See Figure 2.6a).[71-73] Nanoparticles have many unique and size dependent catalytic, magnetic, optical and electronic properties. Since nanoparticles are synthesized *ex situ* in this approach, their size, composition and morphology can be controlled. At the same time, the BCPs are nanostructured and the domains act as scaffolds or templates.[74-76] Due to the synergetic interaction of individual components, the resulting nanocomposites have an ordered array of nanoparticles with unique spatial distribution within the matrix of polymers and hence showed many interesting properties.[66, 77, 78]

Several nanocomposites have been developed by this approach which incorporate quantum dots[79, 80], noble metals[81] and semiconductor nanoparticles[82, 83]. However, a fewer examples have been reported in literature on the development of magnetic materials/nanocomposites by this approach due to several disadvantages.[84-88] First of all, the incorporation of magnetic nanoparticles altered the characteristic dimension and morphology of the BCP. Further, the strong dipolar interactions between the magnetic particles resulted in their aggregation, either in the solution or within the polymer matrix, which yielded reduced properties. Additionally, these aggregates in turn can also affect the morphology of the BCP.[89-91] These problems can be overcome by having an understanding on various factors that determine the morphology and hence the macroscopic properties of magnetic nanocomposites developed by this approach

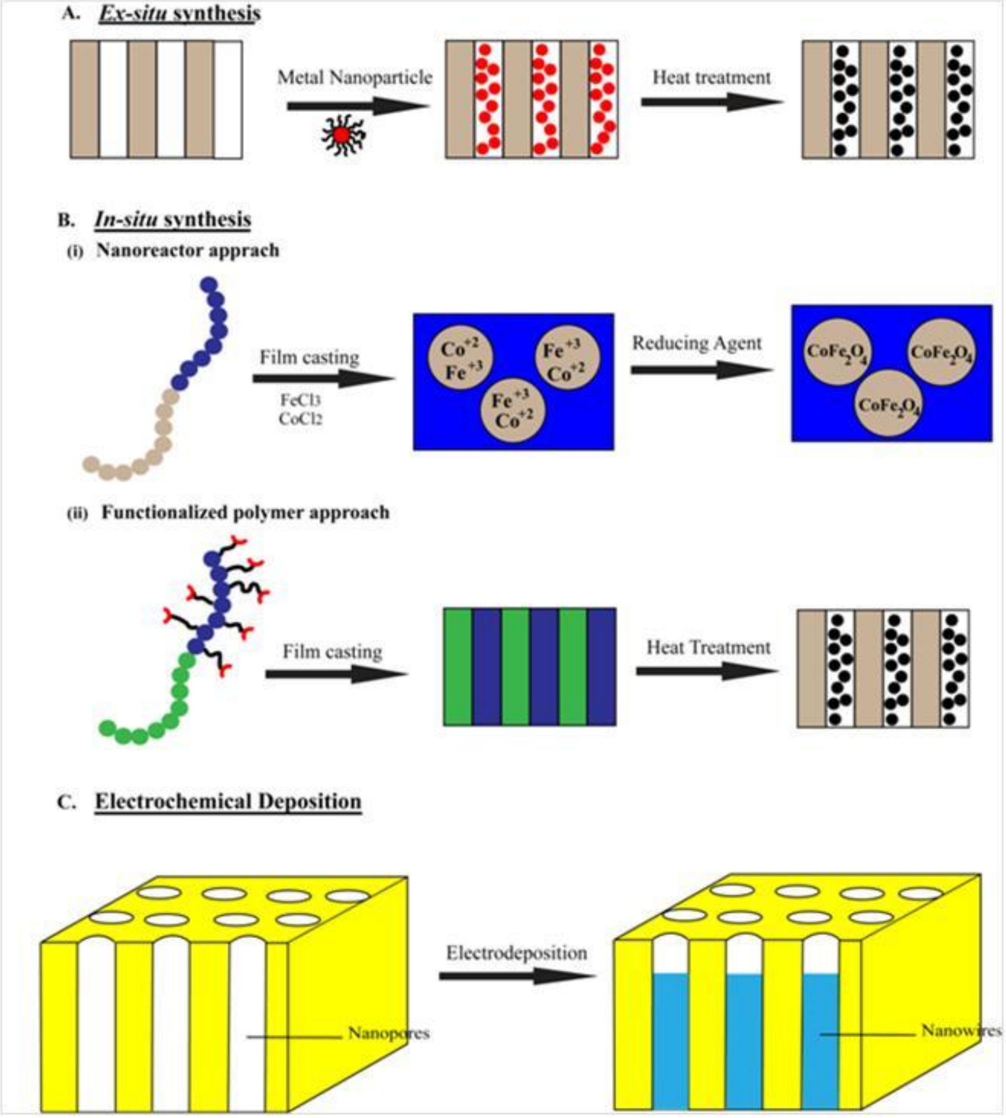

Figure 2.6 Different approaches to fabricate nanostructured magnetic polymer materials. (**a**) In first approach, magnetic nanoparticles (synthesized *ex situ*) are selectively segregated into block copolymer domains. (**b**) In second approach, the block copolymer domains act as nanoreactors for *in situ* synthesis of nanoparticles. (**i**) The metal salts were mixed with BCP and were confined with the BCP domains and were reduced further by either treating with chemical agent or thermal decomposition. (**ii**) The metal precursors are attached to the monomer and polymerized and upon microphase separation are confined within the domains of BCP. After film formation, the metal precursors are converted into magnetic nanoparticles by either thermal treatment or reacting with chemical agent. (**c**) In third approach, one particular block in a nanostructured block copolymer film (in this case, PMMA) is removed by selective etching process to form nanopores. These nanopores are then filled with metals such as cobalt by electrochemical deposition.

. For efficient distribution of nanoparticles within the BCP domains, controlling the interaction between two nanoparticles is very important. Different solvents for casting polymer films were used in order to control the competition of interaction between the nanoparticle and BCP against dipolar interactions between the nanoparticles resulting in different hybrid morphologies.[85] This has been illustrated by dispersing magnetic nanoparticles within the polyisoprene (PI) and poly(2-vinylpyridine) (P2VP) domains of polystyrene-*b*-polyisoprene (PS-*b*-PI) and polystyrene-*b*-poly(2-vinylpyridine) (PS-*b*-P2VP) BCPs respectively.[85, 88] The effect of particle volume fraction, molecular weight of the grafted polymer and aggregation behavior of nanoparticles in them has been studied by selectively dispersing the polymer-grafted magnetite particles in the PMMA domains of the poly(styrene)-*b*-poly(methyl methacrylate) (PS-*b*-PMMA) BCPs.[86, 87] The effect of particle size on the magnetic properties was investigated by incorporating surface modified Fe_3O_4 magnetic nanoparticles within styrene-*b*-ethylene/butylene-*b*-styrene (SEBS) polymer matrix. The magnetic permeability of these nanocomposites increased with increase in the size of nanoparticles.[92] Though the reduction in the aggregation of magnetic nanoparticles has been possible, the complete preclusion has not yet been achieved and confining the nanoparticles into single domain of BCP has not been efficient by this method.

In the second approach, the BCPs act as nanoreactors and the metal nanoparticles are produced *in situ* (See Fig. 2.6b(i)). Initially these nanoreactors are pre-loaded with metal precursors or complexes, which are then reduced either by reacting with other chemical agents or by thermal decomposition to form metal nanoparticles. Cohen's and Kofinas' groups have developed several magnetic nanoclusters within different BCP morphologies by nanoreactor approach and have studied their magnetic properties.[93-100] A diblock copolymer of poly(norbornene-dicarboxylic acid) and poly(norbornene) having carboxylic acid functional group was mixed with $FeCl_3$ and $CoCl_2$ metal salts in solution. These metals have high affinity for the COOH group and hence are attached to one particular block of the diblock copolymer.[94, 95] The polymer solution was cast into a solid film and was then treated with sodium hydroxide (NaOH) and water to yield $CoFe_2O_4$ nanoparticles having an average size of 8.7 nm, uniformly distributed within the polymer matrix with high particle density of 110^9 particles per/cm^2.[94] Though diblock copolymer films exhibited ferrimagnetic behavior at room temperature, nanoparticles were dispersed uniformly in matrix without any ordering

As an alternative approach to chemically reducing the metal complexes, cobalt nanoparticles were grown within the poly(2-vinyl pyridine) domains of poly(styrene-*b*-2-vinyl pyridine) (PS2VP) diblock copolymers by thermal decomposition of organometallic complex, dicobalt octacarbonyl.[101] The diblock copolymer volume fraction was varied to obtain different BCP morphologies and the efficacy of the technique to confine the nanoparticles into one particular domain of BCP was illustrated. The size of the particles formed within the polymer matrix by this approach was found to be bigger than those obtained by chemical reduction method and this may be due to the availability of sufficient thermal energy for the diffusion and growth of nanoparticles. All the magnetic nanocomposites having different morphologies exhibited ferromagnetic behavior at room temperature and was attributed to the large particle sizes (~100 nm) formed. However, the nature of these particles such as crystallinity, which affects their magnetic properties, was not reported. Apart from pure metal nanoclusters such as cobalt and iron, even alloy nanoclusters such as iron-cobalt and cobalt-nickel were also formed within PS2VP BCPs and their magnetic properties as a function of the particle size and composition were studied.[102]

Instead of incorporating the metal salt into BCP domains after the polymer synthesis, metal ion could be attached to polymer chain before polymerization to obtain metal precursors within the BCP domains. Kofinas *et al.* attached cobalt metal ions to the monomer of the BCP and upon microphase separation the cobalt oxide nanoparticles were grown within nano-domains when treated with H_2O_2 (See Fig. 2.6b(ii)).[93] These magnetic nanocomposites having cobalt oxide particles of 4.9 nm uniformly distributed within polymer matrix exhibited ferrimagnetic properties at room temperature. However, no clear microphase separation of BCPs was observed in TEM images. Similarly, Manners *et al.* fabricated room temperature magnetic ceramics by pyrolysis of polyferrocenylsilane (PFS) based homopolymer and BCP.[67, 69, 103-107] However, a very high temperature of 1000 ºC was necessary for the pyrolysis, which destroyed the template. Any lower temperature to retain the polymer template only yielded SPM materials. This approach was then extended to form magnetic alloys such as Fe-Pt, Ni-Pt and Fe-Co.[106, 108] Finally, Grubbs and co-workers, synthesized poly(styrene-*b*-4-(phenylethynyl)styrene) BCPs containing alkyne-functional block and dicobalt hexacarbonyl ($Co_2(CO)_6$) was complexed to the alkyne functionality. These BCP underwent microphase separation and formed regular BCP morphologies.[109] Thermal treatment at moderate temperature of 110 ºC formed cobalt nanoparticles within BCP domains. However, no magnetic characterization of these polymers was reported. A similar approach has been utilized in this work to form nanostructured magnetic polymers and systematic studies were done to derive structure and property relations.

The aggregation of the nanoclusters or particles formed within BCP by second approach was significantly less compared to that observed in materials developed by first approach. Also, attaching the metal ion or complexes directly to the monomer, significantly improved the efficiency of sequestering the nanoparticles to single domain. Another significant advantage of this approach is its ability to obtain magnetic nanostructures with different morphologies that are observed in BCPs such as spherical, lamellar, inverted cylindrical and gyroid.[11, 12, 16] However, control over the size and composition of these nanoparticles has not yet been possible with this method. Further, systematic studies to understand the correlation between structure (morphology) and macroscopic magnetic behavior of resulting nanocomposites were not reported.

In third approach, Russell *et al.* have illustrated the fabrication of well-ordered arrays of ferromagnetic cobalt nanowires with high aspect ratio within the poly(styrene-*b*-(methyl methacrylate)) (PS-*b*-PMMA) BCP films (See Fig 2.6c). Thin films of the BCPs were spin coated onto a silicon wafer and then the PMMA domains are aligned perpendicular to the substrate by application of an electric field. Upon exposure to ultraviolet radiation, the PS domains undergo crosslinking whereas the PMMA domains degrade. The degraded PMMA were removed by treating the films with acetic acid to form nanopores. Subsequently, these nanopores were filled with cobalt by electrochemical deposition to obtain array of nanowires within the diblock copolymer films. Inorganic cobalt cylinders with very high aspect ratio and an ultra-high areal density of 1.9 x 10^{11} cylinders per cm^2 within the polymer matrix were achieved by this approach. The magnetic properties of these ordered arrays of cobalt nanowires were enhanced and exhibited a large coercive field of 800 Oe at room temperature compared to 10 Oe for continuous cobalt film. Fine tuning of aspect ratio, diameter of nanowires and separation between them is possible and tailor their magnetic properties.[110] Excellent control over the crystallinity, aspect ratio and diameter of the nanowires was realized with this method. However, it involves multiple steps including expensive electrochemical deposition procedure. Hence, reduction in the number of processing steps while maintaining the characteristics of this method would be an ideal approach to obtain nanostructured magnetic materials. Apart from cylindrical morphology, it is not possible to apply this method for other morphologies of BCPs.

2.6. Novel Approach: Metal-containing Block Copolymers

In this thesis, novel metal-ion containing BCPs were designed to produce nanostructured magnetic polymers with RTFM properties by simple procedure of microphase separation (solvent film casting) followed by a moderate thermal treatment. In order to achieve this objective, BCPs, with chemical design as shown in Fig. 2.7 and denoted as **ON_{C16}-*b*-ON_{Co}** were proposed. These BCPs were composed of a metal-ion containing block (**ON_{Co}**) and a non-metal containing block (**ON_{C16}**). Significant difference in the solubility parameters of these two blocks (interaction parameter) was expected to drive microphase separation in these BCPs. First of all, according to the design, incorporation of a ferromagnetic metal such as *Fe, Co,* or *Ni* in the metal containing monomer was necessary to obtain nanostructured magnetic materials.

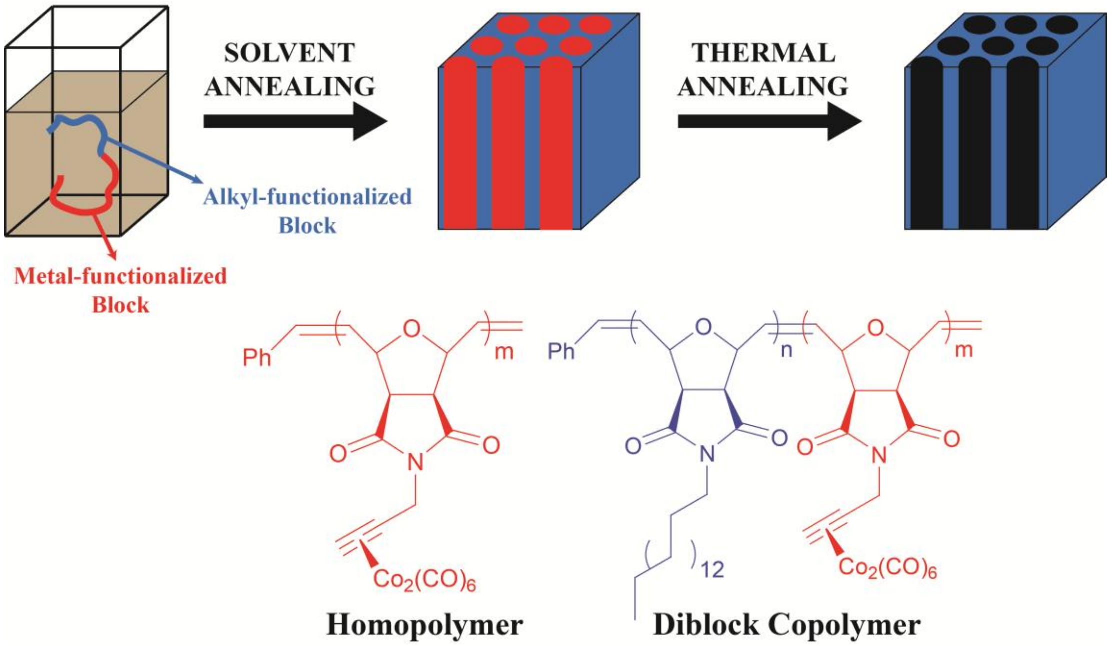

Figure 2.7 Schematic representation of development of nanostructured magnetic materials from cobalt containing BCP. The chemical structure of homopolymer and diblock copolymer is illustrated. The BCP are designed to have metal-functionalized block and alkyl-functionalized block which upon casting into film and solvent annealing yields ordered nanostructured material. Upon thermal treatment at 200 °C, the carbonyl bonds are removed to yield cobalt metal in the microdomains of BCP.

The cobalt metal containing monomer was designed to constitute a dicobalt hexacarbonyl functionality attached to the acetylene bond. It is well known that the dicobalt hexacarbonyl upon heat treatment gets converted into metallic cobalt.[111-114] Similarly, the non-metal containing monomer should have chemical species which are non-magnetic, at the same time should contribute for microphase separation. Therefore, the non-metal containing monomer was designed so that it contained alkyl chain of optimized chain length, necessary to drive microphase separation. In addition, these BCPs should have high molecular weight (M_w) and excellent sequence control. These two attributes were necessary for the microphase separation and to specifically confine ferromagnetic metal ions to one particular block. Fortunately, ring open metathesis polymerization (ROMP) technique using Grubbs catalyst is known to have these capabilities. Previously, metal containing BCPs from metal-coordinated norbornenes using ROMP have been illustrated.[115-118] Hence, norbornene was chosen as the backbone structure for the cobalt metal containing monomers. In order to increase the efficiency of initiation of the second block, the monomer with same core strained cyclic structures (norbornene) was used for non-metal containing block. The synthesis of cobalt functionalized homopolymer and BCPs have been explained in detail in our recently published work.[119]

2.7. Microphase Separation: Tuning Alkyl Chain Length

After successful synthesis of cobalt-containing BCPs, it was necessary to ensure that microphase separation occurs in these materials. Since, the backbones of both the blocks are the same, the alkyl chain length of the non-metal containing block is critical in driving phase separation in them. Without knowing a priori the Flory-Huggins interaction parameter, χ ('chi') and as a starting point, studies were done on the cobalt-containing BCPs (**$\mathbf{ON_{C5}}$-*b*-$\mathbf{ON_{Co}}$**) having alkyl chain length of 5. As an initial screening tool to determine microphase separation, atomic force microscopy (AFM) was used. The BCPs were spin coated on the silicon wafer and the thin film morphology was determined by AFM. The AFM images as shown in the Figure 2.8 indicated limited microphase separation. Hence, two more BCPs having increased alkyl chain lengths, equal to 9 and 16, denoted as **$\mathbf{ON_{C9}}$-*b*-$\mathbf{ON_{Co}}$** and **$\mathbf{ON_{C16}}$-*b*-$\mathbf{ON_{Co}}$** respectively were synthesized. The M_w of all these three BCPs was around 100 kDa. A representative AFM image is shown for **$\mathbf{ON_{C5}}$-*b*-$\mathbf{ON_{Co}}$** and **$\mathbf{ON_{C16}}$-*b*-$\mathbf{ON_{Co}}$** is shown in the Figure 2.8. The AFM images of **$\mathbf{ON_{C16}}$-*b*-$\mathbf{ON_{Co}}$** i.e. with alkyl chain length equal to 16 showed better microphase separation than the other two BCPs. These results were expected as the interaction parameter, χ, increases with increased alkyl chain length and hence better microphase separation. Consequently, all the further studies were carried out on the BCPs containing the alkyl chain length equal to 16 (**C_{16}**).

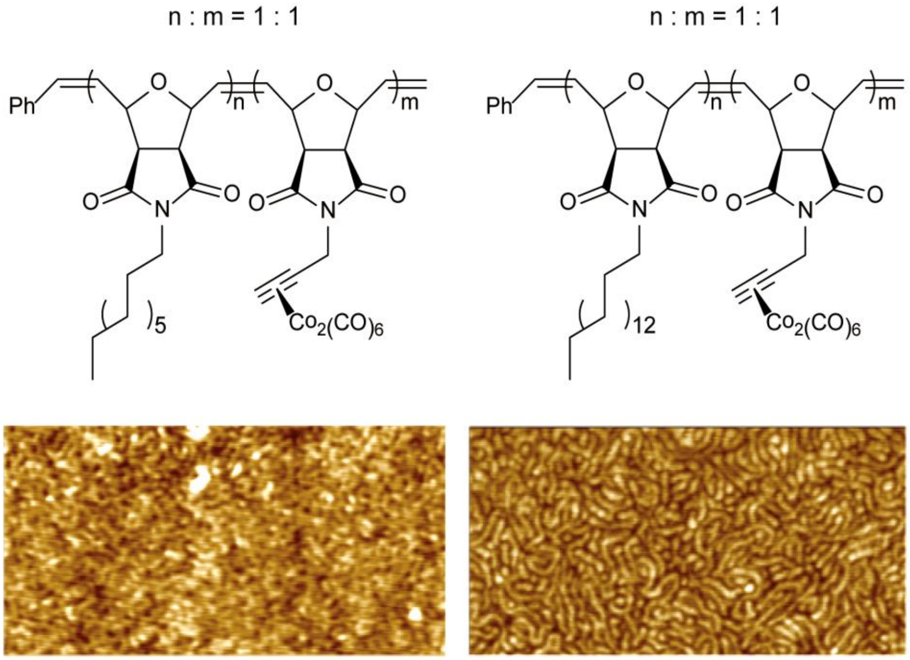

Figure 2.8 AFM images of the cobalt-containing BCP with different alkyl chain lengths a) C_5 and b) C_{16}. The samples were prepared by spin casting thin films of the BCPs on silicon wafer. The AFM image of the BCP containing C_{16} (right) shows better microphase separation than that containing C_5 (left). The M_w of both the BCPs was 100kDa. The size of the AFM images is (1x2 microns)

2.8. Thermal Treatment

After establishing the microphase separation in **ON_{C16}-*b*-ON_{Co}** BCPs, next logical step was to verify the removal of carbonyl ligands from dicobalt hexacarbonyl functionality in them by thermal treatment to yield metallic cobalt. The thermal removal of the carbonyl ligands from metal complexes is well known. More precisely, preparation of cobalt nanomaterials by the thermolysis of cobalt carbonyls has been demonstrated in literature.[119-122] Thermal gravimetric analysis (TGA) was performed on the $\mathbf{ON_{C16}}$-***b***-$\mathbf{ON_{Co}}$ BCP and $\mathbf{ON_{C16}}$ homo polymer at a heating rate of 10 ºC/min under an atmosphere of nitrogen and is shown in the Figure 2.9.

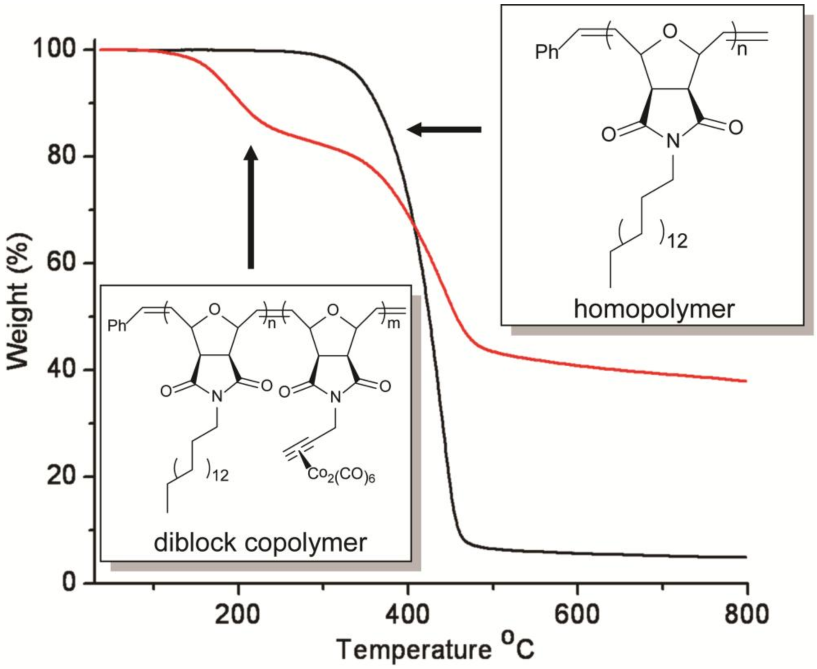

Figure 2.9 TGA of the $\mathbf{ON_{C16}}$ homopolymer and the diblock copolymer $\mathbf{ON_{C16}}$-***b***-$\mathbf{ON_{Co}}$. The C16 homopolymer demonstrates the basic polymer is stable to above 350°C while the cobalt containing block copolymer has a thermal transition starting around 100°C. Using weight loss to calculate carbonyl loss, it is determined that ~95% of the carbonyl ligands have been evaporated.

The TGA results show that the basic polymer of $\mathbf{ON_{C16}}$ homopolymer is stable up to 350 °C whereas, BCP $\mathbf{ON_{C16}}$-***b***-$\mathbf{ON_{Co}}$ has additional thermal transition starting around 100 °C, corresponding to the removal of carbonyl ligands from cobalt metal. Comparison of the theoretical carbonyl weight (18 wt %) and the carbonyl weight loss measured by TGA weight loss (17%) indicated that ~95% of the carbonyl ligands have been evaporated. Apart from such high efficiency of thermal conversion, a wide operating window (100 ºC to 300 ºC) is available allowing for easier processing conditions. However, for simplicity and to ensure the complete removal of metal carbonyls, a temperature of 200 ºC was chosen for thermal treatment for further studies. Considering the success of removal of dicobalt hexacarbonyl by thermal treatment, it was necessary to ensure that the thermal treatment had no impact on the morphology of the BCP.

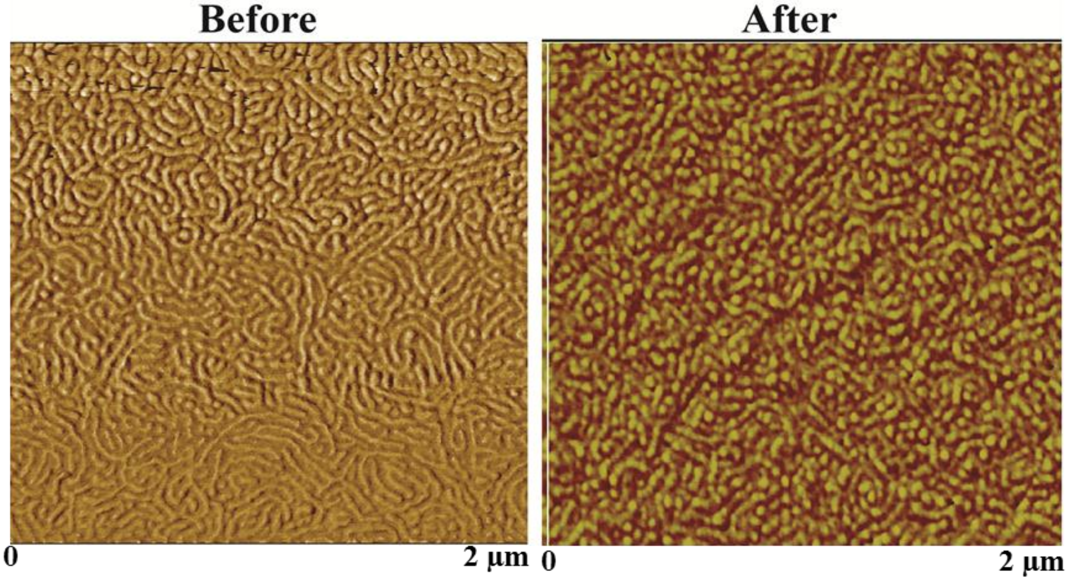

Figure 2.10 AFM images of the BCP, **ON_{C16}-*b*-ON_{Co}** spun coat on a Si wafer, before (left) and after (right) thermal treatment. The cylindrical morphology of BCP thin films was affected by thermal treatment at 200 °C.

The effect of thermal treatment on BCP morphology was studied by AFM. The thin films of BCP, ON_{C16}-b-ON_{Co} were obtained by spin coating a 1 wt% polymer solution on Si wafer. Then the thin of BCP was heat at 200 °C for 6 hours under vacuum. The AFM images of spun coat BCP thin films before and after is shown in the Figure 2.10. These images indicate that the cylindrical morphology of BCP was not affected by the thermal treatment.

2.9. Bulk Morphology

As described above, AFM was used as a characterization technique to determine the microphase separation in the BCPs. However, AFM only provides thin film morphology which is not at equilibrium. In order to determine, the equilibrium or bulk morphology, TEM and small angle x-ray scattering (SAXS) were utilized. The samples were prepared by solution casting a 10 wt% polymer solution (dissolved in chloroform) in a Teflon mold and were then solvent annealed in chloroform environment for 2 weeks. For SAXS characterization, the solution cast polymer films were sandwiched between two kapton films and exposed to X-ray for 1h.

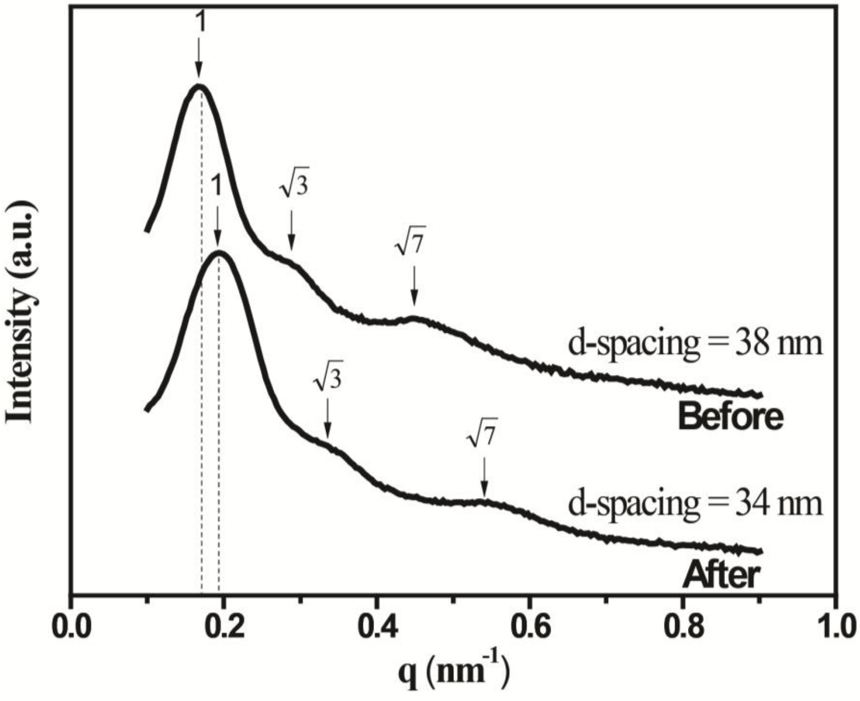

Figure 2.11 SAXS pattern for the BCP, **ONC$_{16}$-b-ON$_{Co}$** before annealing and after annealing. The peak positions were consistent with cylindrical morphology. The SAXS pattern did not change upon thermal treatment.

The SAXS profiles of the BCP, **ON$_{C16}$-*b*-ON$_{Co}$**, before and after thermal treatment are shown in the Figure 2.11. The scattering vectors corresponding to the peak positions in the SAXS pattern are at ratio, q*, $\sqrt{3}$q*, $\sqrt{7}$q* and hence consistent with cylindrical morphology. The domain spacing corresponding to the first order reflection was determined to be ~ 38 – 40 nm. No significant difference was observed in the SAXS profiles of BCP samples obtained before and after thermal treatment except a small change in their d-spacing. This change in d-spacing was consistent with theoretical volume change due to the evaporation of carbonyl moieties from the BCP upon thermal treatment. However, since the change in d-spacing is very small and is in the error limit of SAXS characterization technique, no conclusion was derived by this observation.

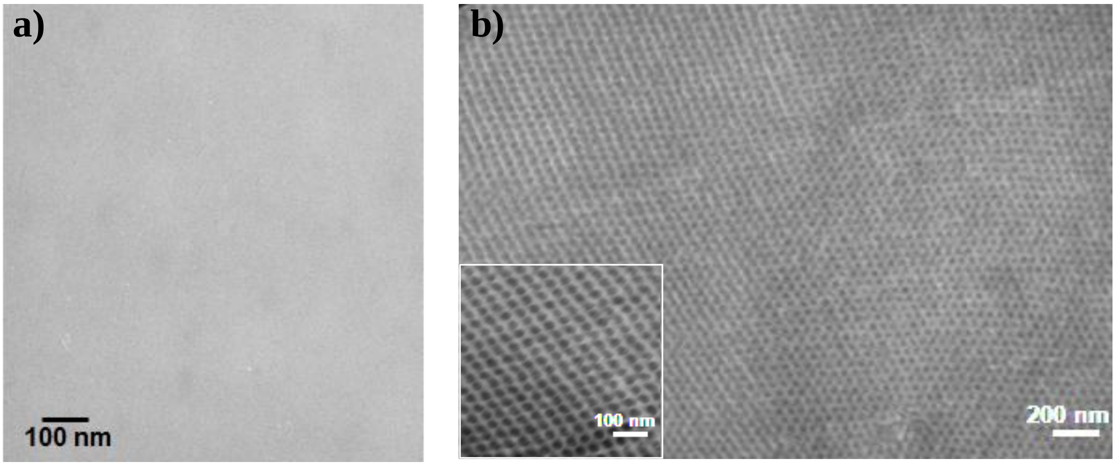

Figure 2.12 TEM images of the solvent annealed homopolymer, $\mathbf{ON_{Co}}$ and BCP, $\mathbf{ON_{C16}}$-***b***-$\mathbf{ON_{Co}}$. a) TEM image of the homopolymer is unstructured and homogenous b) BCP is showing the nanostructured cylindrical morphology.

For TEM studies, the polymer films were fixed to aluminum pin by glue and ultra-thin sections were cut with a diamond knife using a Leica Ultracut Microtome. The unstained TEM images of the BCP $\mathbf{ON_{C16}}$-***b***-$\mathbf{ON_{Co}}$ and homopolymer $\mathbf{ON_{Co}}$ are shown in the Figure 2.12. From TEM images, the homopolymer is unstructured whereas the BCP is nanostructured. The TEM image of BCP indicates that the sample has cylindrical morphology and is quite well ordered over a length of micron. The contrast arises from the presence of cobalt in the cylindrical microdomains. The diameter of the cylinders was found to be ~20 nm and the center-to-center distance of ~40 nm, consistent with the SAXS data.

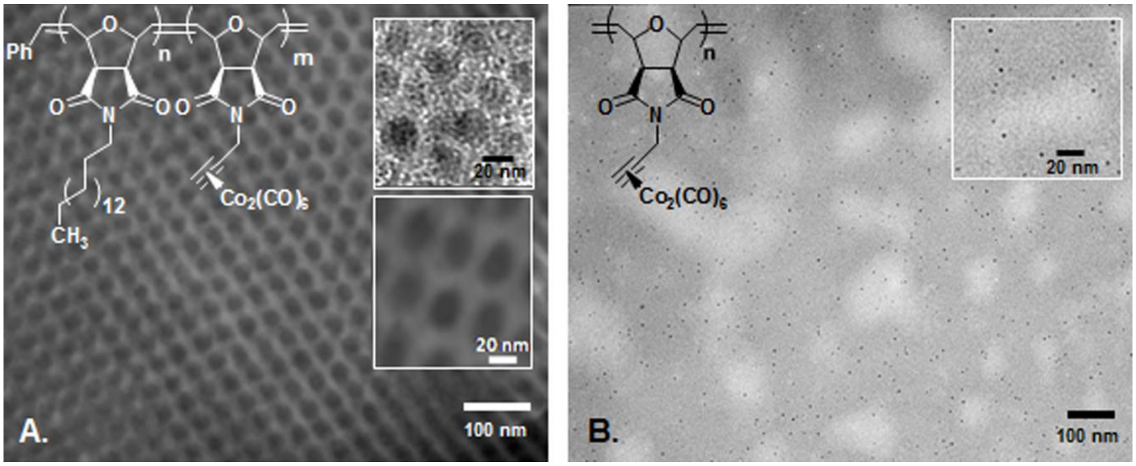

Figure 2.13 TEM images of an unstained, microtomed cross section of a thermally annealed, cobalt-containing a) BCP and b) homopolymer showing the cylindrical microdomain morphology of the BCP and cobalt nanoparticles distributed randomly in the homopolymer. Insets in a) magnify the cylindrical domains with the largest magnification and thinner microtomed section showing small cobalt nanoparticles inside the cylinders.

The TEM image of the thermally annealed BCP as shown in Figure 2.13a clearly shows that the cylindrical morphology is intact even after thermal treatment. Highly magnified TEM images of ultra-thin microtomed slices of the BCP showed the presence of small nanoparticles of size ~2nm within the cylindrical domains (Figure 2.13a inset). The TEM image of the homopolymer without any thermal treatment showed unstructured and homogenous morphology (See Figure 2.12a). However, after thermal treatment, the TEM image as seen in Fig. 2.13b showed a random distribution of similar nanoparticles but of size ~5nm. The high contrast of the nanoparticles in the TEM images of unstained homopolymer and BCP clearly indicates that they are made up of cobalt.

2.10. Structure of Cobalt

2.10.1. Wide-angle X-ray Diffraction

The determination of crystalline and chemical structure of the cobalt nanoparticles was necessary in order to understand the magnetic behavior of thermally annealed homopolymer and BCP. The crystalline structure of the cobalt was investigated by both wide angle X-ray diffraction (WAXD) and selected area electron diffraction (SAED). Similarly, the chemical structure of the cobalt was investigated by X-ray Photoelectron spectroscopy (XPS) and near edge X-ray absorption fine structure (NEXAFS) characterization. The crystalline nature of the cobalt nanoparticles formed in the thermally annealed homopolymer and BCP was investigated using WAXD and spectrums are shown in Figure 2.14. No peaks corresponding to crystalline cobalt were observed in the WAXD profiles of both homopolymer and BCP which are thermally treated at 200 °C (Figs 2.14b and 2.14c).

The absence of crystalline peaks might be due to their amorphous structure or due to their extremely small sizes. To rule out one of the possibilities, crystalline cobalt nanoparticles, having an average diameter of 5 nm (same size as that seen homopolymer), were grown by known solution methods and mixed with th**e ONC$_{16}$** homopolymer so that total cobalt content was 10 wt%, lower than the cobalt content of the BCP or homopolymer samples. A crystalline peak was observed in the WAXD spectra of this nanocomposite (Figure 2.14a).

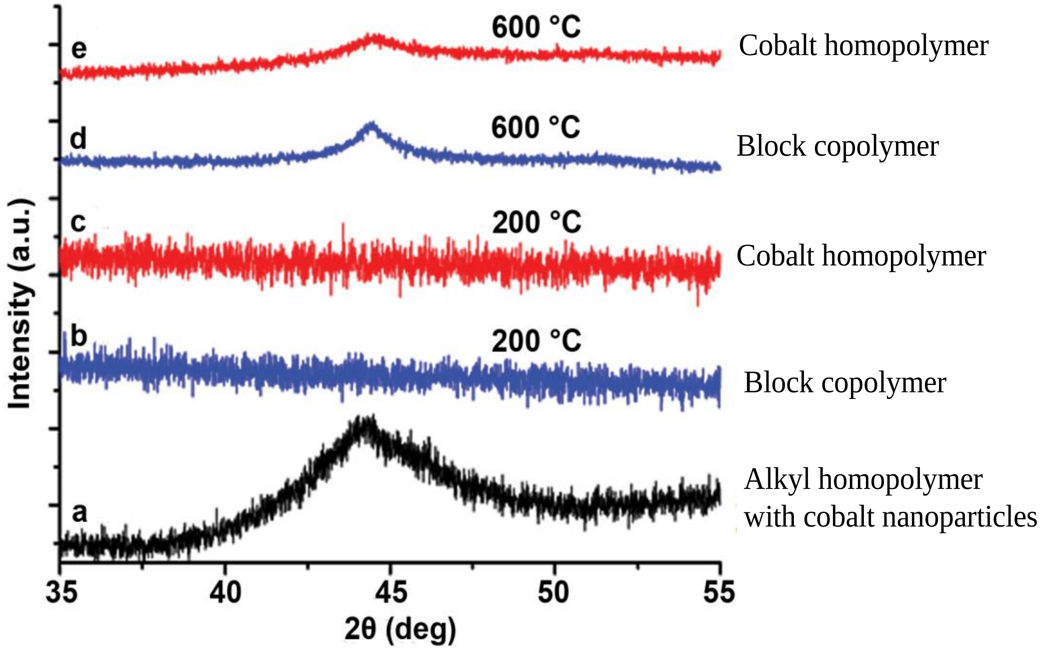

Figure 2.14 WAXD profiles of a) a 10 wt% blend of solution prepared by mixing crystalline Co nanoparticles in the C_{16} containing homopolymer, b) BCP and c) homopolymer heated at 200°C, and pyrolyzed samples of the d) BCP and e) homopolymer at the 600 ^{o}C, which removes all the organic ligands and allows the Co present to crystallize.

Thus the absence of reflections in WAXD spectrum cannot be attributed due to the effect of size or concentration of nanoparticles. The WAXD spectrum of both homopolymer and BCP which are thermally treated at 600 °C showed crystalline peaks and is shown in Figures 2.14d and 2.14e. The temperature of 600 °C was high enough for the removal of the organic material and the cobalt present in the sample was able to crystallize. Further, the SAED of Co-containing BCP and homopolymer samples heated at 200 °C showed no crystalline diffraction spots but a halo ring indicating amorphous structure (See Figure 2.15).

Figure 2.15 Selected area electron diffraction (SAED) of thermally annealed diblock copolymer showing a halo ring, indicating amorphous cobalt.

2.10.2 Chemical State of Cobalt by NEXAFS

The chemical structure of the cobalt nanoparticles was initially investigated by XPS. It is a surface sensitive technique and has a penetration depth of only 5nm. The presence of cobalt and other organic species were confirmed by XPS. Considering the low concentration of cobalt (~13%), the signal from cobalt species were not significant enough to determine their oxidation state. Therefore, near edge X-ray absorption fine structure (NEXAFS) spectroscopy of the BCP and homopolymer before and after heat treatment confirmed the presence of only Co^0 species within the polymers (see Figure 2.16).

The peak position of Co L_{III} edge is shifted to lower energy (1.5 eV) indicating the decarbonylation of dicobalt hexacarbonyl after heat treatment in both homopolymer and BCP. A single, absorption edge was observed at 781 eV in both homopolymer and BCP after heat treatment and peak splitting was not observed.

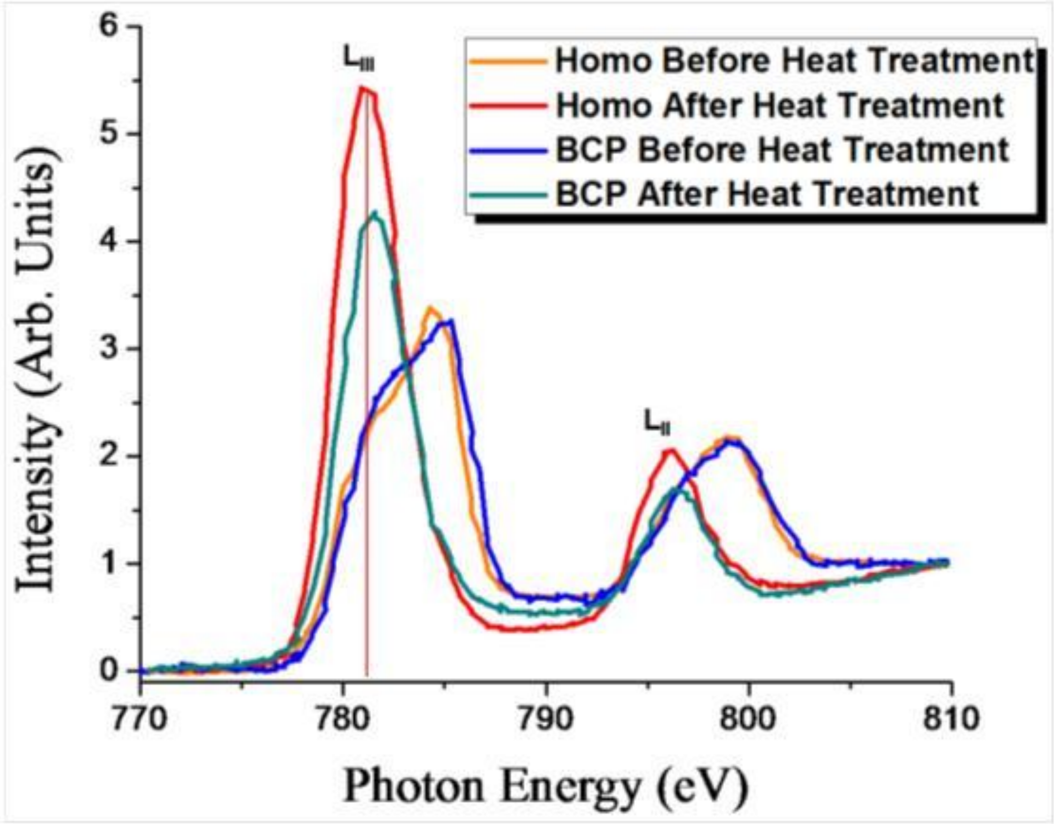

Figure 2.16 The chemical state of cobalt was investigated by Near edge X-ray absorption fine structure (NEXAFS) spectroscopy of the BCP and homopolymer before and after heat treatment.

This peak shape is consistent with that of cobalt foil (Co^0 species) reported in the literature.[123] In NEXAFS of nanosized cobalt particles, the Co L_{III} peak was shifted higher by 1.5eV than bulk cobalt foil, which is also consistent with formation of small Co^0 nanoparticles within polymers. This confirmed the formation of small cobalt metal nanoparticles in the both homopolymer and BCP.

2.11. Characterization of Magnetic Properties

2.11.1 Static Magnetic Properties

Both BCP and homopolymer films after solvent annealing were brown in color and turned to black upon heating indicating the formation of cobalt nanoparticles in both of them. However, as shown in the Figures. 2.17a and 2.17b, upon brining a permanent magnet closer to them, the behavior of BCP was markedly different from that of the homopolymer. The BCP is attracted to the permanent magnet like a ferromagnet whereas the homopolymer did not, indicating that it was nonmagnetic in nature at room temperature. In order to understand this contrasting magnetic behavior more quantitatively, a magnetic characterization of these materials was carried out by Superconducting Quantum Interference Device (SQUID) magnetometer to determine their static magnetic properties. Magnetization versus applied field curves (M-H curves) of thermally treated BCP and homopolymer obtained from SQUID magnetometer is shown in the Figs. 2.17c and 2.20d respectively. The BCP exhibited a RTFM behavior whereas the homopolymers exhibited SPM behavior at room temperature. From the magnetic hysteresis curve of BCP, the values of saturation magnetization (M_s), remnant magnetization (M_r) and coercivity (H_c) were determined to be 3.5 emu/g, 0.61emu/g, and 200Oe respectively. In spite of having similar chemical structure and higher loading of the cobalt, the homopolymer exhibited SPM behavior in contrast to the ferromagnetic behavior in BCP. Interestingly, the size of cobalt particles formed in BCP (~2 nm) is smaller than to that formed in homopolymer (~5 nm). Previous reports having the particles in this size range (less than or equal to 5nm) have exhibited SPM behavior.[124,

[125] Thus, a detailed magnetic characterization was necessary to answer the question, how these SPM particles within BCP could contribute to their RTFM behavior.

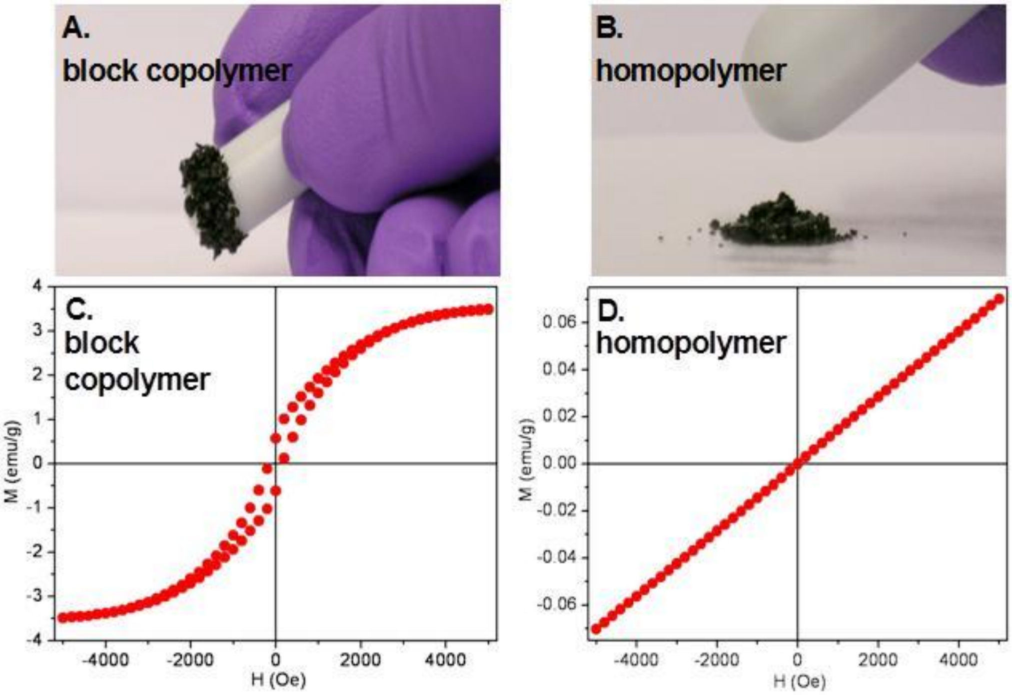

Figure 2.17 The room temperature response of the thermally annealed a) BCP and b) homopolymer to a magnet along with SQUID magnetometer measurements to quantify their magnetic properties. The c) BCP is ferromagnetic at room temperature, while the d) homopolymer is paramagnetic.

The temperature dependent magnetic behavior of homopolymer and BCP was determined by performing, zero-field cooled (ZFC) and field-cooled (FC) experiments. Magnetization under zero-field cooled and field-cooled conditions as function of temperature for both homopolymer and BCP was obtained using SQUID magnetometer by applying a probe field, H = 100 Oe and are shown in Figure 2.18. In order to determine the ZFC curves, the samples were cooled to a low temperature (2K) in the absence of field (zero field) and at low temperature a low magnetic field of 100 Oe was applied and the magnetization was measured by slowly increasing the temperature till room temperature (325 – 350 K). On the contrary, for FC curve, a small magnetic field of H=100 Oe was applied at room temperature and the sample was cooled to a low temperature. At low temperature, the magnetization was measured as the temperature was increased slowly. At low temperatures, non-interacting nanoparticles assume a blocked state i.e. their magnetic moments are frozen in random orientation and most of them will not be able to orient in the direction of the applied field. As the temperature increases, the ZFC curve increases gradually due to progressive unblocking of particles of increasing size, as they would have sufficient thermal energy to reorient themselves in the direction of applied field. The ZFC peak reaches a peak maximum corresponding to mean blocking temperature (T_B), and then decreases on further increase in temperature, exhibiting a paramagnetic-like behavior i.e. following a Curie-Weiss law. At higher temperatures (> T_B), the magnetic moments would have sufficient or excess thermal energy and hence can undergo spontaneous magnetization reversals. Thus, at blocking temperature a transition from ferromagnetic to SPM behavior occurs.[126, 127] The ZFC and FC curves bifurcate at $T_{irr,}$ irreversible temperature corresponding to the temperature above which the magnetization versus applied field will not have any hysteresis and below which it exhibits hysteresis. Generally, the T_B depends on the average particle size and T_{irr} corresponds to the blocking of largest particle size. Hence, the separation between the T_B and T_{irr} is a qualitative measure of particle size distribution.[128] In magnetic nanoparticle systems with narrow particle size, the T_B and T_{irr} coincide with each other and thus often T_{irr} is considered as blocking temperature when the peak maxima in ZFC curve is not distinct.

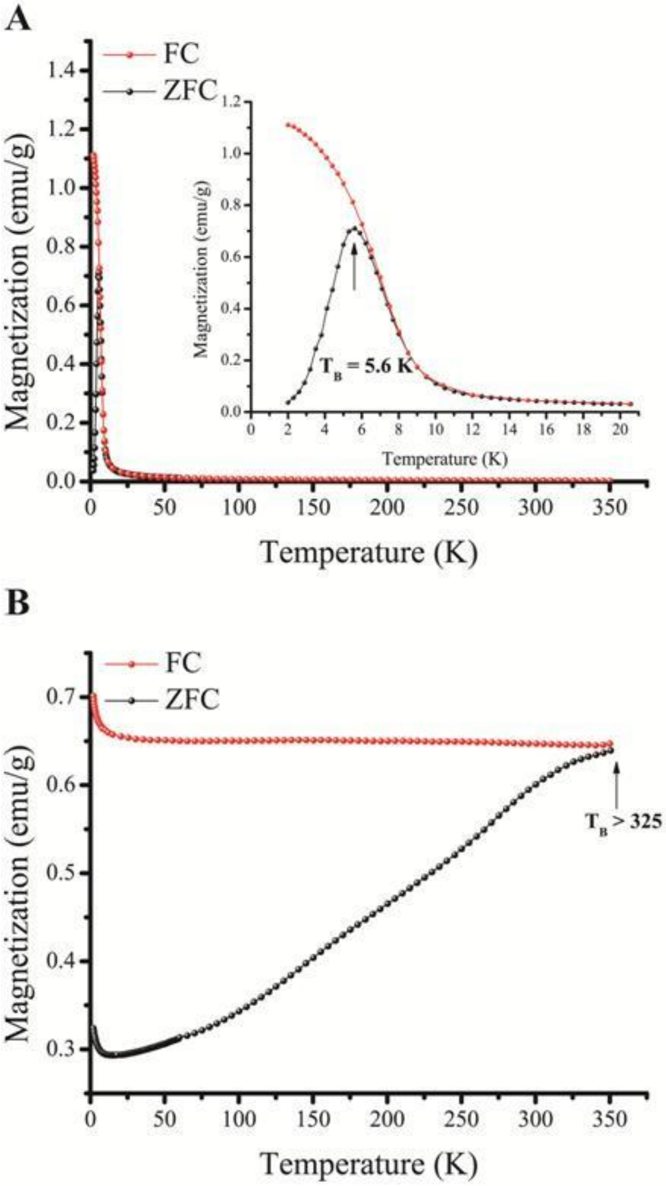

Figure 2.18 Zero field cooled (ZFC) and field cooled (FC) curves of cobalt metal containing a) homopolymer and b) BCP with cylindrical morphology at 100 Oe applied field. The inset in a) is magnified portion of the curve depicting the peak in ZFC corresponding to mean blocking temperature (T_B) The homopolymer exhibited typical superparamagnetic behavior and the BCP RTFM behavior (T_B > 325).

The ZFC and FC curves for homopolymer exhibits a typical SPM behavior with a peak maximum in ZFC curve at 5.6K corresponding to mean blocking temperature. The ZFC and FC curve bifurcate at 12K, corresponding to T_{irr} and is consistent with onset of hysteresis in magnetization versus applied field curves at 4K (Figure 2.19). The small difference between the T_B and T_{irr} indicate a narrow particle size distribution and is consistent with 4.5 nm cobalt nanoparticles observed in the TEM images of thermally annealed homopolymer sample.

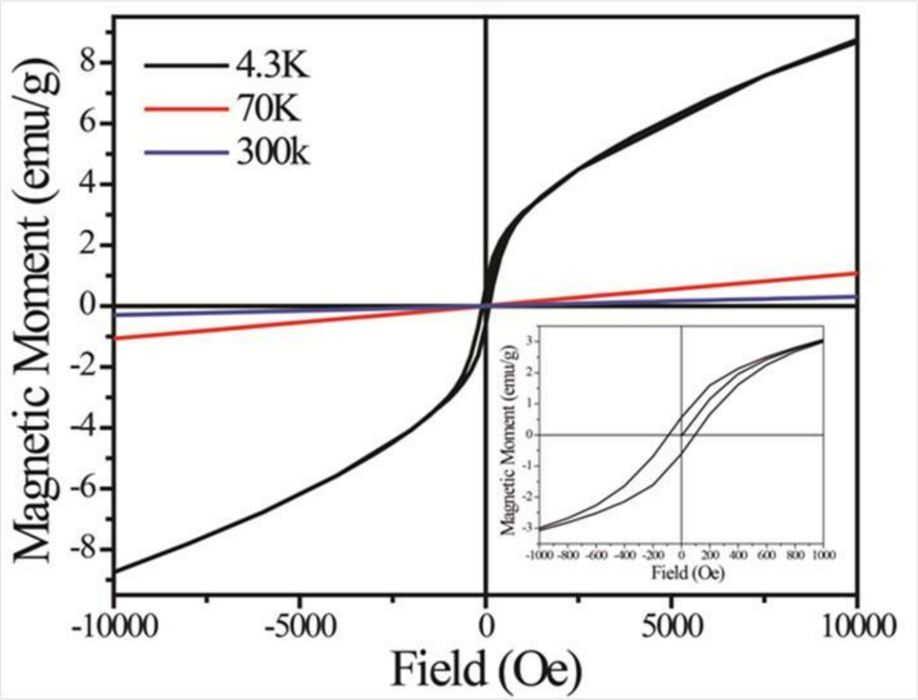

Figure 2.19 Magnetization as a function of applied field (M-H curves) for homopolymer at various temperatures. The onset of magnetic hysteresis at temperatures less than 10 K (4.3 K) is illustrated. The M-H curve at 4.3K is magnified to show the magnetic hysteresis (inset)

On contrast, ZFC of BCP with cylindrical morphology increased continuously with increase in temperature and no peak maximum was observed till the temperature of 350K, indicating a very broad distribution of blocking temperatures. The blocking temperature is related to the particle size and hence indicates the presence of a broad particle size distribution in thermally annealed BCP with cylindrical morphology. The ZFC and FC curves for BCP do not combine even at 350K indicating irreversibility at room temperature. This is consistent with ferromagnetic behavior and hysteresis from magnetization versus applied field curves at room temperature. On the contrary to results from ZFC and FC measurements, only small nanoparticles or clusters of size 2 - 3 nm were observed in the TEM images of thermally annealed BCP sample. In cobalt nanoparticle systems, a size of at least 13 nm is required to show a RTFM behavior or blocking temperature above 300 K, indicating that the individual cobalt nanoparticles are not contributing for the RTFM behavior observed in the BCP samples. The FC curve of BCP increases very gradually with decrease in temperature, which is indicating strong dipolar interactions between the cobalt particles. Magnetic coupling between nanoparticles suppresses the thermal fluctuations and thus increase in net magnetization is inversely related to the interparticle coupling.[129, 130] The interparticle dipolar interactions are also known to increase the blocking temperatures of SPM particles.[47, 49-51, 129, 131-137] At low temperatures, i.e. at 12K, ZFC curve increased steeply with decrease in temperature, but no peak was observed till 2K. This paramagnetic-like behavior as function of temperature might be due to the presence of small nanoparticles or clusters of 2-3 nm observed in TEM images of BCP. This may also be due to the free cobalt atoms, which are not incorporated into nanoparticles. The surface atoms present at the interface between nanoparticles and organic materials within the cylindrical domains is another possibility. The inverse of magnetization in this temperature range was not a linear function of temperature and thus is not following a Curie law (see Figure 2.20). Hence, it is non-trivial to conclusively determine the phenomena among these three possibilities, contributing for this low temperature paramagnetic like behavior. Considering the exponential increase in the magnetization as a function of temperature, most likely it is due to the free atomic cobalt atoms. These will have rotational freedom and hence their magnetic moments will be fluctuating, till very low temperatures. Further, due to their very small size, they can align in the direction of the field even at very low temperatures.

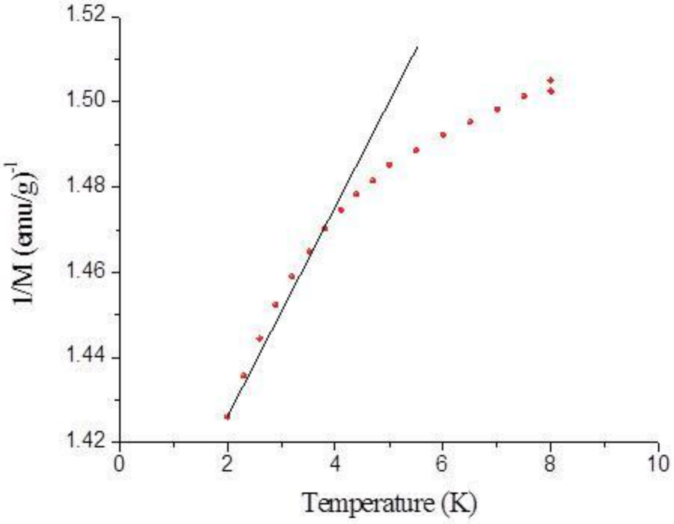

Figure 2.20 The inverse magnetization of BCP in lower temperature region. The inverse magnetization increased exponentially as a function of temperature and hence did not follow curie law. A straight was drawn for guidance of eye.

2.11.2. Dynamic Magnetic Properties

In order to evaluate the relaxation time and the actual energy barriers for magnetization reversal in thermally annealed homopolymer and BCP, the temperature dependence of the ac susceptibility was measured in the frequency range 30 – 10^4 Hz. The in-phase (real) and out-of-phase (imaginary) components of AC magnetic susceptibilities of both the homopolymer and the BCP with cylindrical morphology as function of temperature at different frequencies are shown in the Figure 2.21. The AC susceptibility curve as a function of temperature for homopolymer, shown in Figure 2.21a, exhibited SPM behavior similar to single domain nanoparticles. At low temperatures the χ’ (in-phase component) of homopolymer showed a steep rise with peak maximum observed in the range of 6.6 to 7.4 K. The peak maximum in χ’ shifts to lower temperatures and gains intensity with decreasing frequency. The out-of-phase component, χ”, also shows a frequency-dependent peak maximum in the 5.8 to 6.5 K region. The peak maximum in χ” shifts to lower temperatures and become less intense with the decreasing frequency. All these observations are consistent with SPM behavior observed from both ZFC and FC measurements and the magnetic hysteresis measurements.

For an ensemble of nanoparticles, the relaxation of magnetization M(t) to its thermal equilibrium value M_0 is characterized by

$$M(t) = M_0\left(1 - e^{-\frac{t}{\tau}}\right) \tag{4}$$

where τ is the relaxation time and according to equation 3, follows the Arrhenius law for thermal activation over the anisotropy energy barrier $E_B = KV$. (V is the volume of the particle and K is the anisotropy energy density).

A common step to analyze magnetic relaxation is by a well-known Arrhenius plot that gives a straight line if the process is governed by thermal activation. The blocking temperatures or the temperatures corresponding to peak maximum (T_B) in χ’(T) for homopolymer was derived from the curve in Figure 2.21a. Then, $\tau = {}^{1}/_{2\pi f}$ (where, f is the frequency) is plotted as function of $1/T_B$ as shown in the Figure 2.22. It exhibited a linear relationship indicating the magnetization reversal process in homopolymer is a thermally activated one. Further, from the intercept and slope of this line intrinsic relaxation constant, τ_0 and the ratio ${}^{E_B}/_{k_B}$ were determined respectively.

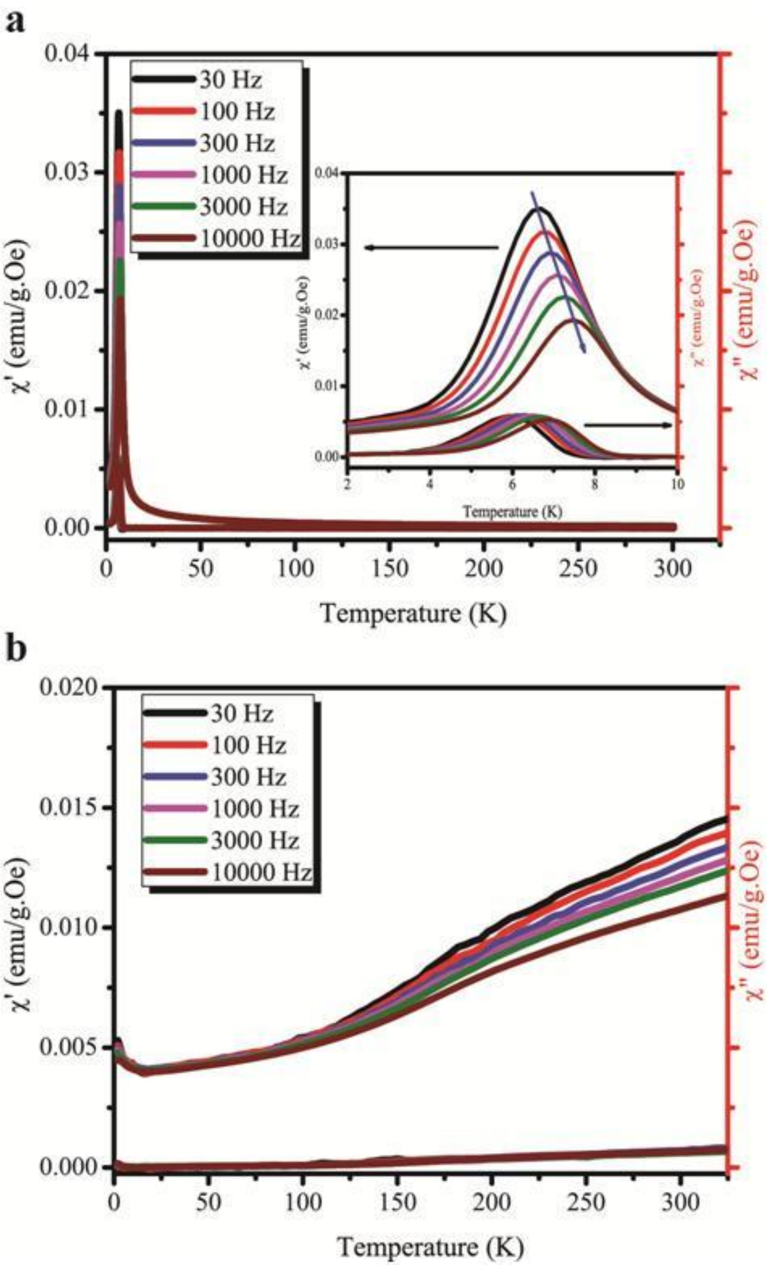

Figure 2.21 Temperature dependence of the in- and out-of-phase components, χ' and χ", of AC susceptibility measured at various frequencies (30 Hz – 10 kHz) for a) homopolymer and b) BCP with cylindrical morphology with an AC field of 5 Oe was applied. The AC susceptibility of homopolymer at low temperature is magnified and is shown as inset in a) depicting the frequency dependency. The peak maximum (T_B) for different frequencies is utilized to plot according to Arrhenius equation in Fig. 2.22.

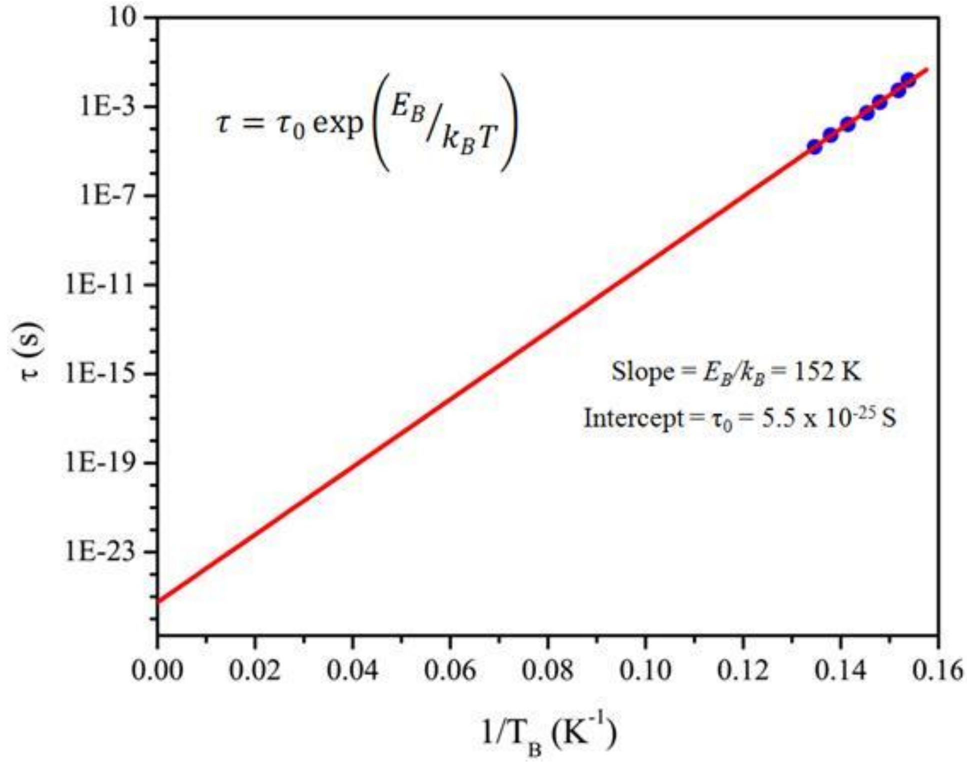

Figure 2.22 Arrhenius plot for the relaxation time of homopolymer.

From the intercept of Arrhenius plot, the intrinsic relaxation time was found to be equal to τ_0 = 5.5 x 10^{-25} s. Usually, the values for intrinsic relaxation times for non-interacting system SPM and ferromagnetic nanoparticles are in the range of 10^{-9} and 10^{-13} s.[138] Reasons for such unphysical values of relaxation time are not clearly understood but mostly attributed to interparticle interactions, shape anisotropy and magnetocrystalline anisotropy.[139-141] The value of $\boldsymbol{E_B}/\boldsymbol{k_B}$ was found to be around 152 K, where k_B is Boltzmann constant. Hence, the energy barrier E_B was found to be equal to 2.098 x 10^{-21} J. Considering a spherical particles of diameter equal to 5 nm, the K_{eff} for cobalt particles was determined to be equal to 1.0074 x 10^5 Jm^{-3}.

The out-of-phase (χ”) and in-phase (χ’) components of ac susceptibility as function of temperature for BCP at different frequencies are shown in Figure 2.21b. The values of χ”(T) at different frequencies were very low and hence no clear interpretation of the data could be derived. The χ’(T) at different frequencies increased with increase in temperature and no peak maximum was observed till 325 K. This observation is consistent with the ZFC magnetization measurements for BCP. The increase in the frequency dependency of χ’(T) with increase in temperature is indicating that the T_B is close to 350 K (or even higher temperatures). Since, no peak maximum was observed in the χ’(T) curve at different frequencies, obtaining information regarding the relaxation time and energy barrier was not possible.

2.12. Origin of Ferromagnetic Behavior in Block Copolymer

In spite of having similar chemical structure, the nanostructured cobalt-containing BCP and the unstructured homopolymer, upon heat treatment exhibited different magnetic behaviors at room temperature. Upon thermal treatment, the formation of SPM cobalt nanoparticles (less than 5 nm) was observed by TEM in both of these polymers. However, the nanoparticles in the case of BCP were confined within the cylindrical domains whereas in the case of homopolymer they were randomly distributed within polymer matrix (see Figure 2.13). The oxidation state of the cobalt nanoparticles, formed in both homopolymer and BCP upon heat treatment was found to be zero by NEXAFS studies. The WAXD and SAED studies on them did not indicate any crystallinity. The size of the nanoparticles formed within them is in SPM regime. Thus, it is expected that, these polymer nanocomposites would exhibit a superparamagnetic behavior.

The magnetic behavior of the homopolymer is consistent with superparamagnetic behavior. It exhibited only a paramagnetic behavior at room temperature but a ferromagnetic behavior at temperatures less than 10 K. The peak maximum at 5.6 K observed in ZFC curve is consistent with their SPM behavior. The frequency dependency of the peak maximum in AC susceptibility measurements also confirmed the SPM behavior of the homopolymer with a T_B = 5.6 K. On contrary, the BCP exhibited a ferromagnetic behavior at room temperature in M-H measurements. The ZFC and FC measurements and ac susceptibility measurements of BCP indicated a broad distribution of particle sizes in them and its blocking temperature is higher than 325 K, consistent with their ferromagnetic behavior at room temperature. This result is in contrast with the TEM studies of thermally annealed BCP, in which the size of the particles were found to be in SPM regime (< 5 nm). Based on above results, it can be hypothesized that the nanoconfinement within the cylindrical domains of BCPs has increased the dipolar interactions between these SPM cobalt particles significantly, to induce an additional ordering between them. Therefore, they collectively contribute to the RTFM behavior of BCP. Additionally, the cylindrical morphology of the BCP domains can impart shape anisotropy to this ensemble of nanoparticles. This observation in BCP is in direct comparison and consistent with the studies from Gross *et al.,* in which, the SPM cobalt nanoparticles were incorporated within the nanopores of hexagonal honeycomb mesoporous silica [129]. The nanoconfinement of single-domain SPM cobalt nanoparticles within nanopores resulted in a constructive magnetic coupling and induced an additional ordering between them to yield RTFM behavior. In comparison, both non-interacting system of dilute cobalt particles and a randomly interacting system such as concentrated particles resulted in lower coercivity. As described above, an ensemble of SPM particles can exhibit SPM, SSG and SFM behavior depending on the strength of interparticle interactions. The cobalt particles are randomly distributed within the matrix of thermally annealed homopolymer. The random and weak interactions between cobalt particles within unstructured homopolymer have resulted in collective or regular SPM behavior. Thus nanostructuring due to microphase separation of BCP are critical in imparting RTFM behavior to these materials.

CHAPTER 3

EFFECT OF BLOCK COPOLYMER MORPHOLOGY ON MAGNETIC PROPERTIES OF COBALT-CONTAINING DIBLOCK COPOLYMERS

3.1 Introduction

In the previous chapter, the development of novel cobalt-containing BCPs, designed to produce nanostructured magnetic polymers with RTFM properties due to microphase separation was demonstrated. The BCP consisted of an alkyl-functionalized block and a cobalt-functionalized block, which microphase separated to give a cylindrical morphology. Upon a heat treatment at 200 °C, the nanostructured materials exhibited RTFM behavior, whereas the unstructured homopolymer material exhibited only superparamagnetic (SPM) behavior, in spite of having similar chemical structure and a higher loading of cobalt. The formation of SPM cobalt nanoparticles, less than 5 nm, was observed in both polymers after their heat treatment. The nanoparticles in the case of BCP were confined within the cylindrical domains whereas in the case of homopolymer they were randomly distributed within the polymer matrix. The sizes of the nanoparticles formed within the polymers are in the SPM regime, and it was hypothesized that the RTFM behavior of the BCP was due to the collective behavior of these SPM cobalt particles. The increased dipolar interactions between the SPM cobalt particles under the nanoconfinement of cylindrical morphology resulted in their ferromagnetic behavior, signifying the importance of nanostructuring on the magnetic properties of these materials.

As described in the previous chapter, the BCPs exhibit various bulk morphologies as a function of block length ratio (or volume fraction). Therefore, it is apt to study the effect of BCP morphology on the magnetic properties of cobalt-containing BCPs in order to further support the hypothesis that the RTFM properties arise from the nanostructured confinement of the BCP microdomains. The advantage of this study is that all the BCP morphologies are nanostructured and also ordered. Additionally, different BCP morphologies have different shape anisotropy. It is well known that shape anisotropy plays an important role in the properties of magnetic materials. Cylinders are usually considered one dimensional (1D) objects (with 2D confinement); lamellae are 2D objects (with 1D confinement); the matrix phase of inverted cylinders is considered a 3D object constrained between cylinders.

A series of cobalt-containing BCPs were synthesized according to the procedure described in the previous chapter, such that their morphologies were varied between the cylindrical, lamellar, and inverted cylindrical phases by varying the block length ratios (or volume fractions). The details of the synthesis of these BCPs along with their characterization will be published elsewhere.[142] The BCPs were characterized by NMR and GPC, and their characteristics are listed in Table 3.1. All the BCPs have similar molecular weights (MWs) and narrow polydispersity indices (PDIs). The BCPs were dissolved in chloroform and bulk polymer films were cast and solvent annealed according to the procedure described in previous chapter. The bulk morphology of these solvent-annealed bulk films was characterized by both SAXS and TEM and tabulated in Table 3.1. Finally, these films were thermally annealed at 200 ºC under vacuum for 6 hours and their static as well as dynamic magnetic properties were determined.

Table 3.1 Details of the cobalt-containing block copolymers with different block copolymer morphologies.

Polymers	f_{co}[a]	Cobalt wt%[b]	M_n (kDa)[c]	PDI[c]	Morphology[d]	d-spacing (nm)[e]
Poly1	32	8	82.1	1.11	Cylindrical	38
Poly2	39	11	75.8	1.12	Cylindrical	40
Poly3	50	13	73.5	1.12	Lamellar	35
Poly4	56	16	79.6	1.10	Lamellar	31
Poly5	65	18	73.7	1.12	Inverted Cylindrical	25

[a] Volume fraction of the cobalt-functionalized block (f_{Co}), as calculated based on density data obtained by the gradient density column method. [b] Theoretical mass percentage of cobalt in the diblock copolymers before the heat treatment, as calculated based on their chemical structures. [c] Determined by gel permeation chromatography (GPC) in THF using a refractive index (RI) detector, relative to polystyrene standards. [d] Determined by small angle X-ray scattering (SAXS) and transmission electron microscopy (TEM). [e] Bulk periodicity before the heat treatment, $d = 2\pi/q^*$, where q^* is the primary scattering peak as determined by SAXS.

3.2. Morphological Characterization by SAXS and TEM

Both SAXS and TEM were used to characterize the bulk morphologies of diblock copolymers with different block length ratios, before and after heat treatment. **Poly1** is similar to BCP (**ON$_{C16}$-*b*-ON$_{Co}$**) with cylindrical morphology described in the previous chapter. The morphological and also magnetic characterization details of **Poly1** can be directly compared to those discussed for BCPs with cylindrical morphology in previous chapter.

The SAXS profiles of **Poly4,** both before and after thermal treatment are shown in Figure 3.1(b). The reflections in the SAXS profile of **Poly4** were observed at q^*, $2q^*$ and $3q^*$, which is consistent with lamellar morphology. Representative TEM images of **Poly4**, before and after thermal treatment, are shown in the Figure 3.2(a) and 3.2(b). The d-spacing between lamellae was approximately ~32 – 34 nm and the dimensions of the cobalt-containing domains were 11 – 13 nm.

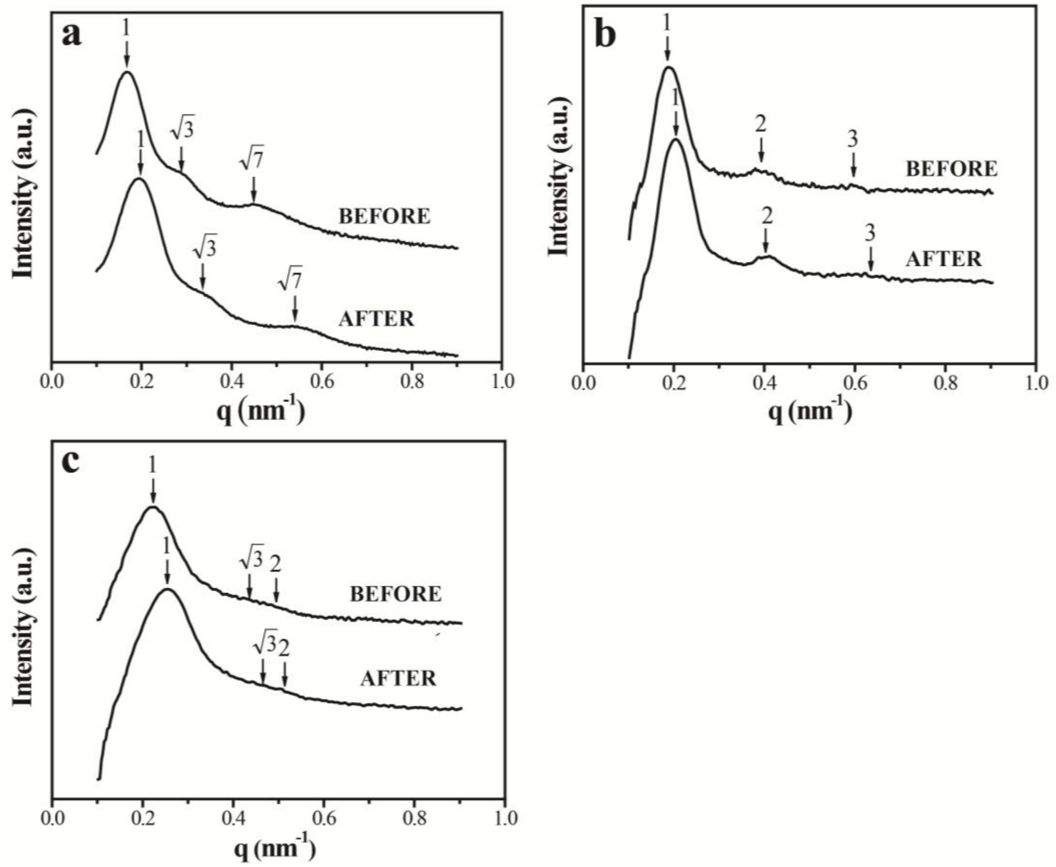

Figure 3.1 Representative SAXS profiles of cobalt-containing BCPs with a) cylindrical (**Poly1)** b) lamellar (**Poly4**) and c) inverted cylindrical (**Poly5**) morphology. SAXS profiles of each sample before and after heat treatment are compared to observe the effect of thermal treatment on bulk morphology.

The morphology of **Poly4** after the heat treatment was not significantly different from the one before annealing. The formation of cobalt nanoparticles in the BCP structures was observed by TEM (Figure 3.2b), similar to the **ON_{Co}** homopolymer and **Poly1,** but they were larger and randomly distributed in both phases.

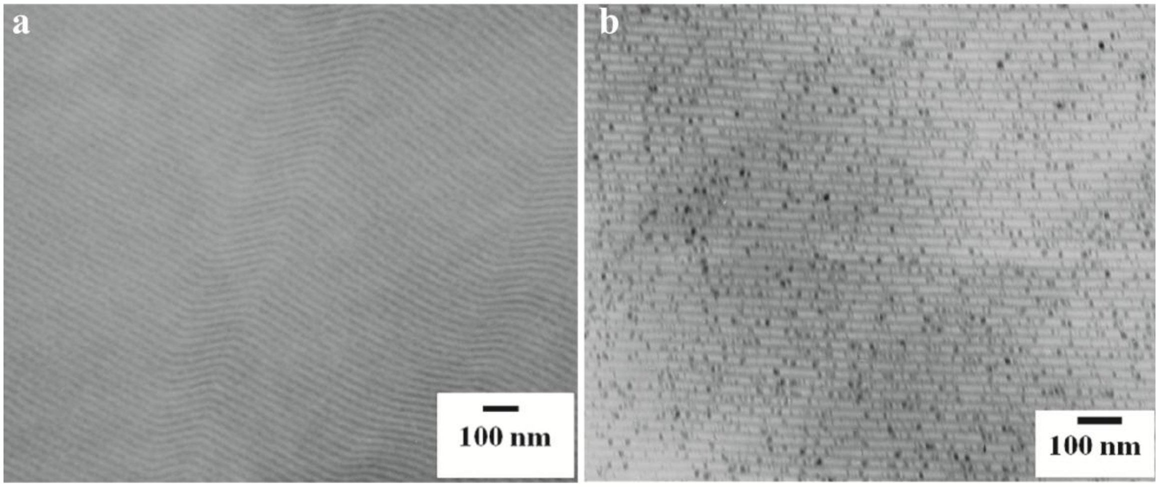

Figure 3.2 Representative TEM micrographs of **Poly4** depicting lamellar morphology a) before and b) after heat treatment. The formation of nanoparticles was observed in the thermally annealed sample consistent with that observed in the $\mathbf{ON_{Co}}$ homopolymer and **Poly1**.

The SAXS profiles of **Poly5**, both before and after thermal treatment, are shown in Figure 3.1(c). A well-defined but broad primary peak was observed in the SAXS profile of **Poly5** samples in both conditions. The small, broad reflection peaks in the SAXS profiles at $\sqrt{3}q^*$ and $2q^*$ would be consistent with a cylindrical morphology, which was confirmed by TEM (Figure 3.3) as inverted cylindrical morphology. Unlike other cobalt-containing polymers, no nanoparticle formation was observed in TEM images of **Poly5**. The whole matrix in the case of inverted cylindrical morphology is made up of the cobalt-containing block and due to the lack of sufficient atomic contrast; the observation of nanoparticles by TEM was not possible. However, since the formation of cobalt nanoparticles was observed in both the cobalt-containing homopolymer and other diblock copolymers with different morphologies (**Poly1** and **Poly4**), it is highly probable that the nanoparticles are formed even in the case of **Poly5**. Consistent with the other BCP morphologies, no remarkable distinction in morphology was observed in the TEM images of **Poly5** before and after thermal treatment. The diameter of the non-magnetic cylinders from the TEM images was ~ 21 – 22 nm and the d-spacing was approximately 25 nm. The d-spacing varied from 25-30 nm in the samples, corresponding to before and after heat treatment.

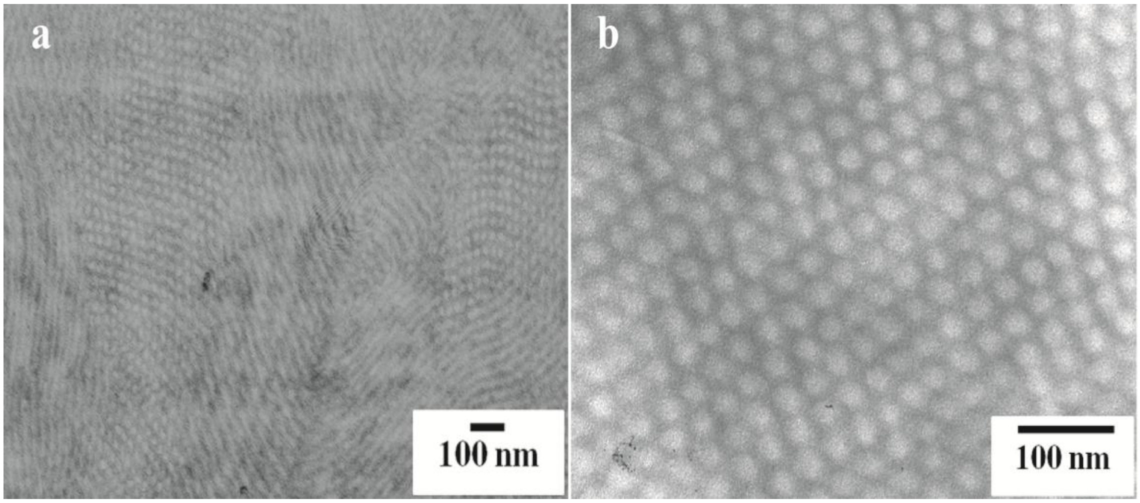

Figure 3.3 Representative TEM micrographs of **Poly5** with inverted cylindrical morphology a) before and b) after heat treatment. The formation of nanoparticles was not observed in the thermally annealed sample

Given the comparison of the three morphologies by TEM after heat treatment, it is clear that the lamellar morphology is much less efficient at confining the nanoparticles in one specific phase. In addition to smaller nanoparticles, the formation of many larger cobalt particles with dimensions of 10-15 nm was observed in the case of **Poly4**. While the majority of the smaller particles (3-5 nm) were confined to a single phase, the larger particles are distributed randomly in both the phases. In spite of the formation of larger nanoparticles, the clear contrast between the two phases corroborates the presence of substantial amount of cobalt in one phase.

3.3. Magnetic Characterization

3.3.1. Static Magnetic Properties

The magnetization at room temperature as a function of an applied field (*M-H*) was measured for all the thermally treated BCP materials by a SQUID magnetomer. Samples tested before the heat treatments were not ferromagnetic at room temperature. Representative magnetic hysteresis curves (M-H curves) for **Poly1**, **Poly4** and **Poly 5** are presented in Figure 3.4. All the nanostructured BCP materials showed magnetic hysteresis loops, irrespective of their morphologies, indicating that they were all RTFM materials. This confirmed the hypothesis that nanoconfinement or constraint within the BCP microdomains increased the interactions between SPM cobalt particles, formed within them, so that they collectively exhibited ferromagnetic behavior. The magnetization of BCPs in an applied field of 1T increased with the increase in the volume fraction of the cobalt-containing block, consistent with the amount of cobalt loading. Shearing of magnetic hysteresis curves for BCPs with cylindrical morphology (**Poly1**) were observed, most likely due to the shape anisotropy of cylinders.

Coercivity is the negative field required for magnetization reversal in ferromagnetic materials. In other words, it is an indicator of the strength of ferromagnetism and hence the higher values are preferred for magnetic applications. The coercive fields derived from the magnetic hysteresis curves are plotted as a function of volume fraction and shown in Figure 3.5. The BCPs with cylindrical morphology, having maximum confinement, had the highest coercivity. The coercivity values for the samples with inverted cylindrical morphology were second highest and least were for the BCPs with lamellar morphology. As described in the previous chapter, an ensemble of

SPM nanoparticles exhibiting collective behavior acts in a similar way to bulk ferromagnetic materials, with atomic moments being replaced by superspins of single-domain SPM particles.

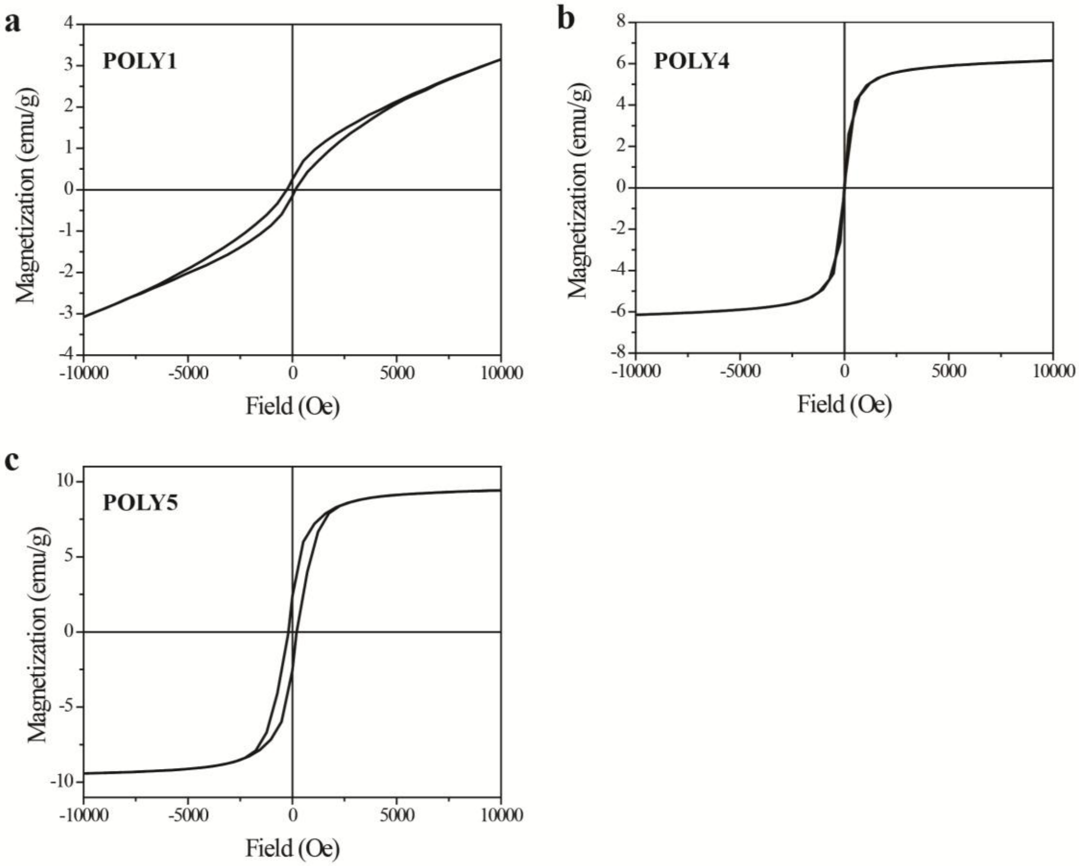

Figure 3.4. Representative magnetic hysteresis (M-H) curves as a function of applied field for BCPs with a) cylindrical (**Poly1)** b) lamellar (**Poly4)** and c) inverted cylindrical (**Poly5)**morphology at room temperature. The coercivity was derived from these M-H curves and represented as a function of volume fraction in Figure 3.5.

The BCPs with cylindrical morphology are analogous to an array of magnetic nanowires. Confining the SPM cobalt nanoparticles within the cylindrical microdomains increases the dipole-dipole interactions between them and they collectively act as a single elongated ferromagnetic particle or nanowire. Gross *et al.* has experimentally demonstrated this phenomenon by incorporating SPM cobalt nanoparticles within mesoporous silica which collectively exhibited ferromagnetic behavior under nanoconfinement. Similarly, ordered arrays of cobalt nanowires were grown within mesoporous aluminosilicate, which also exhibited RTFM behavior.[143]

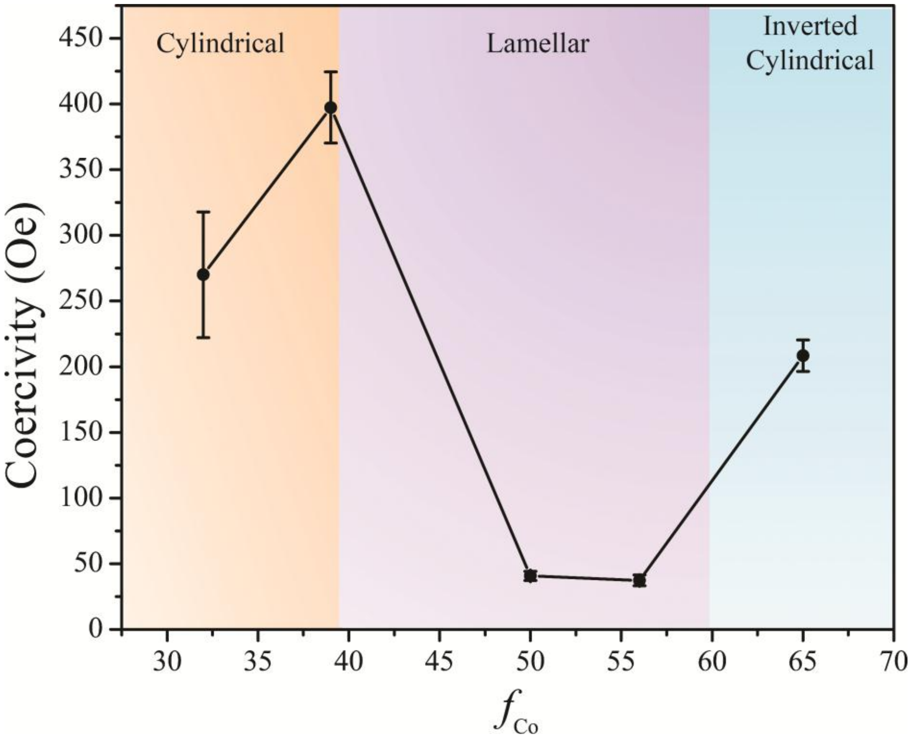

Figure 3.5. Effect of BCP morphology on the coercivity of cobalt-containing BCPs. Room temperature coercivities for **Poly1-Poly5** are plotted as a function of volume fraction ((f_{co}) of the cobalt-containing block**.** Coercivity is derived from the plots of magnetization (M) as a function of applied field (H) measured using a SQUID magnetometer.

Magnetic nanowires are one-dimensional systems and have a high aspect ratio, i.e. ratio of length to diameter. Due to shape anisotropy, the form of the nanowires favors the alignment of the magnetization along their lengths. The magnetization reversal mode of nanowire arrays with diameters in the range of tens of nanometers has been addressed in literature.[144, 145] Magnetization reversal in magnetic nanowires has been explained by both homogenous coherent and curling rotational mechanisms, depending on their diameters.[146] For diameters less than a critical radius, magnetization reversal occurs by coherent rotation, while for diameters above the critical radius, the curling mode is preferred. In either modes, a domain wall or magnetization reversal is nucleated within the nanowire, which then propagates along its axis. The nucleus formation is the energy limiting process in the magnetization reversal of nanowires. Nanowires are one-dimensional objects and hence the superspin or magnetic moment can align only in the direction parallel to the wire axis (up or down). The alignment of the magnetic moment in the direction perpendicular to the wire axis is energetically unfavorable. Thus, the magnetic moment has to rotate 180 degrees across the plane for reversal. The coercive field required for magnetization reversal is comparable to the coherent rotation of a single-domain spheroid, as described by the Stoner-Wolfarth model. The coherent rotation model is applicable under the assumption that there are no imperfections within the nanowires. However the nucleation of magnetization reversal usually occurs at local defects or imperfections. [147, 148] Thus, the experimental values for coercive fields of magnetic nanowires are less than the theoretically predicted values by the Stoner-Wolfarth model.

The lamellar morphology of **Poly3** and **Poly4** are analogous to 2-D magnetic thin films. The magnetic thin films are geometrically constrained in one dimension and hence are magnetized in the plane of the sample. The domain walls in bulk ferromagnetic materials, referred to as the Bloch walls, normal to the plane of the material, which causes large demagnetization energy in thin films. In contrast, Néel walls are formed within magnetic thin films in which moments rotate within the plane of the specimen.[43] With this difference in the freedom of rotation available for the magnetic moment, the magnetization reversal happens by nucleation and propagation of the domain wall in the plane of the sample. Hence the nucleation and propagation of domain walls is easier in thin films compared to nanowires.[149] For example, Thurn-Albrecht *et al.* developed high density cobalt nanowire arrays by electrodeposition within PS-*b*-PMMA nanopores that exhibited very high coercivity (800 Oe) compared to that of a cobalt thin film (10 Oe).[110] Thus, the coercivity of BCPs with lamellar morphology is expected to be less than those with cylindrical morphology, which is consistent with our observed results.

The BCPs with inverted cylindrical morphology have a 3D matrix of the cobalt-containing block constrained by non-magnetic cylinders. Due to the three dimensional freedom, magnetization reversal of superspin is expected to be similar to that observed in homopolymer, thus showing lower coercivity or SPM behavior. However, in the case of inverted cylindrical morphology, the matrix is constrained more than the homopolymer due to the presence of non-magnetic cylinders. In fact, there is a preferred orientation of magnetization along the direction parallel to the axis of non-magnetic cylinders, imparting anisotropy. Thus, the inverted cylinder is analogous to a bulk ferromagnetic material with holes drilled in it. Surprisingly, magnetization studies of such systems have not yet been reported in the literature. However, several reports studying the magnetization of antidot arrays, which are obtained by creating arrays of pores within continuous magnetic thin films, have been reported. The anti-dots are artificially engineered defects that act as pinning centers inhibiting the movement of domain walls during magnetization reversal.[150, 151] Detailed magnetization reversal mechanisms in anti-dot arrays by nucleation, propagation and pinning has been demonstrated by micromagnetic simulations.[150-152] However, the magnetization reversal demonstrated in anti-dot arrays is more applicable to in-plane magnetic fields, as they are 2-D objects. On the contrary, the inverted cylindrical morphology in BCPs behaves as anti-cylinders and has more freedom for magnetization reversal. The orientation of magnetic moment or superspin in the direction normal to the sample is possible. Due to shape anisotropy considerations, there is a preference for domain wall propagation in the direction perpendicular to the surface (or along the axis of cylinders), as there are no hindrances for the domain wall motion. In spite of this major difference from antidot arrays in thin films, the pinning of domain walls can still occur in the case of inverted cylindrical morphology. Thus, the domain walls are more constrained in the inverted cylindrical morphology when compared to those in the lamellar morphology (or 2D thin films) but less constrained than the domain walls in the cylindrical morphology due to interconnectivity or percolation of the matrix. This analysis is consistent with the coercivity values for inverted cylindrical morphology being less than cylindrical morphology but more than for the lamellar morphology.

To further understand the effect of block copolymer morphology on the magnetic behavior of cobalt-containing BCPs, the ZFC (Zero-field cooled) and FC (Field cooled magnetic characterizations were carried out and are presented in Figure 3.6. The ZFC curves of all the diblock copolymers with different morphologies increased with increase in the temperature and did not exhibit any peak corresponding to blocking temperature below room temperature. This suggests a broad distribution of blocking temperatures in all BCPs. Further, the ZFC and FC curves for **Poly1** and **Poly5**, with cylindrical and inverted cylindrical morphologies respectively, did not combine below 325 K, indicating that their T_B are beyond that temperature. However, the ZFC and FC curves for **Poly4** with lamellar morphology combined at 312 K, indicating that its blocking temperature is lower than those observed for samples with cylindrical (**Poly1**) and inverted cylindrical morphologies (**Poly5**) but still above room temperature. These results from ZFC and FC magnetization curves are consistent with the RTFM behavior for all the BCPs, irrespective of their morphology. Further, the profiles of FC curves can also provide information about the coupling interactions between cobalt nanoparticles formed upon thermal treatment within the polymer matrix.[129, 134]

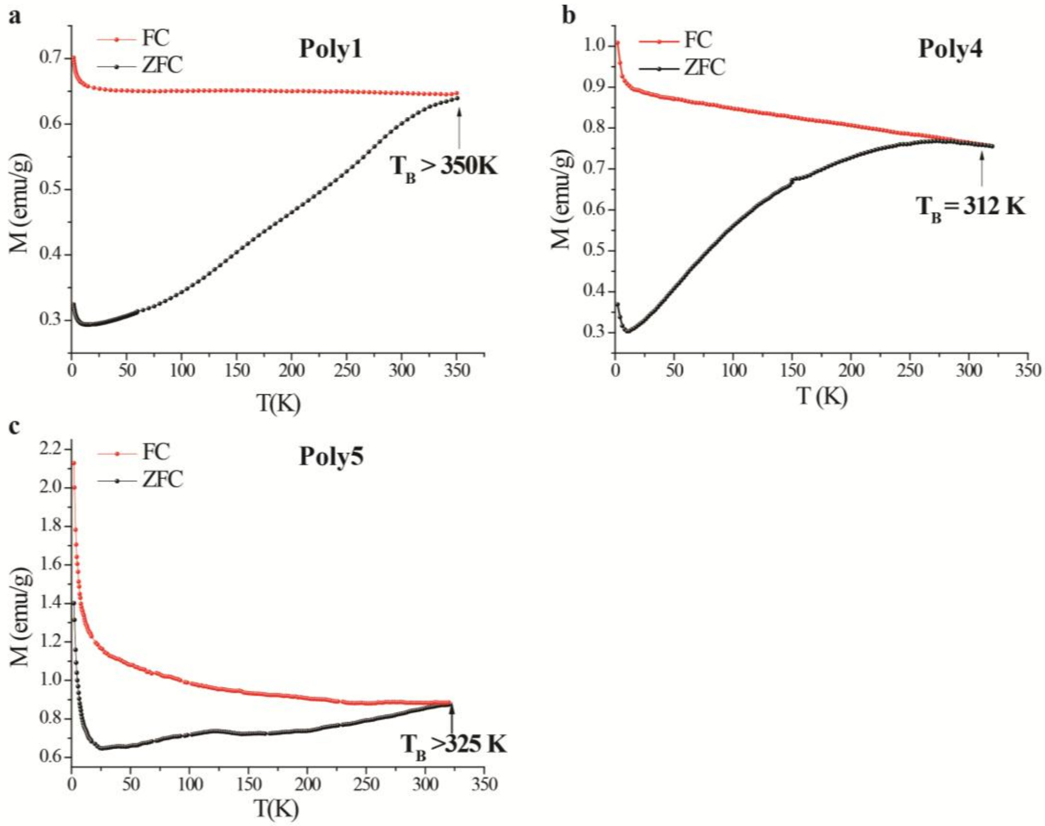

Figure 3.6. Representative zero-field cooled (ZFC) and field cooled (FC) magnetization curves of cobalt-containing BCPs with a) cylindrical (**Poly1**) b) lamellar (**Poly4**) and c) inverted cylindrical morphology (**Poly5**) as function of temperature (**B**) with a field of 100 Oe.

The FC curve for cylindrical morphology increased very gradually as temperature decreased so that its slope is close to zero, indicating increased dipolar interactions. An increase in the dipolar interactions among the magnetic nanoparticles is known to increase the energy barrier for magnetization reversal and hence increases their blocking temperature.[49] The slopes of the FC curves for the lamellar morphology (4.66x10^{-4}) and inverted cylindrical morphology (3.1x10^{-4}) in the temperature range of 150 K to 300 K were higher than that of the cylindrical morphology (2x10^{-6}) indicating les interaction between the particles. Below 150 K, all BCPS exhibit paramagnetic-like behavior. This is consistent with the highest coercivity observed for the BCPs with cylindrical morphology. Even though the difference in the values of slopes for inverted cylindrical morphology and lamellar morphology is small, the slope of FC curve for lamellar morphology is slightly higher and is also consistent with coercivity.

3.3.2. Dynamic Magnetic Properties

In order to evaluate the effect of BCP morphology on the magnetic relaxation time and the actual energy barrier, the temperature dependence of the AC susceptibility was measured in the frequency range of 30-10^4 Hz. Shown in the Figure 3.7 are the representative curves of the In-phase (χ') and out-of-phase (χ'') components of AC-susceptibility as a function of temperature at different frequencies for BCPs with cylindrical (**Poly1**), lamellar (**Poly4**) and inverted cylindrical morphology (**Poly5**).

For all the BCPs, irrespective of their morphology, χ' increased with an increase in temperature and no peak maximum was observed until 325 K. The temperature at which a peak maximum is observed in AC susceptibility curves corresponds to T_B. These results are consistent with the ZFC and FC magnetic characterizations, indicating that the blocking temperature is beyond 325 K for all the BCPs, which is also consistent with magnetic hysteresis curves at room temperature. Since the peak maximum was not observed in both χ’(T) and χ’’(T), it was not possible to determine the relaxation time and energy barriers for BCPs with different morphologies. However, the difference in the frequency dependency of AC susceptibility is evident for different BCP morphologies. The lamellar morphology **Poly4** has a maximum reduction in the values of χ’ at 320 K (28% reduction) from lowest frequency to highest frequency (30 Hz to 10,000 Hz). **Poly1** had the second highest reduction in the values of χ’(T) (~22%). However, χ’(T) for the inverted cylindrical morphology did not exhibit frequency dependence.

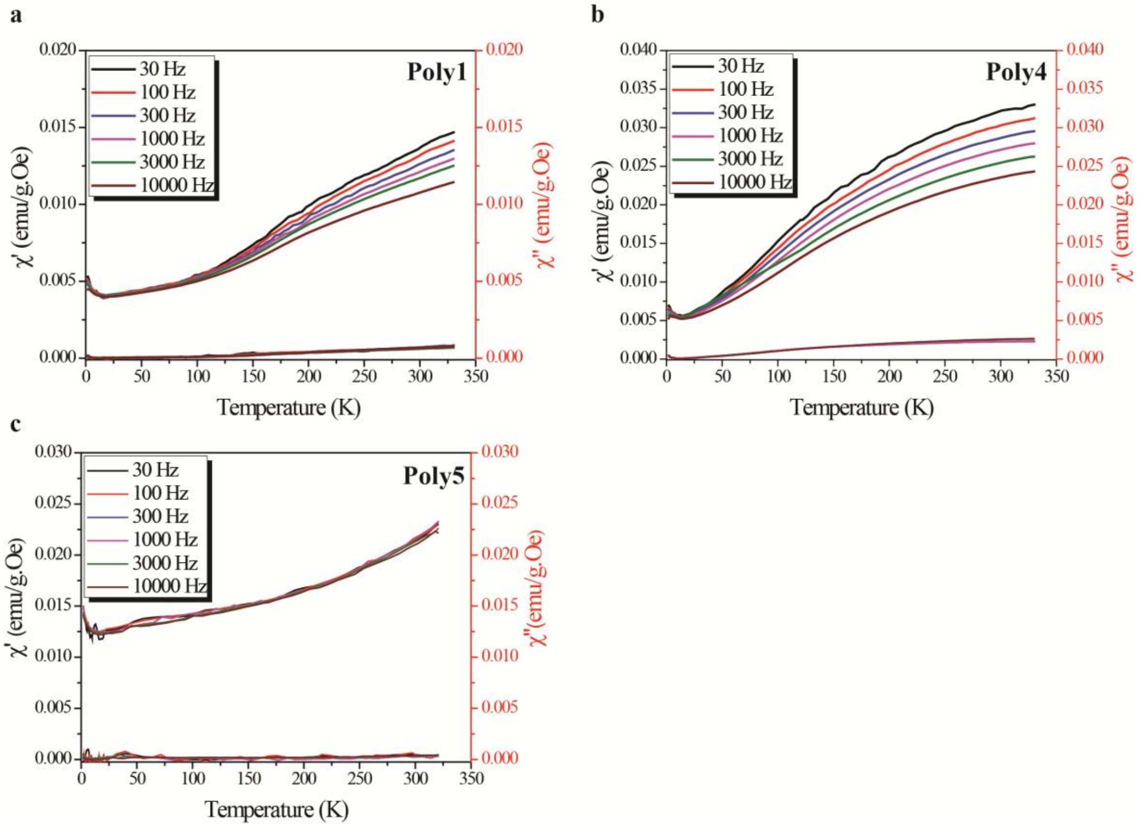

Figure 3.7. Temperature dependence of the in- and out-of-phase components, χ’ and χ”, of AC susceptibility measured at various frequencies (30 – 10^4 Hz) for cobalt-containing BCPs with a) cylindrical (**Poly1**), b) lamellar (**Poly4**)and c) inverted cylindrical morphology (**Poly5**) in an AC field of 5 Oe.

Usually, the frequency dependence of χ'(T) increases with temperature and is observed to be maximum near T_B. As temperature is decreased from T_B, χ'(T) decreases as well. According to this analysis, the T_B seems to be highest for the inverted cylindrical morphology, second highest for the cylindrical morphology and lowest for the lamellar morphology. The lamellar morphology having the lowest T_B is consistent with ZFC and FC measurements. However, the T_B obtained from AC susceptibility measurements contradicts the T_B obtained from the ZFC and FC measurements for the inverted cylindrical and cylindrical morphologies. The reason for these contrasting results is not well understood and the conclusions are speculative. The T_B is a function of applied field and shifts to lower temperatures by increasing the applied field strength. The applied fields for ZFC-FC and AC susceptibility measurements are 100 Oe and 5 Oe respectively. The T_B is also a function of the particle volume and hence it increases with an increase in the particle size. BCPs with inverted cylindrical morphology are composed of a 3D matrix of the cobalt containing block constrained by non-magnetic cylinders. Due to the percolation effect, the size of grains or domains in BCPs with inverted cylindrical morphology is expected to be larger than in the cylindrical morphology. An increased T_B for the inverted cylindrical morphology from AC susceptibility measurements is consistent with this analysis. Further, the arrangement of SPM cobalt particles within cylindrical morphology and inverted cylindrical morphology may also be playing a role in determining the T_B. Dormann *et al.* examined γ-Fe_2O_3 (7 nm) particles and entangled chain agglomerates by AC susceptibility.[137] The particle samples showed lower peak temperatures for χ', indicate lower stability of particles to thermal fluctuations than the agglomerated samples, which have more neighbors and thus higher magnetostatic dipolar interactions. Applying the same analysis, the stability of particles within inverted cylindrical morphology is expected to be higher than in the cylindrical morphology and thus higher T_B. Further, the pinning of domain walls by the non-magnetic matrix may be another factor contributing to this discrepancy. However, it is well known that the blocking temperature is increased by increasing the dipolar interactions between particles and shape anisotropy. Therefore, the cylindrical morphology having more confinement and shape anisotropy than the inverted cylindrical morphology is expected to have higher coercivities. These systems with multi-components are complex and require additional investigation by SANS and MÖssabauer spectroscopy are required to understand the ferromagnetic correlations between the particles. Further, the temperature dependence of AC susceptibility as a function of frequencies can be obtained at increasing AC fields, which would provide further information regarding the dynamics of magnetization reversal in these BCPs.

3.4. Summary

To summarize, all BCPs irrespective of their morphologies exhibited RTFM behavior. The SPM cobalt nanoparticles, formed within the BCPs upon thermal treatment, exhibited a collective ferromagnetic behavior due to confinement within the microdomains of BCP. The BCPs with cylindrical morphology, having maximum confinement, exhibited the highest coercivity. The coercivity values for samples with inverted cylindrical morphology were second highest, and least for the BCPs with lamellar morphology. The magnetization reversal within cylindrical domains of BCPs is analogous to that in magnetic nanowires. Considering the diameter of the cylinders formed within the BCPs (~ 20 nm), the magnetization reversal by coherent rotation mode is preferred. In this mode, magnetization reversal is nucleated in small region of cylinder and propagates along the cylindrical axis. The magnetization reversal in lamellar morphology is analogous to that in magnetic thin films, which again happens by nucleation and propagation of domain wall. However, due to two dimensional freedom, the moments are able to rotate in-plane and hence, the magnetization reversal process is much easier in lamellar morphology than that in the cylindrical morphology. Finally, in inverted cylindrical morphology, the magnetization reversal again occurs by nucleation and propagation of the domain walls but in this case the domain walls' motion is hindered by pinning from non-magnetic cylinders. The presence of non-magnetic cylinders also imparts shape anisotropy to the magnetic matrix, with preference for propagation along the axis of cylinders.

No peak maximum was observed in the ZFC and χ'(T) curves at different frequencies for all BCPs, which is consistent with their RTFM behavior. Hence, determining T_B, relaxation time (τ_0) and the energy barrier was not possible to provide further insight into the magnetization reversal phenomenon in these BCPs.

CHAPTER 4

TUNING THE DIPOLAR INTERACTIONS WITHIN CYLINDRICAL MICRODOMAINS OF BLOCK COPOLYMER

4.1. Introduction

In the earlier two chapters, RTFM behavior in cobalt-containing BCPs, irrespective of their morphology, has been demonstrated. The SPM cobalt particles confined within the microdomains of the BCPs exhibited collective ferromagnetic behavior due to increased dipolar interactions between them. Thus, the dipolar interactions between the SPM nanoparticles play a significant role in determining the magnetic behavior of these cobalt-containing polymers. Previously it has been shown that the dipolar interactions between magnetic elements usually increase with increasing their concentration or decreasing the distance between them.[129, 153, 154] This increase in dipolar interactions typically results in higher coercivity. It is thus reasonable to hypothesize that the coercivity of our BCPs could be tuned by varying the dipolar interactions between the SPM cobalt particles within the nanostructured domains. To investigate this hypothesis two different approaches are presented in this chapter. In first approach, the dipolar interactions between SPM cobalt particles are reduced by reducing the cobalt density within cylindrical domains. The BCP with cylindrical morphology was chosen for these studies, as it had exhibited highest coercivity among the BCPs with different morphologies. In second approach, the diameter of the cylindrical domains was increased by increasing the molecular weight of the BCPs. It was hypothesized that at given cobalt density, the dipolar interactions between SPM cobalt particles is expected to reduce by reducing the nanoconfiment or increasing the size or diameter of cylindrical domains.

4.2. Effect of Cobalt Density

4.2.1. Characterization of Block Copolymers

It was proposed that reducing the cobalt density within nanostructured domains would result in the reduction of dipolar interactions between the cobalt particles. However, it is necessary that the same BCP morphology is maintained while reducing the cobalt density within the domains as the morphology also influences the magnetic properties. This can be achieved by employing block-random copolymers, with the general chemical structure "A-*b*-(B-*r*-C)", where the first block is a homopolymer of the monomer A and the second block is random copolymers of monomers B and C. For this study, a series of metal-containing block-random copolymers composed of alkyl-functionalized homo block (C16) and a random block of cobalt complex- (Co) and ferrocene-functionalized (Fe) units with chemical structure as shown in the Figure 4.1 were synthesized via ROMP. The block ratio of homo to the metal-containing random blocks was kept 70:30 such that the resulting bulk morphology of the BCPs was cylindrical. Taking the advantage of block-random architecture, the influence of dipolar interactions on the magnetic properties of these nanostructured BCPs was studied by varying the molar ratio of the Co units to the Fe units, while maintaining the cylindrical phase-separated morphology. The ferrocene-based monomer was chosen as it is inert to thermal annealing conditions (200 ºC) but at the same time contributes to the microphase separation of the BCP. The synthesis of these BCPs has been reported in recent publication.[155] Increasing the ratio of ferrocene monomer to cobalt monomer effectively reduced the cobalt density within the cylindrical domains. The ratio of cobalt and ferrocene was systematically varied from 0 to 100%. After synthesis, the molecular weights and diblock architecture of these BCPs were confirmed by GPC and NMR. The sample preparation and characterization of these BCPs were carried out in similar ways as described in the previous chapters and the results were tabulated in Table 4.1. The formation of cylindrical morphology and the dimensions of the cylinders in the BCPs were verified by SAXS and TEM. All the BCPs had the similar bulk periodicities with d-spacing values ranging from 42 to 54 nm and the cylindrical diameters were found to be around 20 nm. Thus a fair and logical conclusion could be derived from the magnetic characterization.

Table 4.1 Details of cobalt-ferrocene functionalized random block copolymers.

Polymer	**Mn**[a]	**PDI**[a]	**Block Ratio (n/m)**[b]	**Co : Fe (x : y) (Molar ratio)**[c]	***d*-spacing (nm)**[d]	**d_{cyl} (nm)**[e]
C1	75K	1.10	70:30	100:0	48	20
C2	82k	1.09	76:24	76:24	47	20
C3	89k	1.08	77:23	66:34	45	18
C4	85k	1.08	77:23	54:46	45	21
C5	83k	1.07	78:22	38:62	42	19
C6	90k	1.06	78:22	32:68	47	20
C7	94k	1.05	78:22	23:77	49	21
C8	100k	1.07	78:22	13:87	54	19

[a] Determined by GPC in THF using RI detector, relative to polystyrene standards [b] Block ratio of the Co-r-Fe block (f_{Co+Fe}) calculated based on density data which were obtained by the gradient density column method [c] Co unit percentage in the Co-r-Fe block calculated from ^{1}H NMR integration [d] Bulk periodicity: $d = \frac{2\pi}{q^*}$, where q^* is the primary scattering peak as determined by SAXS [e] Diameter of the cylindrical domains (d_{cyl}) determined by TEM images.

4.2.2. Static Magnetic Properties

The magnetization as a function of applied field at room temperature was obtained for this series of BCPs and the coercivity as derived from the hysteresis curves is plotted as a function of cobalt monomer ratio in Figure 4.1. The coercivity of the BCPs decreased continuously as the ratio of cobalt monomer i.e. as the cobalt density was reduced and eventually underwent a transition from ferromagnetic to SPM behavior at a threshold of 30% molar ratio of cobalt monomer. The BCP containing only ferrocene (0% cobalt-functionalized monomer) exhibited diamagnetic behavior, confirming that it is inert to thermal treatment at 200 ºC and thus ferrocene will not contribute to the magnetic properties. These results can be compared to the studies from Gross *et al.* in which SPM cobalt nanoparticles were incorporated within mesoporous silica.[129] The effect of varying the concentration of cobalt particles within nanopores on their magnetic behavior was investigated. A reduction in coercivity and blocking temperature from 250 K to 170 K was observed when the concentration of cobalt was reduced from 22% to 0.3% by mass. Reduction in the coercivity was attributed to the decrease in dipolar interactions. Further, the decrease in T_B was due to the formation of smaller chains of SPM particles, as the concentration of cobalt particles was reduced within the nanopores. Similarly, by increasing the interaction strength between the particles in granular metal-insulator multilayer systems $[Co_{80}Fe_{20}/Al_2O_3]_n$, a transition from non-collective SPM behavior to collective SSG and SFM behavior was demonstrated.[61] The $Co_{80}Fe_{20}$ particles were grown on sapphire glass interface and nominal thickness *t* was varied to control the dipolar interactions.

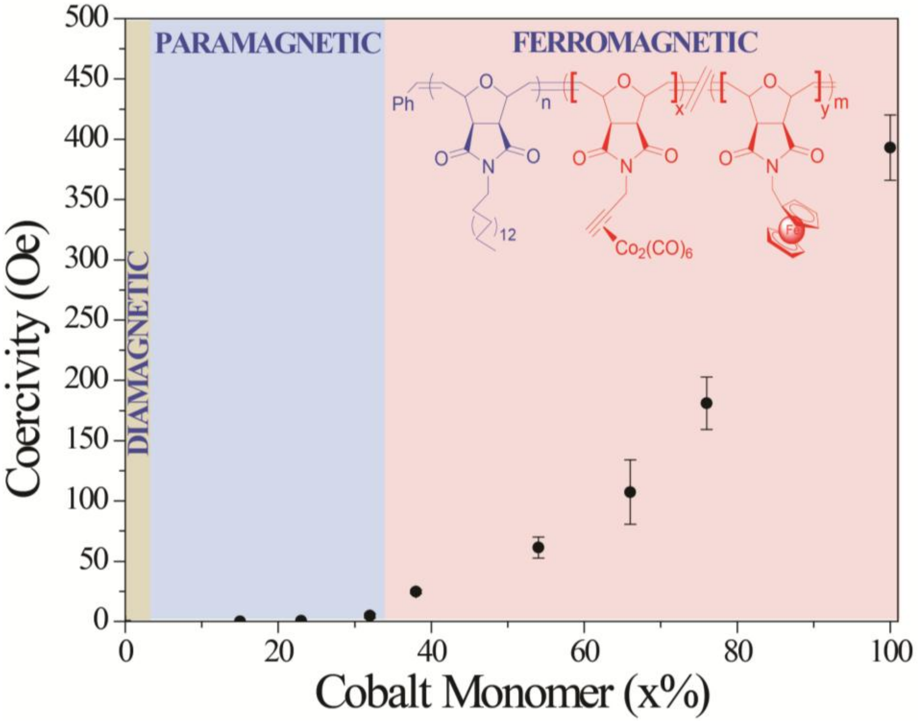

Figure 4.1 Coercivity as function of cobalt monomer content within cobalt-ferrocene functionalized BCPs.

The effect of cobalt density within the cylindrical domains on the dipolar interactions between cobalt particles was further investigated by ZFC and FC measurements. The ZFC and FC curves for 3 different BCPs with ratios of cobalt monomer equal to 100% (**C1**), 65% (**C3**), and 13% (**C8**) are shown in Figure 4.2. These samples were chosen for ZFC and FC measurements to represent different concentration regimes: **C1** - ferromagnetic regime (right extreme); **C8** - SPM regime (left extreme); and **C3** - intermediate or near transition between SPM and ferromagnetic behavior.

The ZFC curve for **C1** increased continuously with temperature and did not reach a maximum before 350 K, indicating that the T_B for this BCP was much higher than 350 K. The ZFC curve for **C3** increased steeply until 210 K and increased gradually to reach a maximum value at around 280 K, then started to decrease to meet the FC curve at 312

K. The ZFC curve for **C8** reached a maximum at 70 K and then gradually decreased to meet the FC curve at 195 K, which is consistent with its SPM behavior.

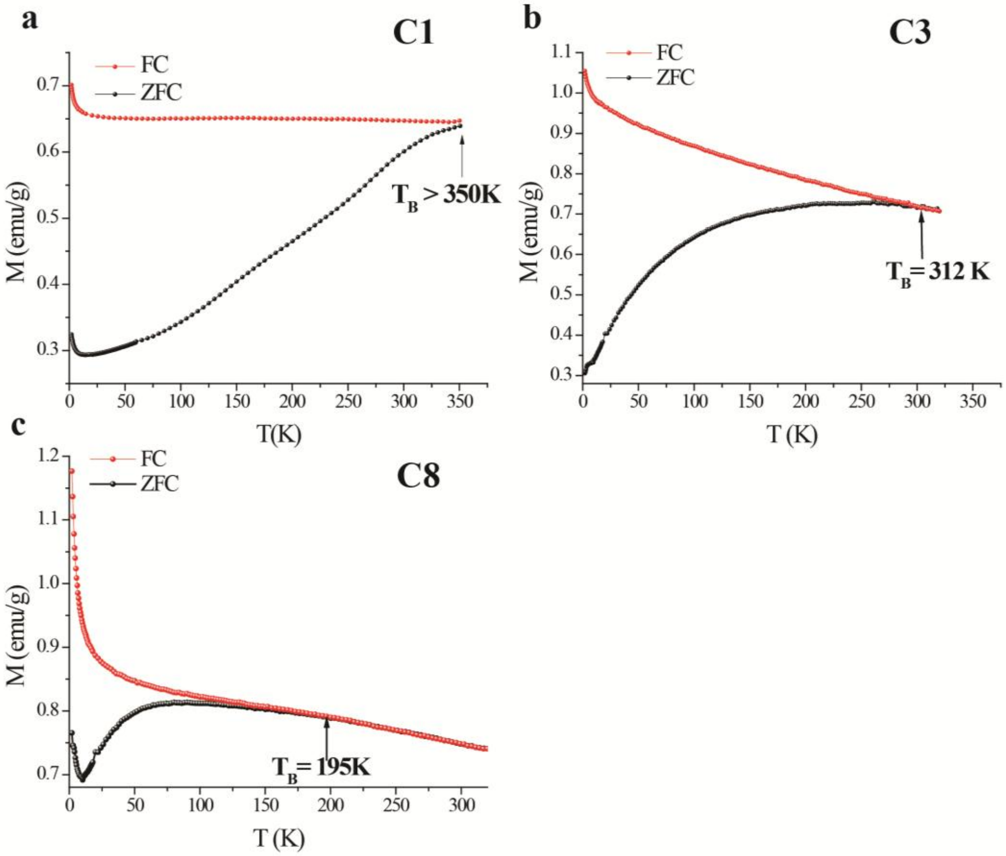

Figure 4.2 Zero-field cooled (ZFC) and field cooled (FC) curves of cobalt-ferrocene containing BCPs with cobalt monomer ratio equal to a) 100 % (**C1**) b) 65 % (**C3**) and c) 13% **(C8)** in a probe field of 100 Oe.

The peak maximum within the ZFC curves corresponds to mean particle size, and the temperature of bifurcation between ZFC and FC curves corresponds to the largest particle size. These results from ZFC and FC measurements for BCPs with different cobalt monomer concentrations indicate that both the average and largest particle sizes formed within the cylindrical domains for **C3** and **C8** are smaller than those observed in **C1**. These results are consistent with the coercivity values. Furthermore, the relative particle sizes derived from the ZFC and FC curves essentially denote the magnetic grain or domain sizes. The reduction in the magnetic grain or domain sizes with dilution of cobalt density within the cylindrical domains suggests a reduction in dipolar interactions, which is consistent with the observation that smaller chains were formed within nanopores as the concentration of cobalt particles was reduced as reported by Gross *et al.*[129] A large increase in the FC curves was observed for **C3** (slope = $7.7\text{x}10^{-4}$) and **C8** (slope = $4.6\text{x}10^{-4}$) in comparison to the very gradual or small increase for **C1** (slope = $2\text{x}10^{-6}$), as measured in the temperature range of 150 – 300 K. This further strengthens the argument that the interactions between SPM cobalt particles are reduced with decreased cobalt monomer concentration. A decrease in the T_B of BCPs with the reduction of cobalt monomer concentration is again consistent with the results reported from Gross *et al* [129]

4.2.3. Dynamic Magnetic Properties

To study the effect of cobalt density within cylindrical domains on the relaxation time and energy barrier, AC susceptibility curves as a function of temperature at different frequencies for BCPs **C1**, **C3** and **C8** were determined and are shown in Figure 4.3. The values of $\chi''(T)$ for all BCPs were very low and hence no meaningful interpretation was possible from them. The $\chi'(T)$ of all the BCPs increased with temperature and no peak maximum was observed until 325 K. The lack of peaks in the $\chi'(T)$ curves prevented the determination of the intrinsic relaxation times and energy barriers by an Arrhenius plot. However, it is evident that $\chi'(T)$ for **C1** increased continuously with temperature, whereas a saturation temperature (T_{sat}) in $\chi'(T)$ was observed for **C3** and **C8**. Additionally, the saturation temperature for **C8** (T_{sat} ~ 175 K) started at lower temperature than the **C3** (T_{sat} > 250 K). The anisotropy constant for iron (K_1 = 4.8 x 10^5 ergs/cm^3) is ten-fold less than cobalt's (K_1 = 45 x 10^5 ergs/cm^3) and hence might be responsible for this saturation behavior.[43] A lower anisotropy constant results in a lower energy barrier ($E_B = KV$), hence iron is expected to saturate at lower temperatures than cobalt. It has been reported that with increasing dipolar interactions, the peak in the χ' curve shifts to higher temperature. Although, no peak was observed for these BCPs, the T_{sat} followed the similar trend. With decreasing the cobalt density within the cylindrical domains, fewer cobalt particles are formed and hence the dipolar interactions are reduced between them. The formation of ~5 nm cobalt nanoparticles in the 100% Co sample (C16-b-Co copolymer) was confirmed in previous chapters. Therefore it seems safe to assume similar sized particles are formed by these new BCPs. Even if the particle size is smaller than 5 nm, they are still below the critical size for cobalt nanoparticles (10−12 nm). Therefore, the only way the samples reported here can be RTFMs is by having dipolar interactions among the particles assisted by the overall cylindrical shape anisotropy.[45] At the same time, it is unlikely that nanoparticles are not formed at all as the cobalt density is decreased based on the ZFC-FC and AC measurements. For example, if no particles were present, there would be no dipolar interactions in the system, and the T_B would be absent. However, even for the 13% Co sample which contains the least number of cobalt-containing monomers, T_B is above 100 K, and the saturation temperature in the AC susceptibility measurement is above 200 K, indicating that there are dipolar interactions present in this system. These BCPs with multi-components are complex systems and it is non-trivial to derive any conclusive interpretations on their dynamic magnetic behavior without further characterizations.

Further characterizations to determine ferromagnetic correlations between cobalt atoms using SANS and MÖssbauer spectroscopy may provide better understanding on the magnetic behavior of these BCPs.

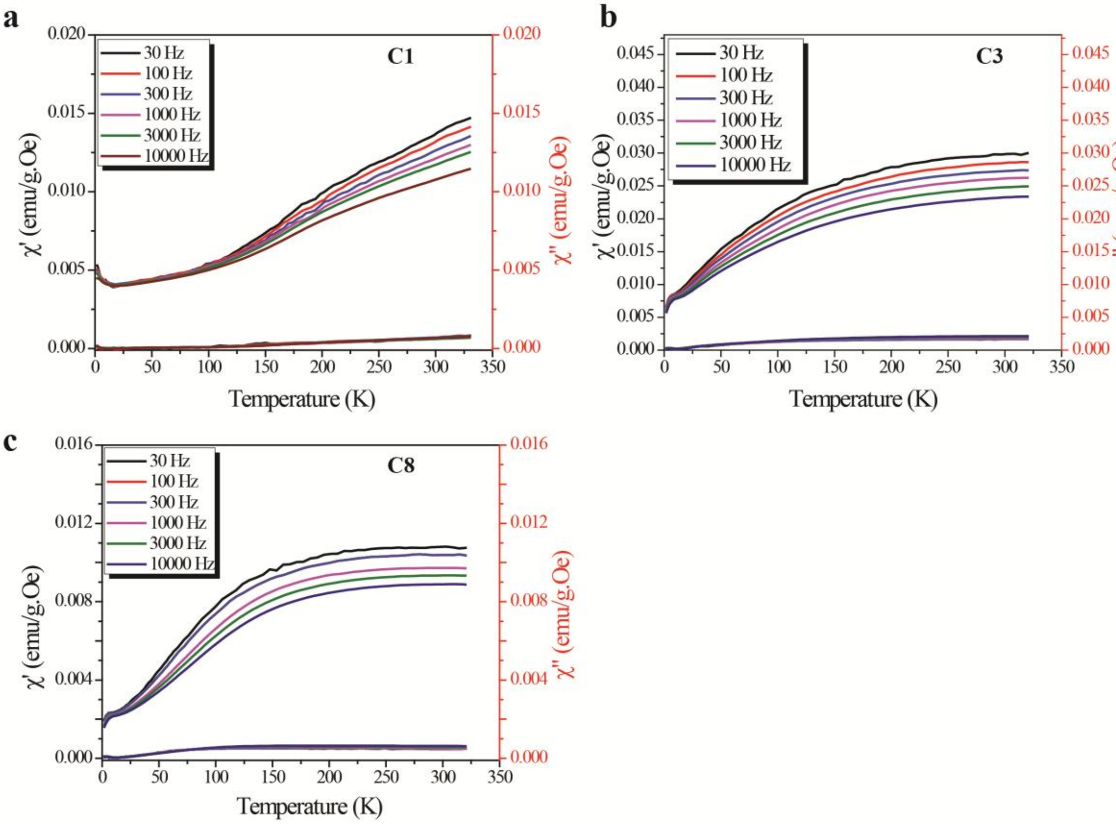

Figure 4.3. Temperature dependence of the in-phase and out-of-phase components, χ' and χ", of AC susceptibility measured at various frequencies (30 – 10^4 Hz) for cobalt-ferrocene functionalized BCPs at different cobalt monomer concentrations. a) **C1** (100% Co), b) **C3** (65% Co) and c) **C8** (13% Co) at an AC field of 5 Oe.

4.3. Effect of Diameter of Cylindrical Domains

So far, it has been demonstrated that the strength of dipolar interactions between the SPM cobalt nanoparticles is determined by the nanoconfinement of the cylindrical microdomains within the BCPs. Another approach to tune these dipolar interactions within these cylindrical microdomains is by changing their diameter. For a given cobalt density, the dipolar interactions are expected to decrease with an increase in the diameter of the cylinders. It is well known that the dimensions of the BCP domains can be varied by varying the overall molecular weight of BCP. A series of five cobalt-containing BCPs with their overall molecular weights ranging from 50 kDa to 300kDa were synthesized, while keeping their block ratios constant i.e. the molar ratios of the C16 units to the Co units were kept 70:30, to yield cylindrical morphology as described in Table 4.2. The synthesis and characterization of all these polymers are published elsewhere.[156]

Table 4.2 The details of diblock copolymers with different molecular weights to vary the diameter of cylindrical domains.

Polymers	M_n (kDa)[a]	PDI	Morphology	d_{cyl} (nm)[b]	d-spacing (nm)[c]
M1	52	1.15	Cylindrical	16	32
M2	100	1.12	Cylindrical	20	38
M3	200	1.10	Cylindrical	22	43
M4	262	1.15	Cylindrical	24	48
M5	296	1.08	Cylindrical	25	52

[a] Determined by GPC in THF using RI detector, relative to polystyrene standards

[b] The diameter of the cylindrical domains (d_{cyl}) was determined from the TEM images

[c] Bulk periodicity: $d = \frac{2\pi}{q^*}$, where q^* is the primary scattering peak as determined by SAXS

The M_w and block ratios of these BCPs were characterized by GPC and NMR. Thermally annealed films of these BCPs were developed according to the procedure as described in previous chapters and were characterized by SAXS and TEM, in order to determine their morphology and dimensions of micro domains. After solvent annealing, the SAXS profiles of the BCPs all showed peaks corresponding to q*, $\sqrt{3q^*}$, $\sqrt{7q^*}$, indicating cylindrical morphology. The formation of well-defined, phase-separated cylindrical morphology was further confirmed by bright field TEM image of the unstained solvent as well as thermally annealed sample. As the overall molecular weight of the BCPs increased from 52 kDa to 296 kDa, the diameter of the cylindrical domains obtained from TEM studies increased from 16 to 25 nm. Similarly, the d-spacing, determined by SAXS, increased from 32 nm to 52 nm.

The magnetic characterization of the thermally treated BCPs was carried out at room temperature in SQUID magnetometer. Magnetic hysteresis loops were observed for all the BCPs with different molecular weights, indicating their RTFM behavior, consistent with our hypothesis. The coercivities for various BCPs were determined from their respective magnetic hysteresis curves and are plotted as function of diameter and shown in Figure 4.4. The average coercivity values appeared to initially increase with diameter, reach maximum value and then decrease. However, the difference in the coercivity values for these BCPs with different cylindrical diameters was not statistically significant, as their error bars overlapped with each other. Previously, it was shown for the cobalt nanoparticles that with increase in size of the nanoparticles, the superparmagnetic to ferromagnetic transition i.e. blocking temperatures above 300 K, occurred around at 10-12 nm.[45] Since the smallest diameter of cylindrical domains obtained in these BCPs was ~16 nm, the observed RTFM behavior was expected. Further, the range of cylindrical diameters investigated i.e. 16 nm to 25 nm, was probably not sensitive enough to show any significant difference in their coercivities. However, the trend observed here is similar to that observed for magnetic nanowires. For example, the coercivity of Ni nanowires increased from 480 Oe at 8 nm diameter to 950 Oe near 18 nm and then decreasing with further increasing wire diameter.[157] The coercive field is directly proportional to the volume of the magnetic nanostructure and hence is expected to the increase as diameter of the nanowires increases. Nevertheless, for diameters larger than a critical diameter, due to the transition from a single-domain to a multi-domain system, coercivity decreases with an increase in diameter. Since the values of coercivities for this series of BCPs were statistically similar, no clear correlation between the diameter of cylinders and dipolar interactions between the SPM cobalt particles or macroscopic magnetic properties was derived from these studies.

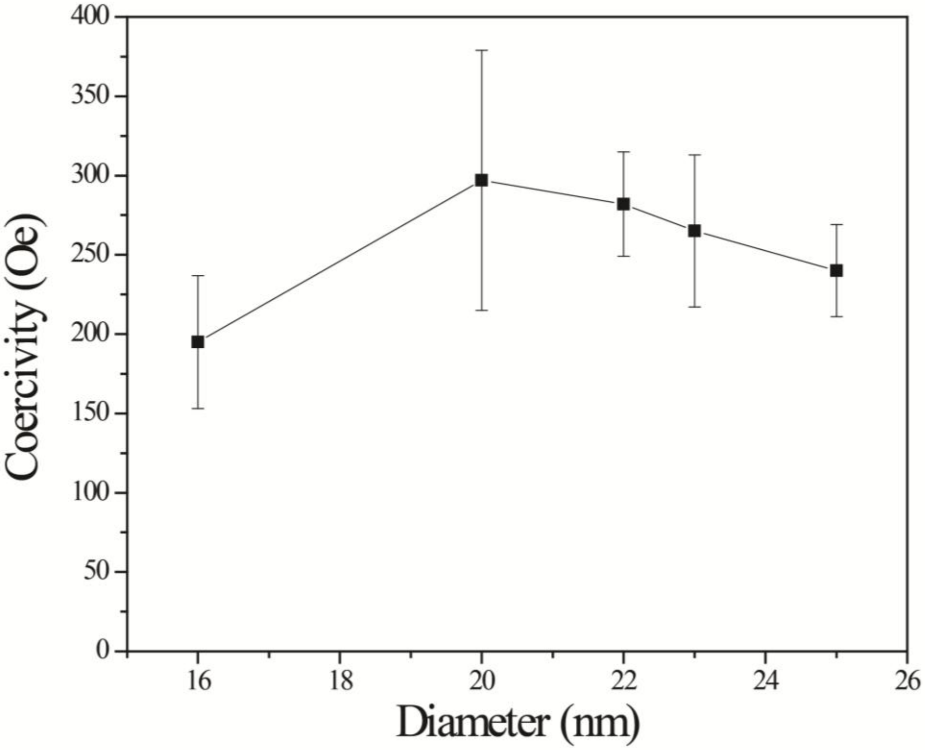

Figure 4.4 The effect of the diameter of the cylindrical domains on BCP coercivity.

The BCP with molecular weight of 25 kDa could not phase separate and hence obtaining cylindrical diameters less than 15 nm would not be possible. Meanwhile, it was synthetically challenging task to obtain BCPs with molecular weights greater than 300 kDa. The first block could not be completely initiated by the second monomer, limiting the study of cylindrical diameters beyond 25 nm. One other limitation of this study is that with increase in the M_w of a BCP, the d-spacing between the cylindrical domains also increases and hence a direct comparison of the macroscopic magnetic properties of BCPs with different M_w is not appropriate. Alternatively, it is possible to increase the dimensions of cylindrical domains by blending BCPs with the cobalt metal-containing homopolymer $\mathbf{ON_{Co}}$ and need to be investigated in future studies. The $\mathbf{ON_{Co}}$ homopolymer will selectively segregate into cobalt-containing microdomains of BCPs and hence increasing their dimensions and at the same time will not be increasing the d-spacing.

4.4. Summary

The dipolar interactions between the cobalt nanoparticles, formed within the cylindrical domains of the BCPs, were varied by varying the composition of the metal-containing block and the overall molecular weight of the BCPs. A series of novel BCPs, in which the metal-containing block was composed of both cobalt- and ferrocene-functionalized monomers, were developed to study the effect of dilution of cobalt density within the cylindrical domains of BCPs on their magnetic properties. The cobalt density within the cylindrical domains of the BCPs was reduced by decreasing the ratio of cobalt-functionalized monomers compared to ferrocene-functionalized monomers within metal-containing blocks of BCPs. The coercivity of these BCPs reduced continuously with increased dilution of cobalt density within the cylindrical domains of BCPs and was attributed to the decrease in dipolar interactions, resulting in smaller grain or domain sizes. Temperature dependence of in-phase [χ'(T)] and out-of-phase [χ'' (T)] components of AC susceptibility measured at different frequencies for three different polymers (**C1**, **C3** and **C8**), with varying cobalt-containing monomer ratios, did not exhibit peak maxima. Hence, the determination of relaxation times (τ_0) and energy barriers (E_B) was not possible. These BCPs with multi-components are complex systems and it is non-trivial to derive any conclusive interpretations from their dynamic magnetic behavior. Additionally, a series of cobalt-containing BCPs with varying molecular weights from ~50 – 300 kDa were synthesized to investigate the effect of cylindrical domain diameter on the dipolar interactions between the cobalt particles and hence the magnetic properties of the BCPs. The diameters of the cylindrical domains were varied within the range of 16 – 25 nm. However, the values of coercivities for these BCPs were not significantly different. A wider range of diameters (5 – 50 nm) of cylindrical domains might show a significant effect of diameter on the dipolar coupling between the cobalt nanoparticles and hence on the magnetic behavior of cobalt-containing BCPs. However, BCPs with very high molecular weights (M_w) are necessary (greater than 300 kDa) in order to obtain diameter of cylindrical domains larger than 25 nm which might be a synthetic challenge.

CHAPTER 5

ZWITTERIONIC POLYMER VESICLES IN IONIC LIQUID

5.1. Introduction

Amphiphilic block copolymers (ABC) can spontaneously self-assemble into several nanostructures in solution with wide variety of morphologies such as micelles, rods and polymer vesicles (PV).[11, 158] Among them, PV have attracted considerable attention in the last decade as they hold potential for a variety of applications, including drug delivery, nanoreactors, biomineralization, imaging, biosensors, and electronics.[26, 159-162] They offer the possibility of tuning their physicochemical and biological properties simply by varying the block copolymer composition. Parameters such as relative block lengths, polydispersity, the nature and composition of solvent and the presence of additives can be varied to tune the size and morphology of PV.[163-167] Further, it is possible to functionalize them with peptide moieties and thus tune their biological properties as well.[34] Further, by suitable tailoring of polymer architecture, smart PVs responsive to external stimuli such as pH, temperature, oxidation/reduction, light etc. have also been illustrated.[5] [168] Although they have been extensively studied, and a number of different chemistries have been used to make vesicles,[169] the greatest majority of reports have hydrophilic blocks composed of nonionic poly(ethylene oxide) (PEO) or charged poly(acrylic acid), while polymers such as polystyrene (PS), poly(lactic acid), polycaprolactone, polybutadiene, and poly(propylene oxide) compose the hydrophobic block.[170-176]

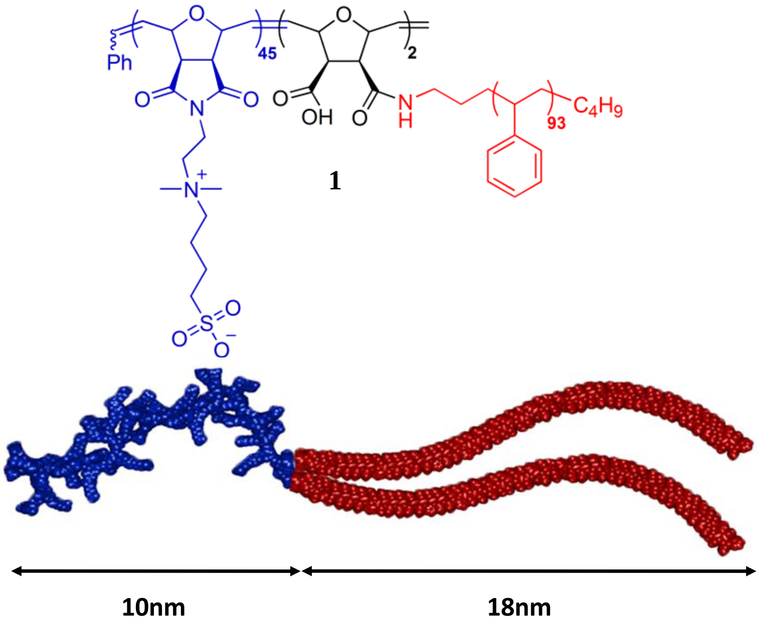

Figure 5.1 The chemical structure and molecular graphics image of the zwitterionic ABC. The dimensions of the hydrophilic zwitterionic block (blue, 10 nm) and the hydrophobic polystyrene block (red, 18 nm) were estimated from conformationally relaxed molecular graphics by Chem3D. The average degree of polymerization of each block was controlled so that the volume fraction of the hydrophilic block is in the range for vesicle formation (25-45%).[177] The M_n is 29.5 kDa. There are 45 and 93 repeat units on average for the sulfobetaine and styrene, respectively.

Recently, zwitterionic polymers also referred to as polybetaines, have gained considerable attention as a special class of ionic polymers.[178-183] They are composed of repeat units carrying both a positive and a negative charge, ensuring an overall neutral charge.[179, 183] In aqueous solution, they show “anti-polyelectrolyte effects” at high salt concentrations.[183] In addition, they resemble natural functional groups, such as phosphatidylcholines, and hence are thought to be biocompatible.[26, 160] Zwitterionic PVs are considered as analogues to mammalian cell membranes since they both present a bilayered structure and expose the unique zwitterion functional group on the surfaces of the bilayer.[184, 185] Despite their many interesting properties, there are only few reports about the self-assembly of zwitterionic BCPs forming vesicles.[186, 187] Hence, the synthesis and self-assembly of a novel zwitterionic amphiphilic block polymer into PVs is illustrated in this chapter.

The nature and composition of the solvent plays an important role in determining the size and structure of PVs.[167, 188-191] Although PV formation in aqueous media has been extensively investigated; only recently these studies have been extended to non-aqueous media such as organic solvents, super critical CO_2, and ionic liquids.[192-197, 198] Ionic liquids, or salts that are liquid at room temperature and are promising alternative solvents for environmental friendly reactions, chemical separation and storage due to their unique features such as negligible volatility, non-combustibility, electrochemical and thermal stability.[199-201] PVs in ionic liquid will give access to new applications in green chemistry such as biocatalysis, nano/micro reactors for organic and inorganic synthesis.[202-206] To date, however, the study of PVs in ionic liquids has been confined only to neutral ABCs based on PEO.[198] How does the ionic liquid will impact vesicle assembly of the ABC, which contains a charged hydrophilic block remains an open question. Ionic liquids possess at least two contrasting properties that were expected to influence PV self-assembly of **1**. While their ionic strengths have been calculated between 1-10 M, their E_TN parameters (normalized empirical parameter of solvent polarity) are more typical of polar organic solvents like DMSO. For example, quaternary ammonium sulfonates have E_TN values of 0.45-0.65 (DMSO, $E_TN = 0.44$).[199] Therefore while they are much less polar than aqueous solutions, their high ionic strength is expected to reduce PV size due to electrostatic screening.[203, 207] Even though ammonium-based ionic liquids are considered to be close ion-pairs, their ionic strength is still larger than standard PBS solutions. An effort was made to answer this question by demonstrating the self-assembly of PVs from a zwitterionic ABC, **1**, in the ionic liquid (2-hydroxyethyl) dimethyl ammonium methanesulfonate. The PVs were formed in an ionic liquid and was compared to one formed in aqueous solutions.

Previously, we reported that ring opening metathesis polymerization (ROMP) could be successfully used to synthesize well-defined, norbornene-based zwitterionic polymers.[208, 209] Here, this chemistry was extended to generate a new ABC, **1**, where the zwitterionic block was combined with a PS block. The zwitterionic block was synthesized by ROMP of a norbornene-based sulfobetaine (M_n = 16.8 kDa, PDI = 1.06), which was subsequently end-capped with maleic anhydride functionalities (M_n = 17.1 kDa, PDI = 1.06). The anhydride containing monomer was added in a stoichiometric ratio to yield, on average, two repeat units per chain end. Although other more precise methods exist to 'end-cap' polymer chains produced by ROMP, they also require more effort (reagent synthesis, post polymerization reactions, etc.).[210, 211] Finally, an amine-terminated PS chain was attached to the zwitterionic block via ring opening of the anhydrides to yield the ABC, **1** (M_n = 29.5 kDa, PDI = 1.27).[186, 212-216] The degrees of polymerization of the zwitterionic block and polystyrene blocks were 45 and 93, respectively; chosen so that the volume fraction of the hydrophilic block was around 35%, favoring vesicle formation (25-45%).[177] Detailed synthetic procedures and chemical characterization has been reported in our recent publication.[217]

5.2. Experimental

5.2.1. Vesicle Preparation

The formation of zwitterionic polymer vesicles in ionic liquid was done by using a method similar to the solvent-switch technique published in literature.[218] The zwitterionic amphiphilic block copolymer **1** was not directly soluble in ionic liquid. Hence, **1** (3 mg) was initially dissolved in a mixture of solvents, DCM (2 mL) and TFE (1 mL), to prepare a polymer solution of concentration 1 mg/mL. TFE was used as a good solvent for the hydrophilic zwitterionic block and DCM for the hydrophobic PS block. Upon complete dissolution of the block copolymer in the organic solvents, 1 mL polymer solution was mixed with 1 mL (2-hydroxyethyl) dimethyl ammonium methanesulfonate ionic liquid. After assuring a homogenous mixture, DCM and TFE were removed by applying vacuum at 80 ºC for 12 hours.

The zwitterionic polymer vesicles in 0.1 M PBS buffer (at pH = 7.4) were formed by using the film rehydration method as described by Discher *et al.*[26] **1** (3 mg) was dissolved in a mixture of DCM (2 mL) and TFE (1 mL) to prepare a polymer solution of concentration 1 mg/mL. This polymer solution was first thoroughly dried onto the wall of a 25 mL glass vial under vacuum for 4 hours in a rotary evaporator. These films were then rehydrated with 0.1 M PBS buffer (3 mL) and sonicated at 80 ºC for 10 minutes, repeating for 3 times with a gap of 5 minutes between each trial.

5.2.2. Transmission Electron Microscopy

The structure and size of zwitterionic polymer vesicles were characterized by conventional transmission electron microscopy (JEOL 100CX) operating at 100.0 kV. To observe the vesicles dispersed in the ionic liquid, a drop of the sample was placed on parafilm and then applied to the carbon-coated TEM grid by touching the drop with one face of the TEM grid. These grids were stored under vacuum overnight prior to characterization by TEM to remove any absorbed water. Lower emission current was used by using smaller spot size (spot size 3) to reduce the movement of ionic liquid due to interaction with electron beam. To observe the vesicles dispersed in 0.1 M PBS buffer, 500 μL of solution containing vesicles was spread on parafilm and mixed with 500 μL of 1 wt% sodium tungstate (maintained at pH 6.8 with 1.0 N KOH) (vesicle dispersion/sodium tungstate in 1:1 v/v ratio), a TEM negative stain. After sitting for 2 minutes, a drop of this solution was placed on a 400 mesh copper grid coated with formvar and stabilized with carbon film coating. The excess fluid was drained off with filter paper. These TEM grids were then floated on top of deionized water to remove any excess stain. The grids were then wicked and allowed to dry at room temperature and stored under vacuum.

5.2.3. Dynamic Light Scattering

To investigate the vesicle formation and the average size, dynamic light scattering (DLS) was used. Measurements were performed at room temperature using an ALV unit equipped with an ALV/SP-125 precision goniometer (ALV-LASER Vertreibsgessellchsaft m.b.h., Langen, Germany), an Innova 70 argon laser (λ = 514.5 nm; maximum power 3 W, Coherent Inc.) operated at 300 mW, and a photomultiplier detector (Thorn EMI electron tubes). Signals from the detector were processed by an ALV 5000 Multiple Tau Digital Correlator board and its associated software.

For the DLS measurements of polymer vesicles prepared in the 0.1 M PBS buffer and ionic liquid, the solutions of 1 mg/mL concentration were filtered through 0.45 μm PTFE syringe filters into a cylindrical scattering cell with an outer diameter of approximately 0.25 inch, and were sealed. Due to high viscosity of the ionic liquid, it was filtered prior to the preparation of vesicles. Since the ionic liquid is highly hygroscopic, the vesicle dispersion was heated at 80 ºC under vacuum for 8 hours to remove any absorbed water and then sealed. The scattering cell containing vesicle dispersion was then immersed in a large diameter thermostated bath at 25 ºC containing the index matching fluid, decalin. The intensity correlation functions g_2(t) were taken in 30º angular increments from 30º to 120º, for a duration of 5 minutes. From these autocorrelation functions, the diffusion coefficient D is derived and from which the hydrodynamic radius, R_h is calculated.

5.2.4. Scanning Electron Microscopy (SEM)

A drop of solution was placed on a double-sided tape on a SEM sample mount. The drop was allowed to dry at room temperature for several hours, followed by surface coating with Au (10 nm) in a gold sputter coater (Tedpella Inc.), and then characterized by a FEI Magellan 400 field emission scanning electron microscope

5.3. Characterization of Vesicles

Representative TEM images of the vesicles formed in the ionic liquid are shown in Figures 5.2a and 5.2b. The hydrophilic zwitterionic block has a preference for the ionic liquid allowing the hydrophobic polystyrene block, to form the membrane core. The dark contrast observed in the TEM micrograph is due to the PS block (see Figure 5.2a), because the outer hydrophilic block was completely dissolved in the ionic liquid and thus invisible in TEM images. The average PV diameter in the ionic liquid was determined by both TEM and dynamic light scattering (DLS). As shown in the TEM micrograph of Figure 5.2a, the average PV diameter is 120–150 nm. This was consistent with the average diameter determined by DLS shown in Figure 5.3a. The hydrodynamic radius, R_h, of 70 nm (140 nm diameter) was calculated using the slope of the plot of Γ vs. q^2 for four angles (30º, 60º, 90º, and 120º). The inset in Figure 5.3a shows the size distribution collected at 90º for PVs with an R_h of 60 nm (120 nm diameter).

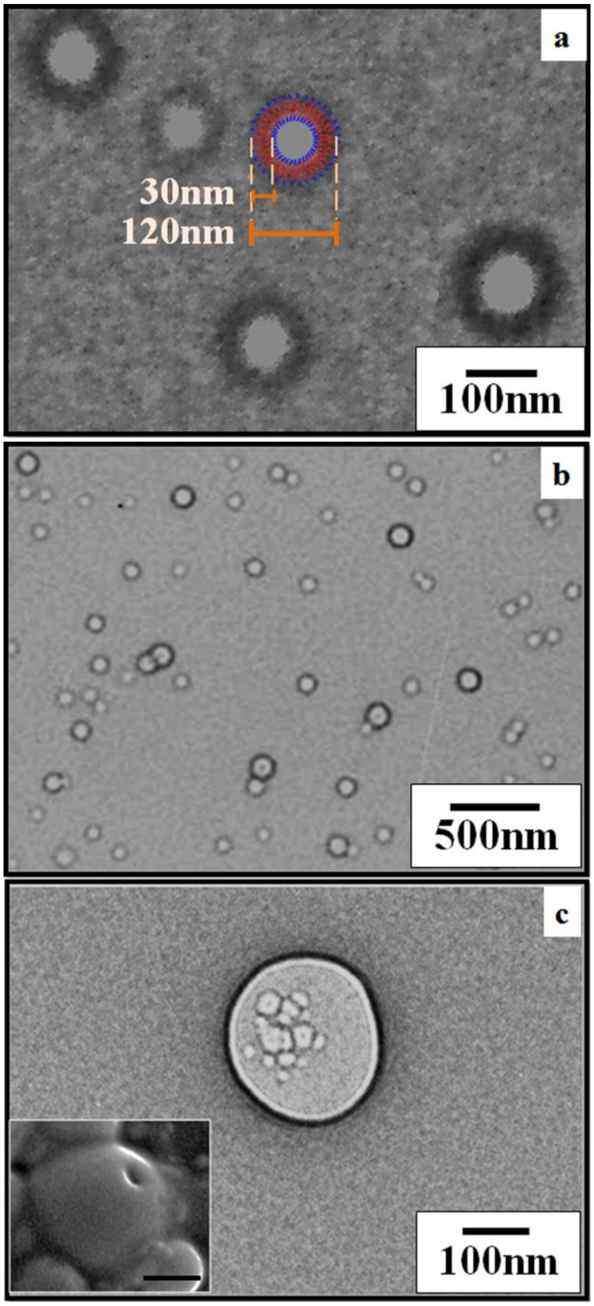

Figure 5.2 TEM images of zwitterionic PVs from **1**: a) formed in ionic liquid at higher magnification b) at lower magnification c) formed in PBS buffer. The inset in (c) shows the same vesicles imaged by SEM, where the scale bar corresponds to 100 nm.

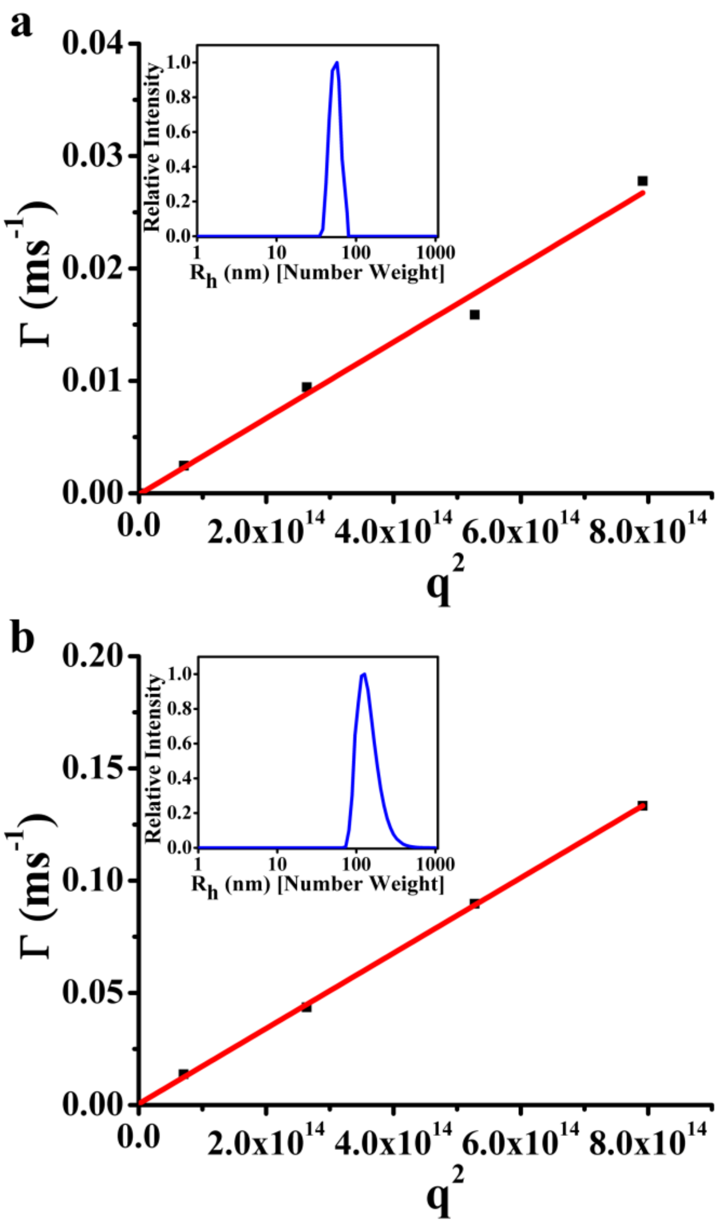

Figure 5.3 DLS data from the zwitterionic ABC, **1**, in (a) the ionic liquid and (b) PBS buffer. The plots show Γ vs. q^2 for four angles (30º, 60º, 90º, and 120º) along with the fitting line. The slope of this line was used to determine the diffusion coefficient, D, which provided the hydrodynamic radius, R_h, using the Stokes-Einstein equation. The insets in (a) and (b) show relative scattering intensity vs. R_h obtained at 90º

The hydrophobic core thickness of the PVs was estimated to be around 30 nm from TEM image analysis (Figure 5.2a) and is in the range of PV wall thicknesses generally observed.[219] This is consistent with a bilayer membrane structure based on the length of the hydrophobic PS, which was calculated to be 18 nm (see Figure 5.1) with MM2 energy minimization using Chem3D for a gaussian conformation. Based on the degree of polymerization, the dimensions of the PS block was found to be 21 nm. These dimensions show that the vesicle is composed of a double layer with limited interpenetration of the PS chains.[196] This results from a combination of factors including the volume occupied by each block of the ABC in the vesicle.

Polymer vesicles were also prepared in 0.1 M PBS buffer, which allowed a direct comparison between the two solvents (ionic strength), and also enabled us to confirm the ability of this novel ABC to form PVs under more traditional conditions. The nanostructures in PBS buffer were formed by the film rehydration method.[26] DLS indicated that the average diameter of PVs in these solutions was 250 nm as shown by the peak maximum of 125 nm in the inset of Figure 5.3b for R_h. A hydrodynamic radius of 150 nm (300 nm diameter) was determined using the plot of Γ vs. q^2 for four angles (30º, 60º, 90º, and 120º). TEM analysis upon drying and negative staining yielded PV diameters of approximately 200 nm as shown in Figure 5.2c, in agreement with DLS. In addition, PVs formed in PBS buffer were larger than those in the ionic liquid, which is consistent with the expectation that the higher ionic strength of the ionic liquid allowed more effective screening of the charges (strong dipoles) on the zwitterionic block.

The effects of drying during sample preparation are evident in the TEM micrograph of Figure 5.2c as patchy, lighter spots on the PV. These surface defects, or holes in the membrane, were further confirmed by scanning electron microscopy (SEM). The inset of Figure 5.2c shows the expected spherical morphology but with a dimple or pore. The patchy spots in TEM and the pores in SEM were seen routinely.[13] As expected, such defects were not observed in the TEM of PVs dispersed in the ionic liquid, demonstrating another benefit of using the ionic liquid for characterization of PVs. The ability to visualize these defects in the PVs prepared in PBS buffer may be related to the use of PS as the hydrophobic core, which has a high glass transition temperature (T_g). Under the high vacuum of TEM or SEM, the remaining interior buffer solution of the PVs must escape rapidly and likely leads to the observed membrane damage. However, due to the high T_g of the PS block it is unable to reorganize, thereby allowing the 'pore' to be visualized.

5.4. Summary

In summary, a novel ABC having a hydrophilic zwitterionic block and hydrophobic PS block was synthesized. The formation of zwitterionic vesicles in an ionic liquid, as well as PBS buffer, was confirmed by TEM and DLS. The ionic liquid allowed vesicle formation and simultaneously the use of conventional, room temperature TEM to visualize them. Application of this approach is easily envisaged for the characterization of other hydrophilic nanostructured assemblies such as gels and biological materials.

BIBLIOGRAPHY

1. Nalwa, H. S., *Polymeric Nanostructures and Their Applications*. American scientific: Los angeles, 2006; Vol. 1-2.

2. Martin, J. I.; Nogues, J.; Liu, K.; Vicent, J. L.; Schuller, I. K., Ordered magnetic nanostructures: fabrication and properties. *J. Mag. Mag. Mat.* **2003,** 256 (1-3), 449-501.

3. Cheng, J. Y.; Ross, C. A.; Smith, H. I.; Thomas, E. L., Templated self-assembly of block copolymers: Top-down helps bottom-up. *Adv. Mat.* **2006,** 18 (19), 2505-2521.

4. Kim, B. H.; Jeong, S. J.; Shin, D. O.; Park, S. H.; Lee, H. M.; Xia, G.; Koo, C. M.; Kim, S. O., Directed self-assembly of block copolymers combining top-down and bottom-up approaches. *Electronic Materials Letters* **2007,** 3 (3), 147-153.

5. Whitesides, G. M.; Grzybowski, B., Self-assembly at all Scales. *Science* **2002,** 295 (5564), 2418-2421.

6. Whitesides, G. M.; Mathias, J. P.; Seto, C. T., Molecular self-assembly and nanochemistry: a chemical strategy for the synthesis of nanostructures. *Science* **1991,** 254 (5036), 1312-1319.

7. Lehn, J.-M., Toward self-organization and complex matter. *Science* **2002,** 295 (5564), 2400-2403.

8. Lehn, J.-M., Toward complex matter: Supramolecular chemistry and self-organization. *PNAS* **2002,** 99 (8), 4763-4768.

9. Hamley, I. W., *Introduction to Soft Matter : Synthetic and Biological Self-assembling Materials*. John Wiley & Sons: Hoboken, NJ, 2007.

10. Klok, H.-A.; Lecommandoux, S., Supramolecular materials via block copolymer self-assembly. *Adv. Mater.* **2001,** 13 (16), 1217-1229.

11. Hamley, I. W., *The Physics of Block Copolymers*. Oxford University Press: New york, 1998.

12. Bates, F. S.; Fredrickson, G. H., Block copolymers—Designer soft materials. *Physics Today* **1999,** 52 (2), 32-38.

13. Hamley, I. W., Nanostructure fabrication using block copolymers. *Nanotechnology* **2003,** 14 (10), R39–R54.

14. Lecommandoux, S.; Borsali, R., On the physics of block copolymers. *Polymer International* **2006,** 55 (10), 1161-1168.

15. Lazzari, M.; Liu, G.; Lecommandoux, S., *Block Copolymers in Nanoscience*. Wiley-VCH: Weinheim, Germany, 2007.

16. Castelletto, V.; Hamley, I. W., Morphologies of block copolymer melts. *Current Opinion in Solid State & Materials Science* **2004,** 8 (6), 426-438.

17. Leibler, L., Theory of microphase seperation in block copolymers. *Macromolecules* **1980,** 13 (6), 1602 - 1617.

18. Matsen, M. W.; Schick, M., Self-assembly of block copolymers. *Curr. Opin. Colloid Interface Sci.* **1996** 1 (3), 329-336.

19. Bates, F. S.; Fredrickson, G. H., Block copolymer thermodynamics - theory and experiment. *Annual Review of Physical Chemistry* **1990,** 41, 525-557.

20. Matsen, M. W.; Bates, F. S., Unifying weak- and strong-segregation block copolymer theories. *Macromolecules* **1996,** 29 (4), 1091-1098.

21. Bates, F. S.; Fredrickson, G. H., Block copolymers - Designer soft materials. *Physics Today* **1999,** 52 (2), 32-38.

22. Ruzette, A. V.; Leibler, L., Block copolymers in tomorrow's plastics. *Nature Materials* **2005,** 4 (1), 19-31.

23. Blanazs, A.; Armes, S. P.; Ryan, A. J., Self-assembled block bopolymer aggregates: From micelles to vesicles and their biological applications. *Macromolecular Rapid Communications* **2009,** 30 (4-5), 267-277.

24. Smart, T.; Lomas, H.; Massignani, M.; Flores-Merino, M. V.; Perez, L. R.; Battaglia, G., Block copolymer nanostructures. *Nano Today* **2008,** 3 (3-4), 38-46.

25. Zhang, L. F.; Eisenberg, A., Multiple morphologies of crew-cut aggregates of Polysytrene-b-Poly(acrylic acid) block-copolymers. *Science* **1995,** 268, (5218), 1728-1731.

26. Discher, D. E.; Eisenberg, A., Polymer Vesicles. *Science* **2002,** 297 (5583), 967-973.

27. Shen, H. W.; Eisenberg, A., Morphological phase diagram for a ternary system of block copolymer PS310-b-PAA(52)/dioxane/H_2O. *J. Phys. Chem. B* **1999,** 103 (44), 9473-9487.

28. Zhang, L. F.; Yu, K.; Eisenberg, A., Ion-induced morphological changes in "crew-cut" aggregates of amphiphilic block copolymers. *Science* **1996,** 272 (5269), 1777-1779.

29. Zhang, L. F.; Eisenberg, A., Morphogenic effect of added Ions on crew-cut aggregates of Polystyrene-b-poly(acrylic acid) block copolymers in solutions. *Macromolecules* **1996,** 29 (27), 8805-8815.

30. Burke, S.; Shen, H. W.; Eisenberg, A., Multiple vesicular morphologies from block copolymers in solution. *Macromolecular Symposia* **2001,** 175, 273-283.

31. Terreau, O.; Luo, L. B.; Eisenberg, A., Effect of Poly(acrylic acid) block length distribution on Polystyrene-b-Poly(acrylic acid) aggregates in solution. 1. Vesicles. *Langmuir* **2003,** 19 (14), 5601-5607.

32. Luo, L. B.; Eisenberg, A., Thermodynamic stabilization mechanism of block copolymer vesicles. *J. Am. Chem. Soc.* **2001,** 123 (5), 1012-1013.

33. Desbaumes, L.; Eisenberg, A., Single-solvent preparation of crew-cut aggregates of various morphologies from an amphiphilic diblock copolymer. *Langmuir* **1999,** 15 (1), 36-38.

34. Demirgoz, D.; Pangburn, T. O.; Davis, K. P.; Lee, S.; Bates, F. S.; Kokkoli, E., PR_b-targeted delivery of tumor necrosis factor-alpha by polymersomes for the treatment of prostate cancer. *Soft Matter* **2009,** 5 (10), 2011-2019.

35. Lodge, T. P., Block Copolymers: Past Successes and Future Challenges. *Macromol. Chem. Phys.* **2003,** 204 (2), 265-273.

36. Buschow, K. H. J.; De Boer, F. R., *Physics of Magnetism and Magnetic Materials*. Kluwer Academic/Plenum Publishers: New York, 2003.

37. Davies, A. G.; Thompson, J. M. T., *Advances in Engineering : Electronics, Materials and Assembly*. Imperial College Press: London, 2007.

38. Gutfleisch, O.; Willard, M. A.; Bruck, E.; Chen, C. H.; Sankar, S. G.; Liu, J. P., Magnetic Materials and Devices for the 21st Century: Stronger, Lighter, and More Energy Efficient. *Adv. Mat.* **2011,** 23 (7), 821-842.

39. Lau, J. W.; Shaw, J. M., Magnetic nanostructures for advanced technologies: fabrication, metrology and challenges. *J. Phys. D: Appl. Phys.***2011,** 44 (30), 303001.

40. Cheng, J. Y.; Mayes, A. M.; Ross, C. A., Nanostructure engineering by templated self-assembly of block copolymers. *Nature Materials* **2004,** 3 (11), 823-828.

41. Boyen, H. G.; Kastle, G.; Zurn, K.; Herzog, T.; Weigl, F.; Ziemann, P.; Mayer, O.; Jerome, C.; Moller, M.; Spatz, J. P.; Garnier, M. G.; Oelhafen, P., A micellar route to ordered arrays of magnetic nanoparticles: From size-selected pure cobalt dots to cobalt-cobalt oxide core-shell systems. *Adv. Funct. Mater.***2003,** 13 (5), 359-364.

42. Brust, M.; Kiely, C. J., Some recent advances in nanostructure preparation from gold and silver particles: a short topical review. *Colloids and Surfaces a-Physicochemical and Engineering Aspects* **2002,** 202 (2-3), 175-186.

43. Cullity, B. D., *Introduction to Magnetic Materials*. John Wiley & Sons Inc.: 2000.

44. Bedanta, S.; Kleemann, W., Supermagnetism. *J. Phys. D: Appl. Phys.***2009,** 42 (1), 013001.

45. Jun, Y.-W.; Seo, J.-W.; Cheon, A., Nanoscaling laws of magnetic nanoparticles and their applicabilities in biomedical sciences. *Acc. Chem. Res.* **2008,** 41 (2), 179-189.

46. Hertel, R.; Kirschner, J., Magnetization reversal dynamics in nickel nanowires. *Physica B-Condensed Matter* **2004,** 343 (1-4), 206-210.

47. Fiorani, D.; Dormann, J. L.; Cherkaoui, R.; Tronc, E.; Lucari, F.; D'Orazio, F.; Spinu, L.; Nogues, M.; Garcia, A.; Testa, A. M., Collective magnetic state in nanoparticles systems. *J. Mag. Mag. Mat.* **1999,** 196, 143-147.

48. Dormann, J. L.; Bessais, L.; Fiorani, D., A Dynamic Study Of Small Interaction Particles - Superparamagnetic Model and Spin-glass Laws. *J. Phys. C. Solid St. Phys.* **1988,** 21 (10), 2015-2034.

49. Dormann, J. L.; Fiorani, D.; Tronc, E., Magnetic relaxation in fine-particle systems.Adv. Chem. Phys., **1997,** 98, 283-494.

50. Fiorani, D.; Dormann, J. L.; Lucari, F.; D'Orazio, F.; Tronc, E.; Jolivet, J. P., Dynamical magnetic behavior of interacting gamma-Fe_2O_3 particles. *Appl. Organomet. Chem.* **1998,** 12 (5), 381-386.

51. Dormann, J. L.; Cherkaoui, R.; Spinu, L.; Nogues, M.; Lucari, F.; D'Orazio, F.; Fiorani, D.; Garcia, A.; Tronc, E.; Jolivet, J. P., From pure superparamagnetic regime to glass collective state of magnetic moments in gamma-Fe_2O_3 nanoparticle assemblies. *J. Mag. Mag. Mat.* **1998,** 187 (2), L139-L144.

52. Sankar, S.; Dender, D.; Borchers, J. A. S.; Smith, D. J.; Erwin, R. W.; Kline, S. R.; Berkowitz, A. E., Magnetic correlations in non-percolated Co-SiO_2 granular films. *J. Mag. Mag. Mat.* **2000,** 221 (1-2), 1-9.

53. Petracic, O.; Chen, X.; Bedanta, S.; Kleemann, W.; Sahoo, S.; Cardoso, S.; Freitas, P. P., Collective states of interacting ferromagnetic nanoparticles. *J. Mag. Mag. Mat.* **2006,** 300 (1), 192-197.

54. Morup, S., Magnetic hyperfine splitting in Mossbauer-spectra of micro-crystals. *J. Mag. Mag. Mat.* **1983,** 37 (1), 39-50.

55. Aslibeiki, B.; Kameli, P.; Salamati, H.; Eshraghi, M.; Tahmasebi, T., Superspin glass state in $MnFe_2O_4$ nanoparticles. *J. Mag. Mag. Mat.* **2010,** 322 (19), 2929-2934.

56. Nakamae, S.; Crauste-Thibierge, C.; Komatsu, K.; L'Hote, D.; Tahri, Y.; Vincent, E.; Dubois, E.; Dupuis, V.; Perzynski, R., Superspin glass aging behavior in textured and nontextured frozen ferrofluid. *J. Appl. Phys.* **2010,** 107(9), 09E135.

57. Suzuki, M.; Fullem, S. I.; Suzuki, I. S.; Wang, L.; Zhong, C.-J., Observation of superspin-glass behavior in Fe_3O_4 nanoparticles. *Phys. Rev. B.* **2009,** 79(2), 024418.

58. Sasaki, M.; Jonsson, P. E.; Takayama, H.; Mamiya, H., Aging and memory effects in superparamagnets and superspin glasses. *Phys. Rev. B.* **2005,** 71(10), 104405.

59. Nakamae, S.; Tahri, Y.; Thibierge, C.; L'Hote, D.; Vincent, E.; Dupuis, V.; Dubois, E.; Perzynski, R., Observation of superspin glass state in magnetically textured ferrofluid gamma-Fe_2O_3. *J. Appl. Phys.* **2009,** 105(7), 07E318.

60. Bedanta, S.; Eimueller, T.; Kleemann, W.; Rhensius, J.; Stromberg, F.; Amaladass, E.; Cardoso, S.; Freitas, P. P., Overcoming the dipolar disorder in dense CoFe nanoparticle ensembles: Superferromagnetism. *Phys. Rev. Lett.* **2007,** 98 (17), 176601.

61. Bedanta, S.; Petracic, O.; Kentzinger, E.; Kleemann, W.; Rucker, U.; Paul, A.; Bruckel, T.; Cardoso, S.; Freitas, P. P., Superferromagnetic domain state of a discontinuous metal insulator multilayer. *Phys. Rev. B.* **2005,** 72 (2), 024419.

62. Bedanta, S.; Petracic, O.; Stromberg, F.; Kleemann, W.; Cardoso, S.; Freitas, P. P. In *Transition from Non-Percolated Superferromagnetism to Percolated Ferromagnetism in Granular Metal-Insulator Multilayers*, International Workshop on Mesoscopic, Nanoscopic, and Macroscopic Materials, Bhubaneswar, INDIA, Jan 02-04, 2008; Bhubaneswar, INDIA, 2008; pp 119-124.

63. Bedanta, S.; Petracic, O.; Chen, X.; Rhensius, J.; Kentzinger, E.; Ruecker, U.; Brueckel, T.; Doran, A.; Scholl, A.; Cardoso, S.; Freitas, P. P.; Kleemann, W., Single-particle blocking and collective magnetic states in discontinuous CoFe/Al_2O_3 multilayers. *J. Phys. D: Appl. Phys.***2010,** 43 (47), 474002.

64. Chen, X.; Bedanta, S.; Petracic, O.; Kleemann, W.; Sahoo, S.; Cardoso, S.; Freitas, P. P., Superparamagnetism versus superspin glass behavior in dilute magnetic nanoparticle systems. *Phys. Rev. B.* **2005,** 72 (21), 214436.

65. Hamley, I. W., Nanostructure fabrication using block copolymers *Nanotechnology* **2003,** 14 (10), R39-R54.

66. Haryono, A.; Binder, W. H., Controlled Arrangement of Nanoparticle Arrays in Block-Copolymer Domains. *Small* **2006,** 2 (5), 600-611.

67. Clendenning, S. B.; Han, S.; Coombs, N.; Paquet, C.; Rayat, M. S.; Grozea, D.; Brodersen, P. M.; Sodhi, R. N. S.; Yip, C. M.; Lu, Z. H.; Manners, I., Magnetic ceramic films from a metallopolymer resist using reactive ion etching in a secondary magnetic field. *Adv. Mat.* **2004,** 16 (4), 291-296.

68. Kulbaba, K.; Manners, I., Polyferrocenylsilanes: Metal-containing polymers for materials science, self-assembly and nanostructure applications. *Macromolecular Rapid Communications* **2001,** 22 (10), 711-724.

69. MacLachlan, M. J.; Ginzburg, M.; Coombs, N.; Coyle, T. W.; Raju, N. P.; Greedan, J. E.; Ozin, G. A.; Manners, I., Shaped ceramics with tunable magnetic properties from metal-containing polymers. *Science* **2000,** 287 (5457), 1460-1463.

70. AL-Badri, Z. M.; Maddikeri, R. R.; Zha, Y.; Thaker, H. D.; Dobriyal, P.; Shunmugam, R.; Russell, T. P.; Tew, G. N., Room temperature magnetic materials from nanostructured diblock copolymers. *Nat. Commun.* **2011,** 2, 482.

71. Lopez, W. A.; Jaeger, H. M., Hierarchical self-assembly of metal nanostructures on diblock copolymer scaffolds. *Nature* **2001,** 414 (6865), 735-738.

72. Kim, B. J.; Chiu, J. J.; Yi, G.-R.; Pine, D. J.; Kramer, E. J., Nanoparticle-Induced Phase Transitions in Diblock-Copolymer Films. *Adv. Mater.* **2005,** 17 (21), 2618-2622.

73. Chiu, J. J.; Kim, B. J.; Kramer, E. J.; Pine, D. J., Control of Nanoparticle Location in Block Copolymers. *J. Am. Chem. Soc.* **2005,** 127 (14), 5036-5037.

74. Kodama, R. H., Magnetic Nanoparticles. *J. Magn. Magn. Mat.* **1999,** 200 (1-3), 359-372.

75. Zehner, R. W.; Lopes, W. A.; Morkved, T. L.; Jaeger, H.; Sita, L. R., Selective decoration of a phase-separated diblock copolymer with thiol-passivated gold nanocrystals. *Langmuir* **1998,** 14 (2), 241-244.

76. Zehner, R. W.; Sita, L. R., Electroless deposition of nanoscale copper patterns via microphase-separated diblock copolymer templated self-assembly. *Langmuir* **1999,** 15 (19), 6139-6141.

77. Cheng, J. Y.; Zhang, F.; Chuang, V. P.; Mayes, A. M.; Ross, C. A., Self-assembled one-dimensional nanostructure arrays. *Nano Letters* **2006,** 6 (9), 2099-2103.

78. Lin, Y.; Böker, A.; He, J.; Sill, K.; Xiang, H.; Abetz, C.; Li, X.; Wang, J.; Emrick, T.; Long, S.; Wang, Q.; Balazs, A.; Russell, T. P., Self-directed self-assembly of nanoparticle/copolymer mixtures. *Nature* **2005,** 434 (7029), 55-59.

79. Yeh, S.-W.; Wei, K.-H.; Sun, Y.-S.; Jeng, U.-S.; Liang, K. S., Morphological Transformation of PS-b-PEO Diblock Copolymer by Selectively Dispersed Colloidal CdS Quantum Dots. *Macromolecules* **2003,** 36 (21), 7903-7907.

80. Li, C.-P.; Wei, K.-H.; Huang, J. Y., Enhanced Collective Electron Transport by CdSe Quantum Dots Confined in the Poly(4-vinylpyridine) Nanodomains of a Poly(styrene-b-4-vinylpyridine) Diblock Copolymer Thin Film. *Angew. Chem. Int. Ed.* **2006,** 45 (9), 1449-1453.

81. Warren, S. C.; Messina, L. C.; Slaughter, L. S.; Kamperman, M.; Zhou, Q.; Gruner, S. M.; DiSalvo, F. J.; Wiesner, U., Ordered mesoporous materials from metal nanoparticle-block copolymer self-assembly. *Science* **2008,** 320 (5884), 1748-1752.

82. Lin, Y.; Boker, A.; He, J. B.; Sill, K.; Xiang, H. Q.; Abetz, C.; Li, X. F.; Wang, J.; Emrick, T.; Long, S.; Wang, Q.; Balazs, A.; Russell, T. P., Self-directed self-assembly of nanoparticle/copolymer mixtures. *Nature* **2005,** 434 (7029), 55-59.

83. Zou, S.; Hong, R.; Emrick, T.; Walker, G. C., Ordered CdSe nanoparticles within self-assembled block copolymer domains on surfaces. *Langmuir* **2007,** 23 (4), 1612-1614.

84. Biswas, S.; D., B. K.; Das, R. K.; Ghosh, S.; Hebard, A. F., Block Copolymer-Mediated Formation of Superparamagnetic Nanocomposites. *Chem. Mater.* **2009,** 21 (23), 5644-5653.

85. Park, M. J.; Char, K.; Park, J.; Hyeon, T., Effect of the casting solvent on the morphology of poly(styrene-b-isoprene) diblock copolymer/magnetic nanoparticle mixtures. *Langmuir* **2006,** 22 (4), 1375-1378.

86. Xu, C.; Ohno, K.; Ladmiral, V.; Composto, R. J., Dispersion of polymer-grafted magnetic nanoparticles in homopolymers and block copolymers. *Polymer* **2008,** 49 (16), 3568-3577.

87. Xu, C.; Ohno, K.; Ladmiral, V.; Milkie, D. E.; Kikkawa, J. M.; Composto, R. J., Simultaneous Block Copolymer and Magnetic Nanoparticle Assembly in Nanocomposite Films. *Macromolecules* **2009,** 42 (4), 1219-1228.

88. Lo, C.-T.; Chao, C.-J., Synthesis and Characterization of Magnetic Nanoparticle/Block Copolymer Composites. *Langmuir* **2009,** 25 (22), 12865-12869.

89. Park, M. J.; Park, J.; Hyeon, T.; Char, K., Effect of interacting nanoparticles on the ordered morphology of block copolymer/nanoparticle mixtures. *J. Polym. Sci. Part B - Polym. Phys.* **2006,** 44 (24), 3571-3579.

90. Ribbe, A. E.; Okumura, A.; Matsushige, K.; Hashimoto, T., Element spectroscopic imaging of poly(2-vinylpyridine)-block-polyisoprene microdomains containing palladium nanoparticles. *Macromolecules* **2001,** 34 (23), 8239-8245.

91. Wang, Q.; Nealey, P. F.; de Pablo, J. J., Behavior of single nanoparticle/homopolymer chain in ordered structures of diblock copolymers. *J. Chem. Phys.* **2003,** 118 (24), 11278-11285.

92. Yang, T.-I.; Brown, R. N. C.; Kempel, L. C.; Kofinas, P., Magneto-dielectric properties of polymer–Fe_3O_4 nanocomposites *J. Magn. Magn. Mat.* **2008,** 320 (21), 2714-2720.

93. Ahmed, S. R.; Kofinas, P., Magnetic properties and morphology of block copolymer-cobalt oxide nanocomposites. *J. Mag. Mag. Mat.* **2005,** 288, 219-223.

94. Ahmed, S. R.; Ogale, S. B.; Kofinas, P., Magnetic properties and morphology of block copolymer templated ferrimagnetic CoFe2O4 nanoparticles. *IEEE Transactions on Magnetics* **2003,** 39 (5), 2198-2200.

95. Ahmed, S. R.; Ogale, S. B.; Papaefthymiou, G. C.; Ramesh, R.; Kofinas, P., Magnetic properties of $CoFe_2O_4$ nanoparticles synthesized through a block copolymer nanoreactor route. *Appl. Phys. Lett.* **2002,** 80 (9), 1616-1618.

96. Akcora, P.; Zhang, X.; Varughese, B.; Briber, R. M.; Kofinas, P., Structural and magnetic characterization of norbornene-deuterated norbornene dicarboxylic acid diblock copolymers doped with iron oxide nanoparticles. *Polymer* **2005,** 46 (14), 5194-5201.

97. Papaefthymiou, G. C.; Ahmed, S. R.; Kofinas, P., Magnetic and structural characterization of $CoFe_2O_4$ nanoparticles encapsulated within block copolymer films. *Rev. Adv. Mat. Sci.* **2005,** 10 (4), 306-313.

98. Yang, T. I.; Brown, R. N. C.; Ckempel, L.; Kofinas, P., Controlled synthesis of core-shell iron-silica nanoparticles and their magneto-dielectric properties in polymer composites. *Nanotechnology* **2011,** 22 (10), 105601.

99. Yang, T.-I.; Brown, R. N. C.; Kempel, L. C.; Kofinas, P., Magneto-dielectric properties of polymer-Fe3O4 nanocomposites. *J. Mag. Mag. Mat.* **2008,** 320 (21), 2714-2720.

100. Yang, T.-I.; Brown, R. N. C.; Kempel, L. C.; Kofinas, P., Surfactant-modified nickel zinc iron oxide/polymer nanocomposites for radio frequency applications. *Journal of Nanoparticle Research* **2010,** 12 (8), 2967-2978.

101. Abes, J. I.; Cohen, R. E.; Ross, C. A., Selective growth of cobalt nanoclusters in domains of block copolymer films. *Chem. Mater.* **2003,** 15 (5), 1125-1131.

102. Abes, J. I.; Cohen, R. E.; Ross, C. A., Block-copolymer-templated synthesis of iron, iron-cobalt, and cobalt-nickel alloy nanoparticles. *Materials Science & Engineering C-Biomimetic and Supramolecular Systems* **2003,** 23 (5), 641-650.

103. Rider, D. A.; Liu, K.; Eloi, J.-C.; Vanderark, L.; Yang, L.; Wang, J.-Y.; Grozea, D.; Lu, Z.-H.; Russell, T. P.; Manners, I., Nanostructured magnetic thin films from organometallic block copolymers: Pyrolysis of self-assembled polystyrene-block-poly(ferrocenylethylmethylsilane). *ACS Nano* **2008,** 2 (2), 263-270.

104. Clendenning, S. B.; Cheng, A. Y.; Manners, I., Lithographic patterning and reactive ion etching of a highly metallized polyferrocenylsilane. *Metal-Containing and Metallosupramolecular Polymers and Materials* **2006,** 928, 306-319.

105. Clendenning, S. B.; Manners, I., Lithographic patterning of a highly metallized polymer resist system and pyrolytic or plasma treatment to afford ferromagnetic ceramics. *Journal of Vacuum Science & Technology B* **2004,** 22 (6), 3493-3496.

106. Liu, K.; Clendenning, S. B.; Friebe, L.; Chan, W. Y.; Zhu, X. B.; Freeman, M. R.; Yang, G. C.; Yip, C. M.; Grozea, D.; Lu, Z. H.; Manners, I., Pyrolysis of highly metallized polymers: Ceramic thin films containing magnetic CoFe alloy nanoparticles from a polyferrocenylsilane with pendant cobalt clusters. *Chem. Mater.* **2006,** 18 (10), 2591-2601.

107. Liu, K.; Fournier-Bidoz, S.; Ozin, G. A.; Manners, I., Highly Ordered Magnetic Ceramic Nanorod Arrays from a Polyferrocenylsilane by Nanoimprint Lithography with Anodic Aluminum Oxide Templates. *Chem. Mater.* **2009,** 21 (9), 1781-1783.

108. Liu, K.; Ho, C.-L.; Aouba, S.; Zhao, Y.-Q.; Lu, Z.-H.; Petrov, S.; Coombs, N.; Dube, P.; Ruda, H. E.; Wong, W.-Y.; Manners, I., Synthesis and lithographic patterning of FePt nanoparticles using a bimetallic metallopolyyne precursor. *Angew. Chem. int. Ed.***2008,** 47 (7), 1255-1259.

109. Mîinea, L. A.; Sessions, L. B.; Ericson, K. D.; Glueck, D. S.; Grubbs, R. B., Phenylethynylstyrene−Cobalt Carbonyl Block Copolymer Composites. *Macromolecules* **2004,** 37 (24), 8967–8972.

110. Thurn-Albrecht, T.; Schotter, J.; Kästle, G. A.; Emley, N.; Shibauchi, T.; Krusin-Elbaum, L.; Guarini, K.; Black, C. T.; Tuominen, M. T.; Russell, T. P., Ultrahigh-Density Nanowire Arrays Grown in Self-Assembled Diblock Copolymer Templates. *Science* **2000,** 290 (5499), 2126-2129.

111. Lagunas, A.; Jimeno, C.; Font, D.; Sola, L.; Pericas, M. A., Mechanistic studies on the conversion of dicobalt octacarbonyl into colloidal cobalt nanoparticles. *Langmuir* **2006,** 22 (8), 3823-3829.

112. Greenfield, H.; Sternberg, H. W.; Friedel, R. A.; Wotiz, J. H.; Markby, R.; Wender, I., Acetylenic Dicobalt Hexacarbonyls – Organometallic Compounds derived from Alkynes and Dicobalt Octacarbonyl. *J. Am. Chem. Soc.* **1956,** 78 (1), 120-124.

113. Gorschinski, A.; Khelashvili, G.; Schild, D.; Habicht, W.; Brand, R.; Ghafari, M.; Bonnemann, H.; Dinjus, E.; Behrens, S., A simple aminoalkyl siloxane-mediated route to functional magnetic metal nanoparticles and magnetic nanocomposites. *J. Mater. Chem.***2009,** 19 (46), 8829-8838.

114. Kato, Y.; Sugimoto, S.; Shinohara, K.; Tezuka, N.; Kagotani, T.; Inomata, K., Magnetic properties and microwave absorption properties of polymer-protected cobalt nanoparticles. *Materials Transactions* **2002,** 43 (3), 406-409.

115. Al-Badri, Z. M.; Tew, G. N., Well-defined acetylene-functionalized oxanorbornene polymers and block copolymers. *Macromolecules* **2008,** 41 (12), 4173-4179.

116. Aamer, K. A.; De Jeu, W. H.; Tew, G. N., Diblock copolymers containing metal complexes in the side chain of one block. *Macromolecules* **2008,** 41 (6), 2022-2029.

117. Aamer, K. A.; Tew, G. N., Supramolecular polymers containing terpyridine-metal complexes in the side chain. *Macromolecules* **2007,** 40 (8), 2737-2744.

118. Calzia, K. J.; Tew, G. N., Methacrylate polymers containing metal binding ligands for use in supramolecular materials: Random copolymers containing terpyridines. *Macromolecules* **2002,** 35 (16), 6090-6093.

119. Baranauskas, V. V.; Zalich, M. A.; Saunders, M.; St Pierre, T. G.; Riffle, J. S., Poly(styrene-b-4-vinylphenoxyphthalonitrile) - Cobalt complexes and their conversion to oxidatively stable cobalt nanoparticles. *Chem. Mater.* **2005,** 17 (21), 5246-5254.

120. Vadala, M. L.; Rutnakornpituk, M.; Zalich, M. A.; St Pierre, T. G.; Riffle, J. S., Block copolysiloxanes and their complexation with cobalt nanoparticles. *Polymer* **2004,** 45 (22), 7449-7461.

121. Zalich, M. A.; Baranauskas, V. V.; Riffle, J. S.; Saunders, M.; St Pierre, T. G., Structural and magnetic properties of oxidatively stable cobalt nanoparticles encapsulated in graphite shells. *Chem. Mater.* **2006,** 18 (11), 2648-2655.

122. Connolly, J.; St Pierre, T. G.; Rutnakornpituk, M.; Riffle, J. S., Cobalt nanoparticles formed in polysiloxane copolymer micelles: effect of production methods on magnetic properties. *J. Phys. D: Appl. Phys.***2004,** 37 (18), 2475-2482.

123. Papaefthimiou, V.; Dintzer, T.; Dupuis, V.; Tamion, A.; Tournus, F.; Hillion, A.; Teschner, D.; Haevecker, M.; Knop-Gericke, A.; Schloegl, R.; Zafeiratos, S., Nontrivial Redox Behavior of Nanosized Cobalt: New Insights from Ambient Pressure X-ray Photoelectron and Absorption Spectroscopies. *ACS Nano* **2011,** 5 (3), 2182-2190.

124. Skumryev, V.; Stoyanov, S.; Zhang, Y.; Hadjipanayis, G.; Givord, D.; Nogues, J., Beating the superparamagnetic limit with exchange bias. *Nature* **2003,** 423 (6942), 850-853.

125. Held, G. A.; Grinstein, G.; Doyle, H.; Sun, S. H.; Murray, C. B., Competing interactions in dispersions of superparamagnetic nanoparticles. *Phys. Rev. B.* **2001,** 64 (1), 012408.

126. Klabunde, K. J., *Nanoscale materials in chemistry*. Wiley-Interscience: New York, 2001.

127. Morrish, A. H.; IEEE Magnetics Society., *The physical principles of magnetism*. IEEE Press: New York, 2001.

128. Cannas, C.; Concas, G.; Gatteschi, D.; Musinu, A.; Piccaluga, G.; Sangregorio, C., How to tailor maghemite particle size in gamma-Fe_2O_3-SiO_2 nanocomposites. *J. Mater. Chem.***2002,** 12, (10), 3141-3146.

129. Gross, A. F.; Diehl, M. R.; Beverly, K. C.; Richman, E. K.; Tolbert, S. H., Controlling magnetic coupling between cobalt nanoparticles through nanoscale confinement in hexagonal mesoporous silica. *J. Phys. Chem. B* **2003,** 107 (23), 5475-5482.

130. Sun, S. H.; Murray, C. B., Synthesis of monodisperse cobalt nanocrystals and their assembly into magnetic superlattices (invited). *J. Appl. Phys.* **1999,** 85 (8), 4325-4330.

131. Nadeem, K.; Krenn, H.; Traussnig, T.; Wuerschum, R.; Szabo, D. V.; Letofsky-Papst, I., Effect of dipolar and exchange interactions on magnetic blocking of maghemite nanoparticles. *J. Mag. Mag. Mat.* **2011,** 323 (15), 1998-2004.

132. Nunes, W. C.; Cebollada, F.; Knobel, M.; Zanchet, D., Effects of dipolar interactions on the magnetic properties of gamma-Fe2O3 nanoparticles in the blocked state. *J. Appl. Phys.* **2006,** 99 (8), 08N705.

133. Vargas, J. M.; Nunes, W. C.; Socolovsky, L. M.; Knobel, M.; Zanchet, D., Effect of dipolar interaction observed in iron-based nanoparticles. *Phys. Rev. B.* **2005,** 72 (18), 184428.

134. Dormann, J. L.; Fiorani, D.; Tronc, E., On the models for interparticle interactions in nanoparticle assemblies: comparison with experimental results. *J. Mag. Mag. Mat.* **1999,** 202 (1), 251-267.

135. Dormann, J. L.; Ezzir, A.; Cherkakoui, R.; Nogues, M.; Lucari, F.; dOrazio, F.; Godinho, M.; Tronc, E.; Jolivet, J. P.; Fiorani, D., Static and dynamical properties of gamma-Fe_2O_3 nanoparticles. *Journal De Physique IV* **1997,** 7 (C1), 509-512.

136. Dormann, J. L.; Fiorani, D.; Cherkaoui, R.; Spinu, L.; Lucari, F.; D'Orazio, F.; Nogues, M.; Tronc, E.; Jolivet, J. P.; Garcia, A., Collective glass state in a magnetic nanoparticle system. *Nanostructured Materials* **1999,** 12, (5-8), 757-762.

137. Fiorani, D.; Dormann, J. L.; Lucari, F.; Dorazio, F.; Tronc, E.; Prene, P.; Jolivet, J. P.; Testa, A. M., Dynamic properties of interacting gamma-Fe_2O_3 particles. *Philosophical Magazine B-Physics of Condensed Matter Statistical Mechanics Electronic Optical and Magnetic Properties* **1997,** 76 (4), 457-462.

138. Novak, M. A.; Folly, W. S. D.; Sinnecker, J. P.; Soriano, S., Relaxation in magnetic nanostructures. *J. Mag. Mag. Mat.* **2005,** 294 (2), 133-140.

139. Kim, D. K.; Zhang, Y.; Voit, W.; Rao, K. V.; Muhammed, M., Synthesis and characterization of surfactant-coated superparamagnetic monodispersed iron oxide nanoparticles. *J. Mag. Mag. Mat.* **2001,** 225 (1-2), 30-36.

140. Sahoo, S.; Petracic, O.; Kleemann, W.; Stappert, S.; Dumpich, G.; Nordblad, P.; Cardoso, S.; Freitas, P. P., Cooperative versus superparamagnetic behavior of dense magnetic nanoparticles in $Co_{80}Fe_{20}/Al_2O_3$ multilayers. *Appl. Phys. Lett.* **2003,** 82 (23), 4116-4118.

141. Mira, J.; LopezPerez, J. A.; Rivas, J.; LopezQuintela, M. A.; Caciuffo, R.; Rinaldi, D.; Fiorani, D., Dynamic magnetic behaviour of interacting gamma-Fe_2O_3 nanoparticles dispersed in epoxy resin. *IEEE Transactions on Magnetics* **1997,** 33, (5), 3724-3726.

142. Zha, Y. P.; Thaker, H. D.; Maddikeri, R. R.; Gido, S. P.; Tuominen, M. T.; Tew, G. N., Nanostructured Block-Random Copolymers with Tunable Magnetic Properties. *J. Am. Chem. Soc.* **2012,** 134 (35), 14534-14541.

143. Vyacheslavov, A. S.; Eliseev, A. A.; Lukashin, A. V.; Tretyakov, Y. D.; Grigorieva, N. A.; Grigoriev, S. V.; Eckerlebe, H., Ordered cobalt nanowires in mesoporous aluminosilicate. *Materials Science & Engineering C-Biomimetic and Supramolecular Systems* **2007,** 27 (5-8), 1411-1414.

144. Forster, H.; Schrefl, T.; Scholz, W.; Suess, D.; Tsiantos, V.; Fidler, J., Micromagnetic simulation of domain wall motion in magnetic nano-wires. *J. Mag. Mag. Mat.* **2002,** 249 (1-2), 181-186.

145. Hertel, R., Computational micromagnetism of magnetization processes in nickel nanowires. *J. Mag. Mag. Mat.* **2002,** 249 (1-2), 251-256.

146. Zeng, H.; Zheng, M.; Skomski, R.; Sellmyer, D. J.; Liu, Y.; Menon, L.; Bandyopadhyay, S., Magnetic properties of self-assembled Co nanowires of varying length and diameter. *J. Appl. Phys.* **2000,** 87 (9), 4718-4720.

147. Zeng, H.; Skomski, R.; Menon, L.; Liu, Y.; Bandyopadhyay, S.; Sellmyer, D. J., Structure and magnetic properties of ferromagnetic nanowires in self-assembled arrays. *Phys. Rev. B.* **2002,** 65 (13), 134426.

148. Sellmeyer, D.; Skomski, R., *Advanced Magnetic Nanostructures*. Linconln, Nebraska, 2005.

149. Weller, D.; Moser, A., Thermal effect limits in ultrahigh-density magnetic recording. *IEEE Transactions on Magnetics* **1999,** 35 (6), 4423-4439.

150. Cowburn, R. P.; Adeyeye, A. O.; Bland, J. A. C., Magnetic switching and uniaxial anisotropy in lithographically defined anti-dot Permalloy arrays. *J. Mag. Mag. Mat.* **1997** 173 (1-2), 193-201.

151. Adeyeye, A. O.; Singh, N., Large area patterned magnetic nanostructures. *J. Phys. D: Appl. Phys.***2008,** 41 (15), 153001.

152. Heyderman, L. J.; Nolting, F.; Backes, D.; Czekaj, S.; Lopez-Diaz, L.; Klaui, M.; Rudiger, U.; Vaz, C. A. F.; Bland, J. A. C.; Matelon, R. J.; Volkmann, U. G.; Fischer, P., Magnetization reversal in cobalt antidot arrays. *Phys. Rev. B.* **2006,** 73 (21), 214429.

153. Luo, W. L.; Nagel, S. R.; Rosenbaum, T. F.; Rosensweig, R. E., Dipole interactions with random anisotropy in a frozen ferrofluid. *Phys. Rev. Lett.* **1991,** 67 (19), 2721-2724.

154. Jonsson, T.; Mattsson, J.; Djurberg, C.; Khan, F. A.; Nordblad, P.; Svedlindh, P., Aging in a magnetic particle system. *Phys. Rev. Lett.* **1995,** 75 (22), 4138-4141.

155. Zha, Y.; Maddikeri, R.; Gido, S.; Tew, G., Magnetic Properties of Cobalt-Containing Diblock Copolymers with Cylindrical Morphology of Different Domain Sizes. *J.Inorg. Organomet. Polym. Mater* **2012**, 1-6.

156. Zha, Y. P.; Thaker, H. D.; Maddikeri, R. R.; Gido, S. P.; Tuominen, M. T.; Tew, G. N., Nanostructured Block-Random Copolymers with Tunable Magnetic Properties. *J. Am. Chem. Soc.* **2012,** 134, (35), 14534-14541.

157. Carignan, L.-P.; Massicotte, M.; Caloz, C.; Yelon, A.; Menard, D., Magnetization Reversal in Arrays of Ni Nanowires With Different Diameters. *IEEE Transactions on Magnetics* **2009,** 45, (10), 4070-4073.

158. Hadjichristidis, N.; Pispas, S.; Floudas, G., *Block Copolymers: Synthetic Strategies, Physical Properties, and Applications.* Wiley, New York: 2003.

159. Sauer, M.; Haefele, T.; Graff, A.; Nardin, C.; Meier, W., *Chem. Commun.* **2001,** 23, 2452-2453.

160. Ahmed, F.; Discher, D. E., *J. Controlled Release* **2004,** 96, 37-53.

161. Ghoroghchian, P. P.; Frail, P. R.; Susumu, K.; Blessington, D.; Brannan, A. K.; Bates, F. S.; Chance, B.; Hammer, D. A.; Therien, M. J., *PNAS* **2005,** 102, 2922-2927.

162. Discher, B. M.; Won, Y.-Y.; Ege, D. S.; Lee, J. C.-M.; Bates, F. S.; Discher, D. E.; Hammer, D. A., *Science* **1999,** 284, 1143-1146.

163. Antonietti, M.; Forster, S., Vesicles and liposomes: A self-assembly principle beyond lipids. *Adv. Mat.* **2003,** 15, (16), 1323-1333.

164. Discher, B. M.; Hammer, D. A.; Bates, F. S.; Discher, D. E., Polymer vesicles in various media. *Curr. Opin. Colloid Interface Sci.* **2000,** 5, (1-2), 125-131.

165. Liu, F. T.; Eisenberg, A., Preparation and pH triggered inversion of vesicles from poly(acrylic acid)-block-polystyrene-block-poly(4-vinyl pyridine). *J. Am. Chem. Soc.* **2003,** 125, (49), 15059-15064.

166. Luo, L. B.; Eisenberg, A., Thermodynamic size control of block copolymer vesicles in solution. *Langmuir* **2001,** 17, (22), 6804-6811.

167. Soo, P. L.; Eisenberg, A., Preparation of block copolymer vesicles in solution *J. Polym. Sci.: Part B: Polym. Phys.,* **2004,** 42 (6), 923-938.

168. Li, M.-H.; Keller, P., Stimuli-responsive polymer vesicles. *Soft Matter* **2009,** 5 (5), 927-937.

169. LoPresti, C.; Lomas, H.; Massignani, M.; Smart, T.; Battaglia, G., Polymersomes: Nature inspired nanometer sized compartments *J. Mater. Chem.* **2009,** 19 (22), 3576-3590.

170. Ghoroghchian, P. P.; Li, G.; Levine, D. H.; Davis, K. P.; Bates, F. S.; Hammer, D. A.; Therien, M. J., Bioresorbable Vesicles Formed through Spontaneous Self-Assembly of Amphiphilic Poly(ethylene oxide)-*block*-polycaprolactone *Macromolecules* **2006,** 39 (5), 1673-1675.

171. Schillén, K.; Bryskhe, K.; Mel'nikova, Y. S., Vesicles Formed from a Poly(ethylene oxide)-Poly(propylene oxide)-Poly(ethylene oxide) Triblock Copolymer in Dilute Aqueous Solution *Macromolecules* **1999,** 32 (20), 6885-6888.

172. Yu, K.; Eisenberg, A., Bilayer morphologies of self-assembled crew-cut aggregates of amphiphilic PS-*b*-PEO diblock copolymers in solution *Macromolecules* **1998,** 31 (11), 3509-3518.

173. Zhang, L.; Eisenberg, A., Multiple morphologies of crew-cut aggregates of Polystyrene-b-Poly(acrylic acid) *Science* **1995,** 268 (5218), 1728-1731.

174. Kabanov, A. V.; Bronich, T. K.; Kabanov, V. A.; Yu, K.; Eisenberg, A., Spontaneous formation of vesicles from complexes of block ionomers and surfactants. *J. Am.Chem. Soc.* **1998,** 120 (38), 9941-9942.

175. Shen, H.; Eisenberg, A., Control of architecture in block-copolymer vesicles. *Angew. Chem. Int. Ed* **2000,** 39 (18), 3310-3312.

176. Love, J. A.; Morgan, J. P.; Trnka, T. M.; Grubbs, R. H., A practical and highly reactive Ruthenium-based catalyst that effects the cross-metathesis of acrylonitrile. *Angew. Chem. Int. Ed* **2002,** 41 (21), 4035-4037.

177. Discher, D. E.; Ahmed, F., Polymersomes. *Annu. Rev. Biomed. Eng.* **2006,** 8, 323-341.

178. Kumar, R.; Fredrickson, G. H., Theory of polyzwitterion confirmations. *J.Chem. Phys.* **2009,** 131, 104901.

179. Kudaibergenov, S.; Jaeger, W.; Laschewsky, A., Polymeric betaines: synthesis, characterization and application. *Adv. Polym. Sci* **2006,** 201, 157-224.

180. Mary, P.; Bendejacq, D. D.; Labeau, M. P.; Dupuis, P., Reconciling low- and high-salt solution behavior of sulfobetaine polyzwitterions. *J. Phys. Chem. B* **2007,** 111 (27), 7767-7777.

181. Salamone, J. C.; Volksen, W.; Olson, A. P.; Israel, S. C., Aqueous solution properties of a poly(vinyl imidazolium sulphobetaine). *Polymer* **1978,** 19 (10), 1157-1162.

182. Schulz, D. N.; Peiffer, D. G.; Agarwal, P. K.; Larabee, J.; Kaladas, J. J.; Soni, L.; Handwerker, B.; Garner, R. T., Phase behavior and solution properites of sulphobetaine polymers *Polymer* **1986,** 27, 1734-1742.

183. Lowe, A. B.; McCormick, C. L., Synthesis and solution properties of Zwitterionic polymers. *Chem. Rev.* **2002,** 102 (11), 4177-4189.

184. Chapman, D., Biomembranes and new hemocompatible materials. *Langmuir* **1993,** 9 (1), 39-45.

185. Liu, G. Y.; Lv, L. P.; Chen, C. J.; Hu, X. F.; Ji, J., Biocompatible Poly(D,L-lactide)-*block*-Poly(2-methacryloyloxyethylphosphorylcholine) micelles for drug delivery. *Macromol. Chem. Phys.* **2011,** 212 (6), 643-651.

186. Du, J. Z.; Tang, Y.; Lewis, A. L.; Armes, S. P., pH-sensitive vesicles based on a biocompatible zwitterionic diblock copolymer *J. Am. Chem. Soc.* **2005,** 127 (51), 17982-17983.

187. Shen, L.; Du, J. Z.; Armes, S. P.; Liu, S., Kinetics of pH-induced formation and dissociation of polymeric vesicles assembled from a water-soluble zwitterionic diblock copolymer. *Langmuir* **2008,** 24 (18), 10019-10025.

188. Antonietti, M.; Förster, S., Vesicles and Liposomes: A self-assembly principle beyond lipids *Adv. Mater.* **2003,** 15, 1323-1333.

189. Discher, B. M.; Hammer, D. A.; Bates, F. S.; Discher, D. E., Polymer vesicles in various media *Curr. Opin. Colloid Interface Sci.* **2000,** 5 (1), 125-131.

190. Liu, F.; Eisenberg, A., Preparation and pH triggered inversion of vesicles from Poly(acrylicacid)-*block*-Polystyrene-*block*-Poly(4-vinylPyridine) *J.Am.Chem.Soc.* **2003,** 125 (49), 15059-15064.

191. Luo, L.; Eisenberg, A., Thermodynamic size control of block copolymer vesicles in solution. *Langmuir* **2001,** 17 (22), 6804-6811.

192. Bai, Z.; Lodge, T. P., Polymersomes with ionic liquid interiors dispersed in water *J. Am. Chem. Soc.* **2010,** 132 (45), 16265-16270.

193. Bang, J.; Jain, S.; Li, Z.; Lodge, T. P.; Pedersen, J. S.; Kesselman, E.; Talmon, Y., Sphere, cylinder, and vesicle nanoaggregates in Poly(styrene-*b*-isoprene) diblock copolymer solutions *Macromolecules* **2006,** 39 (3), 1199–1208.

194. Di Cola, E.; Lefebvre, C.; Deffieux, A.; Narayanan, T.; Borsali, R., Micellar transformations of Poly(styrene-***b***-isoprene) block copolymers in selective solvents *Soft Matter* **2009,** 5 (5), 1081-1090.

195. Edmonds, W. F.; Hillmyer, M. A.; Lodge, T. P., Block copolymer vesicles in liquid CO_2 *Macromolecules* **2007,** 40 (14), 4917–4923.

196. He, Y.; Li, Z.; Simone, P.; Lodge, T. P., Self-assembly of block copolymer micelles in an ionic liquid *J. Am.Chem.Soc.* **2006,** 128 (8), 2745-2750.

197. Njikang, G., Han, D., Wang, J., and Liu, G., ABC Triblock Copolymer Micelle-Like Aggregates in Selective Solvents for A and C *Macromolecules* **2008,** 41 (24), 9727-9735.

198. Simone, P. M.; Lodge, T. P., Lyotropic phase behavior of Polybutadiene−Poly(ethylene oxide) diblock copolymers in ionic liquids *Macromolecules* **2008,** 41 (5), 1753-1759.

199. Welton, T., Room-temperature Ionic liquids. Solvents for synthesis and catalysis. *Chem. Rev.* **1999,** 99, 2071-2083.

200. Hoffmann, M. M.; Heitz, M. P.; Carr, J. B.; Tubbs, J. D., Surfactants in green solvent systems-current and future research directions *J. Dispersion Sci. Technol.* **2003,** 24 (2), 155-171.

201. Huddleston, J. G.; Visser, A. E.; Reichert, W. M.; Willauer, H. D.; Broker, G. A.; Rogers, R. D., Characterization and comparison of hydrophilic and hydrophobic room temperature ionic liquids incorporating the imidazolium cation. *Green Chem.* **2001,** 3 (4), 156-164.

202. Hao, J.; Zemb, T., Self-assembled structures and chemical reactions in room-temperature ionic liquids. *Curr. Opin. Colloid Interface Sci.* **2007,** 12 (3), 129-137.

203. Greaves, T. L.; Drummond, C. J., Ionic liquids as amphiphile self-assembly media. *Chem. Soc. Rev.* **2008,** 37 (8), 1709-1726.

204. Yuan, J.; Bai, X.; Zhao, M.; Zheng, L., C_{12}mimBr ionic liquid/SDS vesicle formation and use as template for the synthesis of hollow silica spheres *Langmuir* **2010,** 26 (14), 11726-11731.

205. Hao, J.; Song, A.; Wang, J.; Chen, X.; Zhuang, W.; Shi, F.; Zhou, F.; Liu, W., Self-assembled structure in room-temperature ionic liquids. *Chem. Eur. J.* **2005,** 11 (13), 3936-3940.

206. Nakashima, T.; Kimizuka, N., Vesicle in salt: formation of bilayer membranes from dialkyldimethylammonium bromides in ether-containing ionic liquids. *Chem. Lett.* **2002,** 31 (10), 1018–1019.

207. Evans, D. F.; Yamauchl, A.; Wel, G. J.; Bloomfield, V. A., Micelle size in ethylammonium nitrate as determined by classical and quasi-elastic light scattering. *J. Phys. Chem.* **1983,** 87 (18), 3537-3541.

208. Colak, S.; Tew, G. N., Synthesis and solution properties of norbornene based Polybetaines. *Macromolecules* **2008,** 41 (22), 8436-8440.

209. Colak, S.; Nelson, C. F.; Nüsslein, K.; Tew, G. N., Hydrophilic modifications of an amphiphilic Polynorbornene and the effects on its hemolytic and antibacterial activity. *Biomacromolecules* **2009,** 10 (2), 353-359.

210. Hilf, S.; Kilbinger, A. F. M., Functional end groups for polymers prepared using ring-opening metathesis polymerization *Nature Chemistry* **2009,** 1, 537-546.

211. Madkour, A. E.; Koch, A. H. R.; Lienkamp, K.; Tew, G. N., End-Functionalized ROMP polymers for Biomedical Applications *Macromolecules* **2010,** 43 (10), 4557-4561.

212. Terreau, O.; Luo, L.; Eisenberg, A., Effect of Poly(acrylic acid) Block Length Distribution on Polystyrene-*b*-Poly(acrylic acid) Aggregates in Solution. 1. Vesicles *Langmuir* **2003,** 19 (14), 5601-5607.

213. Kickelbick, G.; Bauer, J.; Hüsing, N.; Andersson, M.; Palmqvist, A., Spontaneous vesicle formation of short-chain amphiphilic Polysiloxane-*b*-Poly(ethylene oxide) block copolymers *Langmuir* **2003,** 19 (8), 3198-3201.

214. Gaitzsch, J.; Appelhans, D.; Gräfe, D.; Schwille, P.; Voit, B., Photo-crosslinked and pH sensitive polymersomes for triggering the loading and release of cargo *Chem. Comm.* **2011,** 47 (12), 3466-3468.

215. Du, J. Z.; Chen, Y. M., Preparation of Organic/Inorganic Hybrid Hollow Particles Based on Gelation of Polymer Vesicles *Macromolecules* **2004,** 37 (15), 5710-5716.

216. Power-Billard, K. N.; Spontak, R. J.; Manners, I., Redox-active organometallic vesicles: Aqueous self-assembly of a diblock copolymer with a hydrophilic polyferrocenylsilane polyelectrolyte block. *Angew. Chem. Int.* **2004,** 43 (10), 1260-1264.

217. Maddikeri, R.; Colak, S.; Gido, S.; Tew, G., Zwitterionic Polymersomes in an Ionic Liquid: Room Temperature TEM Characterization. *Biomacromolecules* **2011,** 12, (10), 3412-3417.

218. Du, J. Z.; Armes, S. P., Preparation of Biocompatible Zwitterionic Block Copolymer Vesicles by Direct Dissolution in Water and Subsequent Silicification within Their Membranes *Langmuir* 2009, 25 (16), 9564-9570.

219. Du, J. Z.; O’Reilly, R. K., Advances and challenges in smart and functional polymer vesicles *Soft Matter* **2009,** 5 (19), 3544-3561.